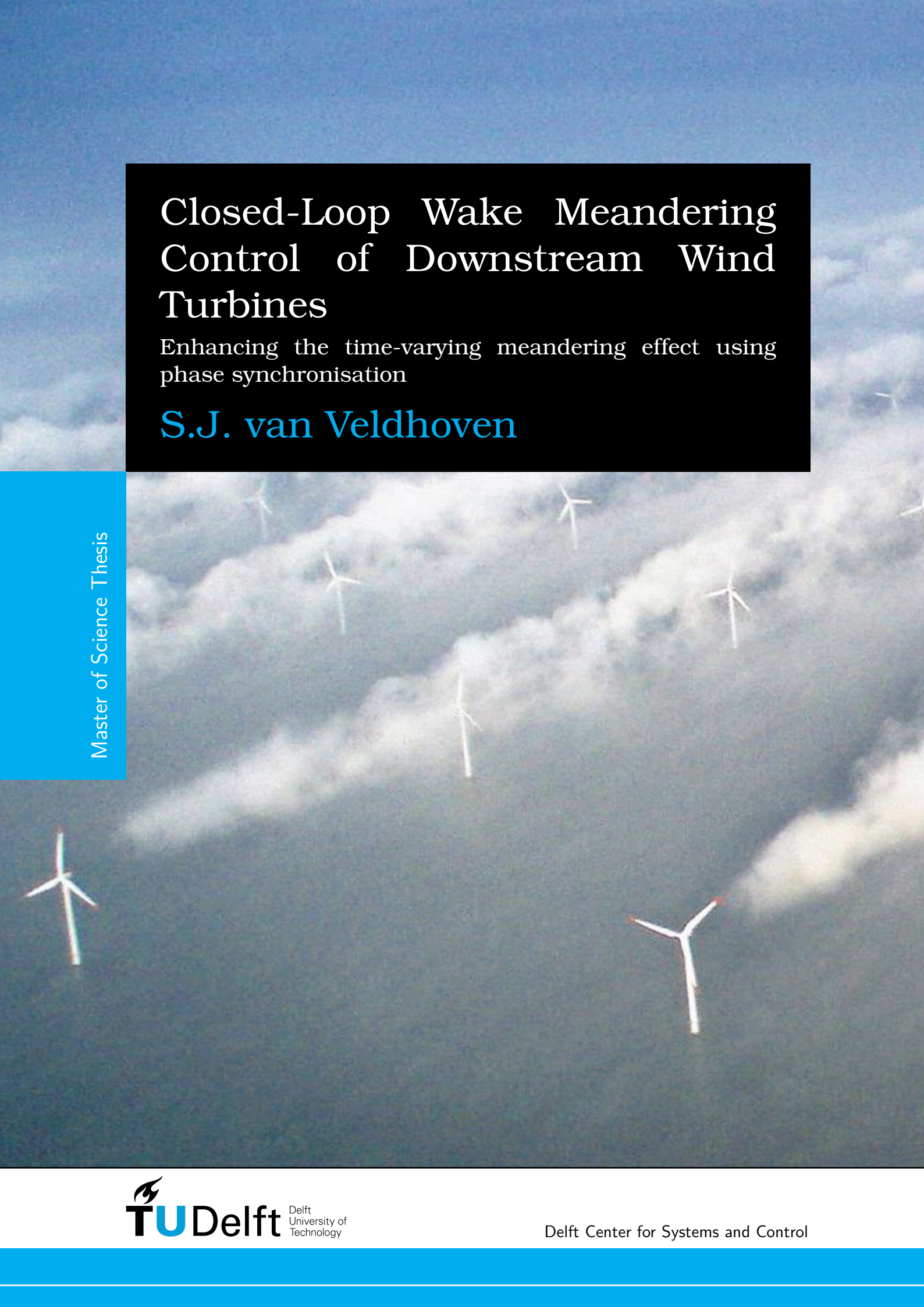

# Closed-Loop Wake Meandering Control of Downstream Wind Turbines

Enhancing the time-varying meandering effect using phase synchronisation

S.J. van Veldhoven

Master of Science Thesis

TU Delft Delft University of Technology

Delft Center for Systems and Control

# Closed-Loop Wake Meandering Control of Downstream Wind Turbines

## Enhancing the time-varying meandering effect using phase synchronisation

Master of Science Thesis

For the degree of Master of Science in Systems and Control at Delft University of Technology

S.J. van Veldhoven

April 15, 2024

Faculty of Mechanical Engineering (ME) · Delft University of Technology


Delft University of Technology
Department of
Delft Center for Systems and Control (dcsc)

The undersigned hereby certify that they have read and recommend to the Faculty of Mechanical Engineering (ME) for acceptance a thesis entitled

Closed-Loop Wake Meandering Control of Downstream Wind Turbines

by

S.J. van Veldhoven

in partial fulfillment of the requirements for the degree of

Master of Science Systems and Control

Dated: April 15, 2024

Supervisor(s):

prof.dr.ir. J.W. van Wingerden

ir. A.A.W. van Vondelen

Reader(s):

dr.ir. S.P. Mulders

dr. M. Coquelet

# Abstract

The offshore wind energy sector has experienced remarkable growth in recent years, driven by increasing demand for renewable energy sources and technological advancements. As wind farms expand and turbine sizes increase, challenges associated with wake effects and turbine interactions become more pronounced. Therefore, wind farm control strategies have been developed to mitigate the negative effects of wakes, consequently enhancing overall power production or reducing fatigue loads. The helix approach has emerged as a promising method for controlling wake dynamics, shaping the wake into a helical pattern to increase wake mixing further downstream. In this context, phase synchronisation has emerged as an extension of the helix approach, simultaneously applying the helix on up- and downstream turbines. By leveraging the existing helical periodic components induced by the upstream turbine, phase synchronisation can initiate the helix at the downstream turbine with less pitch action. However, power is still compromised at the upstream turbine due to the execution of the helix. Consequently, the potential for improvement arises with the integration of phase synchronisation onto the meandering effect—a phenomenon often already present at the downstream turbine. This effect yields benefits similar to those of the helical wake concerning wake recovery, offering the potential to improve overall power performance without power loss at the upstream turbine. This thesis has developed a phase synchronisation method to track the time-varying excitation frequency inherent to the meandering effect. Enhancements were made to a Second-Order Generalized Integrator Phase-Locked Loop (SOGI-PLL), enabling the extraction of phase, amplitude, and bias from periodic loads, which forms the basis of our closed-loop control strategy for the downstream wind turbine. The improvements led to the development of the ESOGI- and MSTOGI-HTan-QT2PLL methodologies, which address internal disturbances caused by offsets and enhance system stability, while accurately tracking of the phase during phase jumps and frequency steps and ramps. The methodologies were tested at different levels of fidelity. First, a low-order study validated the effectiveness of the proposed method during uncertain conditions, which showed better performance of the MSTOGI-HTan-QT2PLL methodology. Then, the results of the higher-fidelity experiments demonstrated that our method could successfully amplify the meandering effect without loss in power, while attenuation led to reduced fatigue loads with minimal power loss. These results show the potential of integrating phase synchronisation on the meandering effect.

# Table of Contents

# List of Figures

# List of Tables

# Acknowledgements

I want to thank my supervisors prof.dr.ir. J.W. van Wingerden and ir. A.A.W. van Vondelen for their invaluable support and guidance throughout this thesis. Their expertise, feedback, and willingness to address all my questions have been incredibly helpful in shaping this work. Special thanks to ir. A.A.W. van Vondelen for our weekly meetings and continuous assistance, and prof.dr.ir. J.W. van Wingerden for facilitating a supportive working environment that encouraged open communication and collaboration within the department.

Additionally, I would like to thank my thesis committee, consisting of prof.dr.ir. J.W. van Wingerden, ir. A.A.W. van Vondelen, dr.ir. S.P. Mulders and dr. M. Coquelet, for their thoughtful questions and feedback during the discussion and defence of this thesis.

Delft, University of Technology
April 15, 2024

S.J. van Veldhoven

# Chapter 1

# Introduction

In December 2015, the Paris Agreement was established, aiming to limit global warming to well below 2°C above pre-industrial levels, with a further target of 1.5°C to reduce climate change risks [1]. With global energy demand rising by approximately 2% annually, renewable energy is increasingly vital for meeting this demand sustainably and mitigating environmental impacts [2]. In response, many governments are setting ambitious targets for low-emission renewable energies, including onshore and offshore wind power. Offshore wind energy has seen significant global advancement, driven by two key economic factors: abundant wind resources at sea and economies of scale. The relatively smooth surface of the sea facilitates stronger and more consistent wind speeds compared to onshore sites. Additionally, the larger available space in the sea allows for the installation of more turbines within a single wind farm, thereby increasing overall power production capacity. This scalability reduces the deployment costs of turbines and associated electricity grids, as well as Operation and Maintenance (O&M) expenses [3]. However, clustering large groups of wind turbines results in aerodynamic coupling between individual turbines, known as the *wake effect*. Upstream turbines generate an airflow characterised by low velocity and increased turbulence intensity, affecting downstream turbines' performance. To mitigate revenue losses from the wake effect, maintaining sufficient spacing between turbines is crucial. However, expanding wind farm areas further leads to increased O&M costs and inefficient use of available sea space. Moreover, modification of existing wind farms is impractical. Therefore, *wake control* presents a solution to mitigate the wake effect and enhance overall power performance [4]. This chapter will delve into the wake effect and its associated control strategies. However, prior to delving into these topics, it is essential to explain the control mechanisms employed in individual wind turbines.

## 1-1 Individual Wind Turbine Control

As wind flows through a wind turbine, it undergoes a crucial conversion from kinetic energy available in the wind into rotational energy in the turbine's rotor. The rotor is connected to a generator in the turbine nacelle through a drivetrain, either directly or through a gearbox,

which transfers its flexibility to the deformation on the low-speed shaft [5]. This conversion is approximated using two quasi-stationary nonlinear equations that describe the aerodynamic torque and power as a function of air density $\rho$ [kg/m$^3$], surface area $A$ [m$^2$], free-stream wind velocity $U$ [m/s], blade pitch $\theta$ [°], tip-speed-ratio $\lambda$ [−], and yaw angle $\gamma$ [°]:

$$T = C_T(\theta, \lambda, \gamma)\frac{1}{2}\rho A U_\infty^2, \qquad P = C_P(\theta, \lambda, \gamma)\frac{1}{2}\rho A U_\infty^3 \tag{1-1}$$

The tip-speed-ratio (TSR), which is the ratio of the tangential speed at the blade tip to the free-stream wind velocity, can be controlled either fast by adjusting the generator torque $\tau$ or more slowly by adapting the blade pitch angles. The thrust force coefficient $C_T$ represents the thrust exerted by a wind turbine on the wind flowing through the rotor, while the power coefficient $C_P$ gives the ratio between the generated power and available power, essential for optimal power extraction [6]. Wind turbines cannot capture all of the wind's accessible energy, as some wind flow must be maintained behind the rotor. According to Betz-Joukowsky law, the theoretical maximum limit for wind turbine efficiency is approximately 59%. Thanks to advancements in wind turbine aerodynamics, particularly with the implementation of Blade-Element Momentum (BEM) theory with extensions of engineering rules, modern Horizontal Axis Wind Turbines (HAWT) have achieved power coefficients that closely approach this theoretical limit, reaching around 0.5 [7].

The operational states of a wind turbine can be categorised into three regions within its power capacity curve, which is determined by wind speed, as depicted in Figure 1-1. Region 1 corresponds to the start-up phase of the turbine. Once the wind speed exceeds the cut-in wind speed, Region 2 begins. In this region, the primary objective is to maximise power output by closely tracking the optimal tip-speed-ratio (TSR). Lastly, Region 3 spans the operational range from the rated wind speed to the cut-out speed. In this region, the turbine maintains a constant rotor speed at the optimal TSR to sustain rated power. Wakes in this region produce smaller velocity deficits because the turbine is already at maximum power and primarily limits its output. Although Region 3 represents the design operating point, most wind turbines in wind farms operate in Region 2 due to their waked state or site-specific wind conditions [8]. A turbine will be shut down after reaching the cut-out speed for safety reasons, as operating at too high a wind speed could damage the wind turbine.

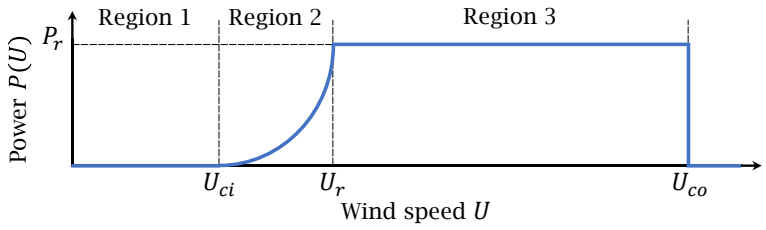


**Figure 1-1:** Representation of the Power Capacity Curve $P(U)$ depending on wind speed $U$ with cut-in speed $U_{ci}$, rated speed $U_r$, cut-out speed $U_{co}$ and rated power $P_r$.

Relying solely on the greedy control settings of wind turbines can restrict the attainment of optimal wind farm performance concerning specific control objectives, including power output maximisation, structural degradation minimisation, and active power control since the upstream turbine's wake could affect the downstream turbine. As a result, ongoing research is exploring alternative wind farm control strategies that coordinate the operation of individual

turbines and mitigate wake effects to optimise overall wind farm performance. Therefore, the remainder of this chapter will first conduct further investigation into the wake effect to gain a better understanding of the influence of wind flows downstream. Subsequently, the main categories of wind farm control strategies discussed in the literature will be explored.

## 1-2 Wake Effect

The wake effect is a well-known phenomenon in wind energy, characterised by a decrease in wind speed downstream of a wind turbine as the wind passes through the rotor disk. This phenomenon, illustrated in Figure 1-2, significantly impacts neighbouring turbines' performance and energy production [9]. The downwind region can be divided into the near-wake and the far-wake region. The near-wake region, immediately downwind of the turbine, has a highly complex, three-dimensional and heterogeneous flow distribution. The flow field in this region is notably affected by the characteristics of the turbine, including its blade profile and the geometry of the hub and nacelle. Conversely, because the far-wake region is situated further downstream, it is less influenced by the turbine features, and it can be more accurately predicted using global parameters like the thrust and power coefficient, along with incoming flow conditions [10].

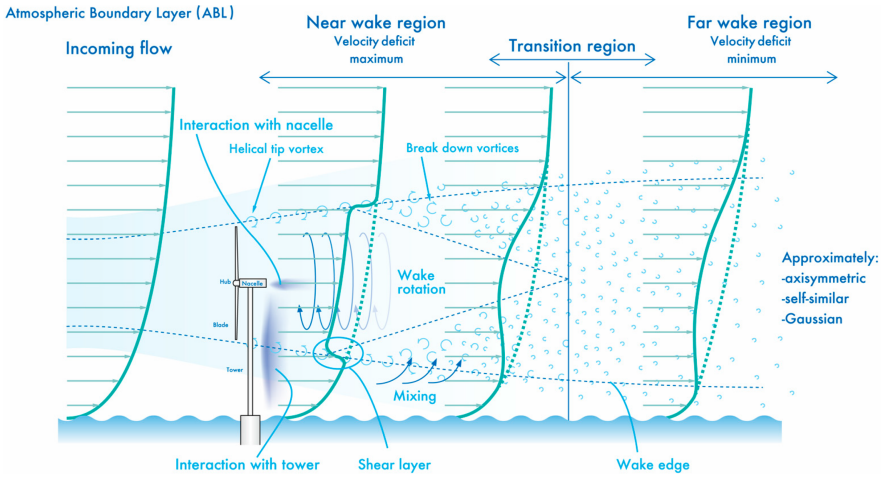


**Figure 1-2:** Schematic side view of wake structure behind a wind turbine, adapted from [11].

Several factors affect a turbine's wake behaviour, including inter-turbine spacing, wind speed and direction, turbulence intensity, and atmospheric stability. These factors cause downstream turbines to experience increased fatigue loads and reduced energy production by up to 12% in wind farms [8]. Therefore, accurate and efficient simulation of the wake's behaviour is critical for implementing wind farm control strategies. However, the complexity of the wake, including wind shear, kidney-shaped wakes, wake recovery, meandering, expansion, deflection, and skewing [6], make it impossible to describe the wake by a simple static velocity deficit field extending downstream in the wind direction. The velocity deficit is primarily influenced by wake deflection and the oscillatory characteristics of wake meandering. Wake deflection arises from momentum conservation, wherein yaw offset generates a transverse thrust force component that causes the wake to deflect. Small yaw angles induce lateral displacement of

the wake's centreline with minimal further impact on the wake's profile, while a tilt offset will result in a vertical displacement. However, highly yawed conditions can also cause significant changes to the wake profile, leading to deviations from the Gaussian shape. This results in a kidney-shaped cross-section due to a counter-rotating vortex pair. As a result, both lateral and vertical displacements may occur [12].

Another phenomenon, known as wake meandering, occurs when low-frequency variations in lateral and vertical turbulence components cause the wake centerline to shift, as illustrated in Figure 1-3. This phenomenon leads to changes in the wake immersion of downstream turbines. While the wake area appears to follow a Gaussian pattern in the near-wake region, wake meandering introduces temporal variation in the cross-sectional area of the wake in the far-wake region under unstable atmospheric conditions. This variability introduces significant uncertainty in power and load predictions [13]. However, meandering could also potentially enhance the available energy at the downstream turbine, owing to induced wake deflection and mixing [14]. Therefore, amplifying the existing meandering effect could accelerate the recovery of velocity deficits upstream. Consequently, the subsequent subsection will delve into wake meandering to gain a deeper understanding of its emergence and key characteristics.

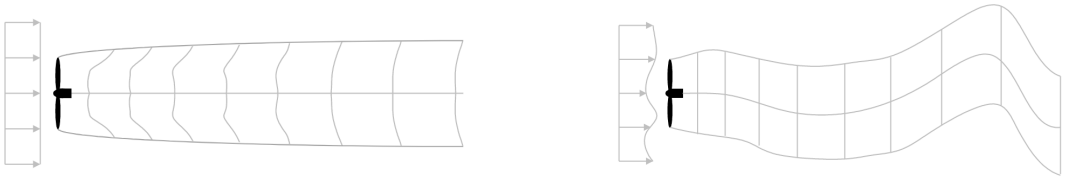

**Figure 1-3: Left**: Axisymmetric- and **Right**: Meandering wake deficit evolution, adapted from [15].

### 1-2-1 Wake Meandering

Wake meandering arises from two distinct mechanisms that operate at different scales [16]. The primary mechanism is driven by large-scale eddies within atmospheric turbulence, which passively advect downstream, resulting in large-scale effects on the wake, including lateral and vertical displacements. The secondary cause of meandering, though less pronounced, is associated with the shear layer's instability, similar to the vortex shedding observed behind bluff bodies. This induces small-scale effects in the wake, including increasing turbulence levels and additional structural loads on wind turbines, which are influenced by the turbine's geometry. The incoming flow conditions and turbine spacing influence large-scale meandering, while turbine operating conditions like TSR or yaw angle do not exert a direct influence [10].

Once the meandering effect is initiated, the lateral and vertical motion manifests as oscillations that shift towards lower frequencies with increasing amplitude [17]. Lateral movements are typically more pronounced, ranging from $10-50\%$, compared to vertical displacements. This discrepancy arises from the ground's blocking effect, limiting vertical wake movements and atmospheric turbulence. In the near wake, lateral displacement occurs within the range of $0 \sim A/D < 0.15$, while in the far wake, it averages around $A/D = 0.2$, but could extend up to an amplitude of $0.5D$ [18, 19]. Furthermore, as atmospheric instability increases, large-scale meandering becomes even more dominant in inducing meandering movements [13]. The

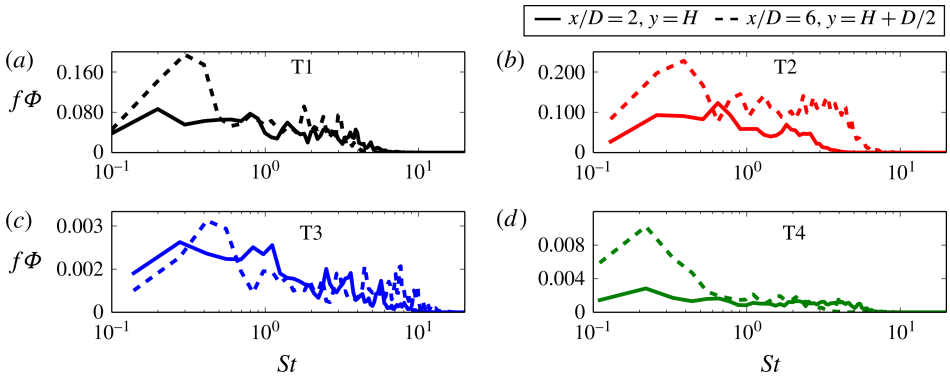


**Figure 1-4:** Premultiplied power density spectrum of the streamwise component of the velocity fluctuations at $x/D = 2$ and $x/D = 6$ for four different wind turbine designs with diameters ranging from wind tunnel scale (T1) to utility-scale (T4), adapted from [20].

small- and large-scale meandering effects correspond to distinct frequency ranges in oscillation energy, rather than a single dominant frequency associated with a single cause of meandering. Foti et al. [20] have demonstrated consistent Strouhal numbers, a dimensionless number to characterise the wake's excitation frequency, for both scales across a wide spectrum of turbine designs and rotor sizes, as can be seen in Figure 1-4. The small-scale effect, due to the interaction between the hub vortex and the shear layer, involves a spectrum with energetic contributions occurring at $St = fD/U = 0.35 - 0.6$, and a peak power observed at $St = 0.45$ [18]. The hub vortex interaction, while relatively subtle, maintains a lasting influence on the large-scale effect and serves as the trigger for the onset of wake meandering at a distance of twice the rotor diameter ($2D$). The energetic contribution of the large-scale meandering occurs at lower frequencies at $St = 0.15 - 0.3$. This aligns with the ranges identified by Howard et al. [21], as well as the Strouhal numbers of the large-scale effects in the far wake at a $x/D = 5$ by Medici and Alfredsson [22] in the range of $St = 0.15 - 0.25$, by Okulov and Sorensen [23] at a peak of 0.23, and Chamorro et al. [24] at 0.28. The contributions of both small- and large-scale meandering effects are evident in the Blade root Out-of-Plane moments observed at the downstream turbine. Therefore, there is potential to develop control strategies that exploit these effects directly, eliminating the need for surrogate wake models. The next section will explore various wind farm control strategies that could be employed to effectively control the meandering effect.

## 1-3 Control Strategies

Improving the overall performance of a wind farm by controlling the wake effect has been a subject of active research since the 1990s. One approach to achieving this goal is by operating wind turbines within the farm at configurations that differ from their individually optimal settings. Advanced wind farm control strategies, including Axial Induction Control, Wake Redirection Control, and Wake Mixing Control, have been developed for this purpose. These strategies may require operating turbines at suboptimal settings to improve the overall performance of the wind farm. The first two strategies mentioned, shown in Figure 1-5, have been more widely adopted, while the latter has been assessed more recently. The Axial Induction Control (AIC) strategy [25] is one of the earliest control strategies proposed for

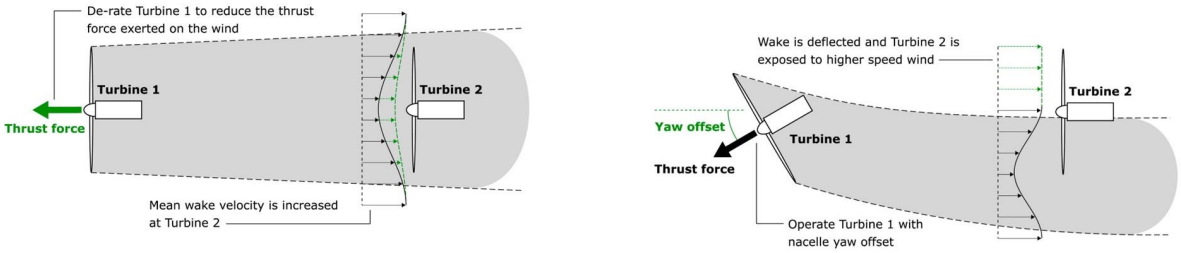


**Figure 1-5:** Top-view of two wind turbines aligned with the incoming free stream wind. Green elements highlight changes in turbine operation and wake conditions associated with each control concept for **Left:** wake induction, and **Right:** wake deflection, adapted and edited from [4].

wind farm control. It affects the wake and its downward interaction by intentionally derating the power generation of upstream turbines to reduce the induction factor by either increasing the blade pitch or operating at a suboptimal TSR. Consequently, downstream turbines can experience higher wind velocities, potentially resulting in increased energy production for the overall wind farm. However, reducing the thrust force of the upstream turbine also decreases wake turbulence, which is crucial for wake recovery, resulting in a further reduction in wind velocity downstream that may counteract the effect of upstream derating. Therefore, the effectiveness of the AIC strategy in contributing to increased power generation is, in practice, small to nonexistent [26]. Despite this, it could still benefit the longevity of turbines in a wind farm, as it can decrease turbine loading while maintaining the same power output.

A more promising strategy for increasing power production is Wake Redirection Control, involving deliberately misaligning the rotor of an upstream turbine with the incoming flow. This intentional misalignment causes the wake to deflect downstream, thus avoiding, either partially or completely, overlapping with a downwind turbine [27]. Misalignment is achieved through yawing or tilting the turbine, generating unsteady and asymmetric loads. The field of wake redirection is actively researched and has been investigated through experimental and field tests for both tilt and yaw misalignment. Yaw misalignment affects the loads, as partial wake overlap can increase fatigue of downstream turbines, while adjusting the tilt angle could lead to either load increases or decreases, depending on the angle [28]. Additionally, Fleming et al. [29] proposed Individual Pitch Control (IPC) to achieve a horizontal or vertical wake skew by intentionally inducing a yaw or tilt moment, refer to Figure 1-7. However, this could lead to a substantial increase in blade loading.

The latest control strategy, Wake Mixing Control, aims to intensify the turbulence within

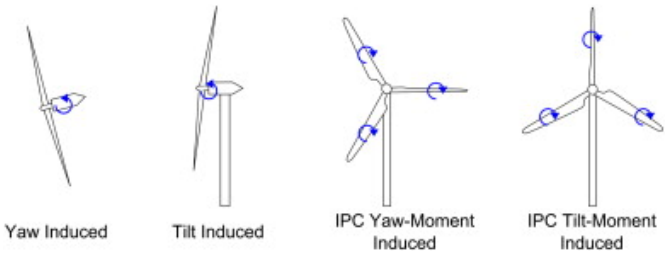


**Figure 1-6:** Techniques considered for redirecting the wake. The blue arrows indicate which component angles are being adjusted, adapted from [27].

the wake zone to increase interaction between the wake and the surrounding free-stream air, enabling enhanced energy recovery. Various strategies have been proposed, including the varying thrust force method [30] and Dynamic Induction Control (DIC) [31], which relies on slowly varying collective pitch angles. The latter, also referred to as the *pulse* method due to the periodic shedding of vortex rings behind the turbine, has shown improvements in energy extraction [32, 33], and has inspired a more recent approach. This novel method, called the *helix* approach [34], utilises Individual Pitch Control (IPC) in a sinusoidal manner to induce time-varying tilt and yaw moments, resulting in a helical-shaped wake. This wake configuration enhances wake mixing in the near wake region, but also increases deflection in the far region, thereby leading to a larger available kinetic energy at the downstream turbine [35]. Both DIC and IPC have proven their ability to significantly boost wind farm power capture by several percentage points. However, the use of pitch actuation and varying rotor thrust may impose additional loads on the turbine, potentially reducing its lifespan [36].

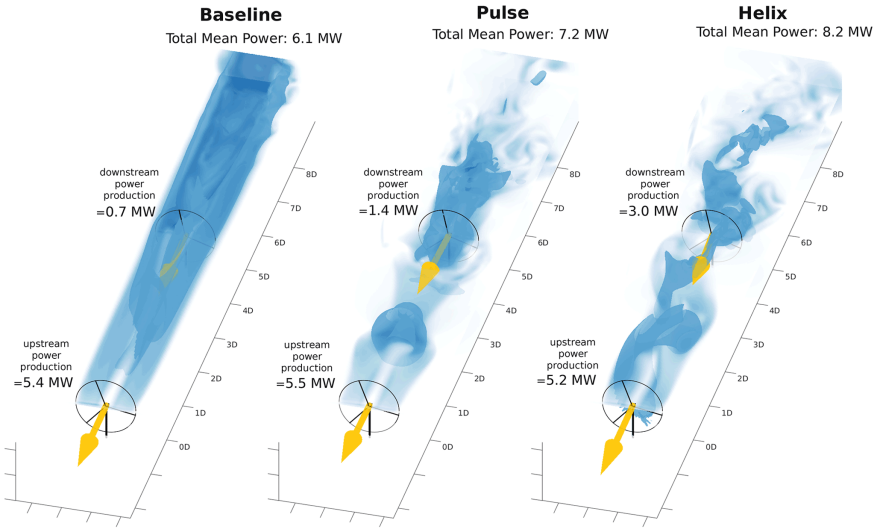


**Figure 1-7:** LES simulation of considered wake mixing techniques. **Left:** Baseline greedy control, **Middle:** Dynamic Induction Control or Pulse control, and **Right:** Helix control. Darker blue denotes iso-surfaces for specific wind velocities, while lighter blue represents absolute wind velocity. The distance between turbines is scaled by the rotor diameter $D$, adapted from [3].

In this context, Phase Synchronisation [37] has emerged as a promising approach. It offers the potential benefits of the helix approach with less pitch action by effectively leveraging the helix's periodic component already present in the wake induced by the upstream turbine. Through active control, this approach ensures a tight alignment between the response of the downstream turbine and the incoming wake, achieving synchronisation in phase. Consequently, in-phase synchronisation could increase the energy harnessed in the wake at the downstream turbine, resulting in overall improved power production [38]. Conversely, out-of-phase synchronisation could lower fatigue loads, thereby improving turbines' lifespan [39]. This principle could also be used to enhance or mitigate the meandering effect. However, while there has been some attention on applying phase synchronisation to enhance the effect of a helical wake, there has been little to no focus on enhancing the meandering effect, despite its inherent presence downstream and potential to accelerate wake recovery [40]. Additionally, existing phase synchronisation methods assume the periodic components to be constant, while

the meandering wake has a slowly time-varying excitation frequency. Hence, these methods are incapable of capturing the meandering effect. Therefore, further investigation is necessary for the application of phase synchronisation to the meandering effect. This begins by estimating the time-varying excitation frequency of the meandering wake. Hence, the next section will delve into adaptive filtering techniques capable of extracting this crucial information.

## 1-4 Adaptive Filtering Techniques

Achieving real-time and accurate estimation of the slowly time-varying characteristics of meandering is crucial for successfully implementing phase synchronisation. This task can be accomplished by applying adaptive filtering techniques, which can be broadly categorised into model-based and model-free approaches. Model-based methods rely on a model of the wind farm dynamics to predict turbine−wake interactions and achieve accurate estimates. Conversely, model-free adaptive filters do not require such a model. Instead, they rely on real-time measurements of the wind turbine's inputs and outputs to estimate the system parameters, making them more adaptable to various wind speed and flow conditions.

In the domain of phase synchronisation, Ottenheym [38] has successfully applied both model-based and model-free methods. The Recursive Least Squares (RLS) Based Estimator [41], a model-free method, recursively solves a weighted least squares problem online while implementing a forgetting factor to reduce the effect of past data and adapt to new system dynamics. While this method is easy to implement and adaptive, it faces limitations in directly estimating the phase of an incoming wake, instead estimating the combined phase of the wake inflow and controller effort. On the other hand, the Kalman Filter (KF) Based Estimator could directly estimate the wake's phase by augmenting the periodic components of the helical wake in the system's state space [42]. Although both methods have shown promise, their reliance on a constant wake frequency limits their capacity to capture the slowly time-varying frequency of the meandering wake. Dong et al. [43] expanded upon the Kalman Filter to estimate the lateral and vertical wake position by incorporating an EKF with the dynamics of the Dynamic Wake Meander (DWM) model. This framework has demonstrated accurate tracking of the wake centre, even in scenarios involving the yaw-misalignment of downstream wind turbines. However, its reliance on the DWM model adds complexity to the method. Other KF-extensions offer promising options for accurately capturing the unsteady behaviour of the meandering wake. The non-steady state Kalman Filter [42] focuses on estimating ambient and periodic excitation of structural modes in a mechanical system, enhancing the precision of tracking periodic components. Another extension addresses estimating the frequency of a harmonic signal with time-varying amplitude and frequency, even in the presence of noisy measurements and broadband stationary noise [44]. Additionally, Phan et al. [45] introduced a novel state-space model in an EKF scheme that considers the positive and negative components of a three-phase system, along with the variation of phase angle between consecutive iterations. This model facilitates the estimation of (un)balanced three-phase systems, rendering it suitable for estimating harmonic content in real-time applications.

While model-based approaches excel in capturing the time-varying behaviour of the meandering wake, their performance is contingent upon the accuracy of the model employed for estimation. If wind or operational conditions deviate from those the model was constructed

for, it may result in inaccurate estimates. Consequently, attention turns towards model-free methods used for phase synchronisation from other fields. One such method widely employed in electronics and signal processing systems is a Phase-Locked Loop (PLL). A PLL is a closed-loop control system that locks its output to its input. It excels at tracking the phase angle of the input signal's fundamental component and provides vital information about grid voltage, including frequency, phase, and amplitude. Various forms of PLLs exist, all featuring three essential components visualised in Figure 1-8: the Phase Detection (PD) stage to generate a signal indicating the difference between actual and estimated phases, the Loop Filter (LF) stage to mainly suppress disturbances within the PLL control loop and dictate dynamic response, tracking characteristics, and stability, and finally, the Voltage-Controlled Oscillator (VCO) stage to produce the synchronised signal corresponding to the PLL input.

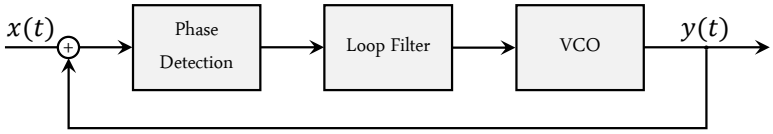


**Figure 1-8:** Overview of a Phase-Locked Loop with its three stages: the Phase Detection, Loop Filter, and Voltage-Controlled Oscillator (VCO) stage to produce the synchronised signal $y(t)$ corresponding to the PLL input $x(t)$.

Utilising Single-Phase PLLs (*1*$\phi$-PLL) designed to synchronise with single-frequency input signals, such as the periodic variations in tilt and yaw moments, enables precise phase synchronisation of the meandering effect. Among these *1*$\phi$-PLL, the Second-Order Generalized Integrator-Phase-Locked Loop (SOGI-PLL) has garnered significant attention for its simplicity, filtering capability, and adaptability to various frequencies [46]. The straightforward structure of the SOGI-PLL facilitates easy implementation and adaptability to specific grid conditions, while its robust filtering ability, inherent to the SOGI-component, enhances its robustness to harmonics compared to other methods [47]. Moreover, its suitability for handling non-ideal sinusoidal signals and adaptability to varying frequencies make it particularly effective for the application of phase synchronising to the time-varying meandering effect. In the next section, the potential of applying phase synchronisation to wake meandering will be further discussed.

## 1-5 Problem Formulation and Research Outline

Employing phase synchronisation to the meandering effect downstream holds promise for enhancing wind farm performance while simultaneously reducing control costs. This approach leverages the inherent presence of the meandering effect, offering a strategy similar to the existing phase synchronisation method [37], but without requiring the application of the helix approach on the upstream turbine. Amplifying the meandering effect holds promise for enhancing wake mixing and deflection, thereby accelerating wake recovery and improving overall power output across the wind farm. Conversely, mitigating the meandering effect could decrease fatigue loads on the turbines, ultimately prolonging the operational lifespan of the wind turbines. Therefore, this thesis seeks to explore the potential of integrating phase synchronisation with the meandering effect. This will be done by addressing the research questions outlined in the subsequent subsection.

### 1-5-1 Research Questions

This MSc Thesis will focus on utilising phase synchronisation on the downstream turbine to harness the effect of the meandering wake. Therefore, the main research question is formulated as follows:

*How can the meandering effect of an incoming wake be harnessed at the downstream turbine to enhance overall performance?*

---

Given that phase synchronisation will be applied in real-time applications, accurately tracking the time-varying meandering nature using key characteristics such as phase, frequency, and amplitude is crucial. Therefore, deriving the parameters needed to track the wake's position from the available inflow information at the downstream turbine will be explored. Furthermore, analysing the effect of enhancing the meandering effect is essential. Therefore, the sub-questions are as follows:

1. *How can wake meandering be identified based on inflow information at the downstream turbine?*
2. *How can phase synchronisation be effectively initiated to accommodate the time-varying nature of meandering wake?*
3. *What impacts does enhancing the meandering effect have on power performance and fatigue loads?*

By addressing these research questions, this thesis aims to provide valuable insights into the harnessing of meandering wakes and their impact on wind farm performance, ultimately contributing to the advancement of wind farm control strategies. The next subsection will give the structure of this report.

### 1-5-2 Report Structure

This report will address the formulated main and sub-research questions through the following structure:

- **Chapter 2** discusses fundamental concepts necessary for effectively utilising phase synchronisation at the downstream turbine. This includes mathematical transformations to preprocess the effect of meandering for phase synchronisation, the construction of an adaptable filtering technique to estimate wake characteristics, and the design procedure of our proposed control strategy.
- **Chapter 3** validates the performance of our methodology using a lower-order model with known dynamics, providing insights into the limits of our controllers.
- **Chapter 4** presents the higher-order experiment to test our control strategy in a wind turbine simulation environment. The results will provide insight into the performance of our control strategy for enhancement of the meandering effect.
- **Chapter 5** offers the final conclusion, addressing the formulated main and sub-research questions, and providing recommendations for future research.

# Chapter 2

# Preliminaries and controllers

A comprehensive understanding of fundamental concepts is vital for effectively utilising phase synchronisation to enhance the meandering wake effect. This chapter explores various aspects of the framework crucial for this purpose. Firstly, preliminary knowledge about the Multi-Blade Coordinate transformation will be explored in Section 2-1. This will cover the different reference frames and the transformations between them, a crucial component applied at various stages in modelling our method. Subsequently, in Section 2-2, the analysis focuses on the meandering effect on the downstream turbine. In Section 2-3, the introduction of a Phase-Locked Loop capable of estimating time-varying frequency while synchronising with the wake's phase is presented. Finally, the closed-loop control strategy of the system is discussed in Section 2-4.

## 2-1 Multi-Blade Coordinate Transform

The incoming meandering wake induces dynamic loads on the rotor disk, embedding valuable wake information in the bending moments of rotor blades. This information can be used to synchronise the downstream turbine to the effect of the meandering. However, a complication arises as the meandering oscillations are induced on the rotor disk while it is simultaneously rotating. Furthermore, the lateral and vertical meandering effects must be controlled using the pitch angles of the three rotating blades. This leads to a highly coupled Multiple-Input Multiple-Output (MIMO) problem, where the control action of one pitch angle influences both tilt and yaw axes. Therefore, the objective is to transform the blade's pitch angles from a rotating three-axis framework to a non-rotating two-axis frame. This enables the application of control actions directly to the non-rotating lateral and vertical meandering effect.

Achieving this decoupling involves using a Multi-Blade Coordinate (MBC) transform, effectively separating the highly coupled MIMO structure into two easier implementable Single-Input Single-Output (SISO) systems. Originating from other fields, the MBC transform is often known as the Park transformation. In electrical engineering, this transformation simplifies problems in three-phase synchronous machines. Similarly, the MBC will be used to

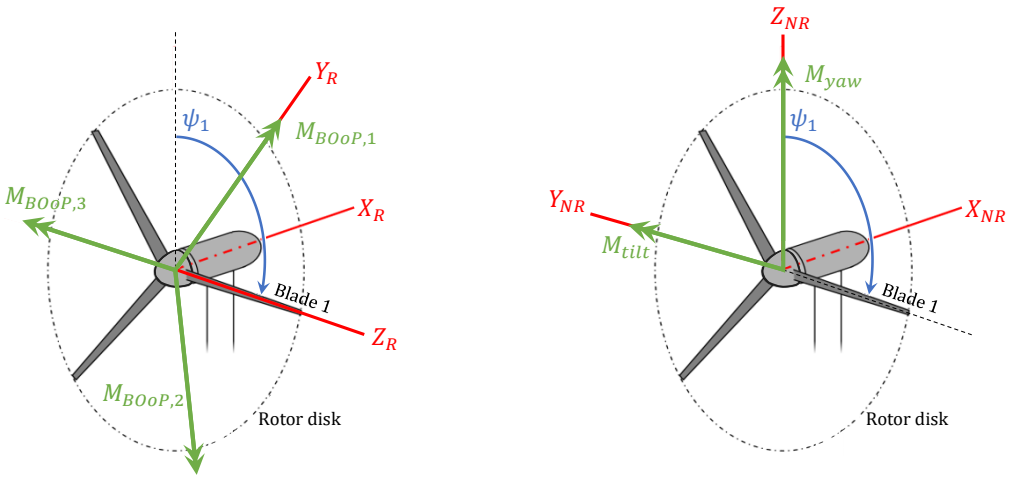


**Figure 2-1:** Schematic representation of the bending moments with **Left:** rotating BOoP moments in the $abc$-frame, and **Right:** nonrotating tilt and yaw moments in the $dq0$-frame.

transform the bending loads on the three rotating blades of a wind turbine in a two-axis frame. Before delving into the application of the MBC transform in our system, an exploration of different reference frames and their characteristics is necessary to gain a better understanding of their applications, as they will also be utilised in the SOGI-PLL, which will be discussed in Section 2-3.

### 2-1-1 Relationship between reference frame

Transformations from the $abc$-frame to the stationary $\alpha\beta0$ or rotating $dq0$-frame are widely applied to analyse three-phase systems. These transformations share a common objective of translating a rotating multi-element to an orthogonal two-axis reference frame, resulting in two signals and a zero-component representing $abc$ signals' mean. This simplification not only facilitates mathematical computations but also provides valuable insights into the specific components of the signal. The relationship between different frames is depicted in Figure 2-2:

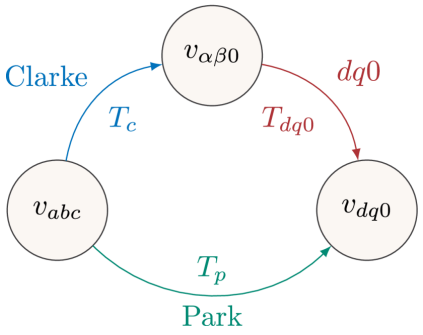


**Figure 2-2:** Relationships between the three-axis reference frame ($abc$-frame), stationary orthogonal two-axis reference frame ($\alpha\beta0$-frame) and rotating orthogonal two-axis reference frame ($dq0$-frame), adapted from [48].

The Clarke transform $T_c$ converts the three 120°-phase-shifted $abc$ signals into the stationary orthogonal two-axis reference frame ($\alpha\beta 0$-frame). The stationary $\alpha\beta 0$ signals can also be described in terms of the rotating orthogonal two-axis reference frame ($dq0$-frame) using the $T_{dq0}$ transformation. The mathematical models of the Clarke and $dq0$ transform are given by

$$\underbrace{\begin{bmatrix} v_\alpha \\ v_\beta \\ v_0 \end{bmatrix}}_{v_{\alpha\beta 0}} = \underbrace{\frac{2}{3}\begin{bmatrix} 1 & -\frac{1}{2} & -\frac{1}{2} \\ 0 & \frac{\sqrt{3}}{2} & -\frac{\sqrt{3}}{2} \\ \frac{1}{2} & \frac{1}{2} & \frac{1}{2} \end{bmatrix}}_{T_c} \underbrace{\begin{bmatrix} v_a \\ v_b \\ v_c \end{bmatrix}}_{v_{abc}} \quad \text{and} \quad \underbrace{\begin{bmatrix} v_d \\ v_q \\ v_0 \end{bmatrix}}_{v_{dq0}} = \underbrace{\begin{bmatrix} \cos(\theta) & -\sin(\theta) & 0 \\ \sin(\theta) & \cos(\theta) & 0 \\ 0 & 0 & 1 \end{bmatrix}}_{T_{dq0}(\theta)} \begin{bmatrix} v_\alpha \\ v_\beta \\ v_0 \end{bmatrix} \tag{2-1}$$

Figure 2-2 shows the effect of a three-phase signal in the different reference frames. It can be seen that the $\alpha\beta 0$-frame gives us information about the dc components of the signal, while the $dq0$-frame can provide information about the rotating components. This information will be useful for further applications in our constructed method.

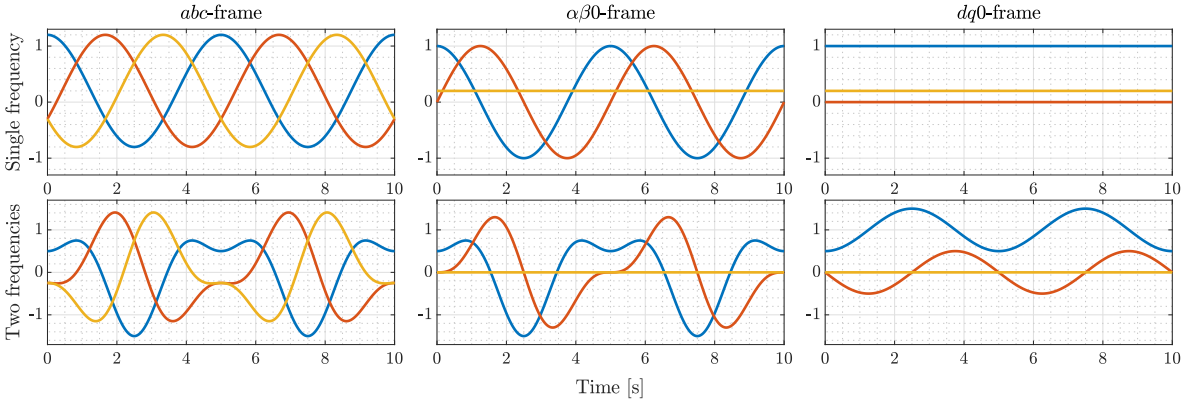


**Figure 2-3:** Time-domain interpretation of two three-phase signals. **Top:** balanced signal with a constant frequency with phase delay and bias, and **Bottom:** unbalanced signal with the sum of two signals with different amplitude, frequencies and phase delay, for **Left:** the $abc$-frame, **Middle:** $\alpha\beta 0$-frame, and **Right:** $dq0$-frame.

### 2-1-2 MBC for phase synchronisation

The $abc$ quantities can also be directly transformed to $dq0$ by consecutively applying the Clarke and $dq0$ transform. This transform is called the Park transformation $T_p$, or as aforementioned, the MBC transform when applied to wind turbines. The MBC is used to transform the rotating Blade root Out-of-Plane (BOoP) moments $M_i$ where $i \in \{1, 2, 3\}$ onto the stationary tilt and yaw moment (refer to Figure 2-1):

$$\underbrace{\begin{bmatrix} M_{\text{tilt}}(t) \\ M_{\text{yaw}}(t) \\ M_0(t) \end{bmatrix}}_{M_{dq0}(t)} = \underbrace{\frac{2}{3}\begin{bmatrix} \cos(\psi(t)) & \cos(\psi(t)+\frac{2\pi}{3}) & \cos(\psi(t)+\frac{4\pi}{3}) \\ \sin(\psi(t)) & \sin(\psi(t)+\frac{2\pi}{3}) & \sin(\psi(t)+\frac{4\pi}{3}) \\ \frac{1}{2} & \frac{1}{2} & \frac{1}{2} \end{bmatrix}}_{T(\psi(t))} \underbrace{\begin{bmatrix} M_1(t) \\ M_2(t) \\ M_3(t) \end{bmatrix}}_{M_{\text{BOoP}}(t)} \tag{2-2}$$

where the obtained collective mode $M_0(t)$ represents the blades' out-of-plane flapping moment. The cyclic modes $M_{dq}(t)$, represent the tilting moment $M_{\text{tilt}}(t)$ (rotor fore-aft tilt) about the

horizontal axis and the yawing moment $M_{\text{yaw}}(t)$ around the vertical axis (rotor side-side coming). Additionally, $\psi(t)$ denotes the rotor azimuth angle for the first blade, with $\psi(t) = 0$ as the vertical upright position. Our control strategy, detailed in Section 2-3 and 2-4, is applied to the cyclic modes $M_{dq}(t)$ to enhance the meandering effect. This yields two control actions formulated as tilt and yaw pitch angles, as illustrated in Figure 2-4. To map the tilt and yaw pitch angles to the cyclic modes effectively, the non-rotating transfer function $C(s, \psi)$ is utilised in the frequency domain:

$$\begin{bmatrix} M_{\text{tilt}}(s) \\ M_{\text{yaw}}(s) \end{bmatrix} = \underbrace{\begin{bmatrix} C_{12}(s,\psi) & C_{12}(s,\psi) \\ C_{21}(s,\psi) & C_{22}(s,\psi) \end{bmatrix}}_{C(s,\psi)} \begin{bmatrix} \theta_{\text{tilt}}(s) \\ \theta_{\text{yaw}}(s) \end{bmatrix} \tag{2-3}$$

However, to integrate these angles into the wind turbine's control action, they need to be translated into a three-axis reference frame. This translation is accomplished using the inverse MBC transformation. Here, individual pitch angles $\theta_i(t)$ for $i \in 1, 2, 3$ are derived from the collective pitch angle $\theta_0(t)$ and the control effort provided in terms of $\theta_{\text{tilt}}(t)$ and $\theta_{\text{yaw}}(t)$:

$$\underbrace{\begin{bmatrix} \theta_1(t) \\ \theta_2(t) \\ \theta_3(t) \end{bmatrix}}_{\theta(t)} = \underbrace{\begin{bmatrix} 1 & \cos(\psi(t) + \frac{2\pi}{3}) & \sin(\psi(t) + \frac{2\pi}{3}) \\ 1 & \cos(\psi(t) + \frac{4\pi}{3}) & \sin(\psi(t) + \frac{4\pi}{3}) \\ 1 & \cos(\psi(t)) & \sin(\psi(t)) \end{bmatrix}}_{T^{-1}(\psi(t))} \underbrace{\begin{bmatrix} \theta_{\text{tilt}}(t) \\ \theta_{\text{yaw}}(t) \\ \theta_0(t) \end{bmatrix}}_{\theta_{dq0}(t)} \tag{2-4}$$

In practical scenarios, there remains some coupling between the tilt and yaw axes due to phase lag caused by coupling and actuator delays. This implies that applying SISO control configurations would not suffice. Introducing an azimuth offset $\psi_{\text{off}}$ in the inverse MBC effectively reduces this coupling. By maximising the main-diagonal terms in (2-3) and minimising the off-diagonal terms, it minimises the coupling between the control inputs, leading to reduced phase lag [49]. Consequently, it allows us to continue using the easier-to-control SISO configuration. Figure 2-4 provides an overview of the control steps outlining the necessary procedures for constructing individual pitch angles from the measured BOoP moments. The subsequent section will further explore the impact of the meandering wake on the downstream turbine to get a better understanding of how to extract the meandering characteristics and construct its control action.

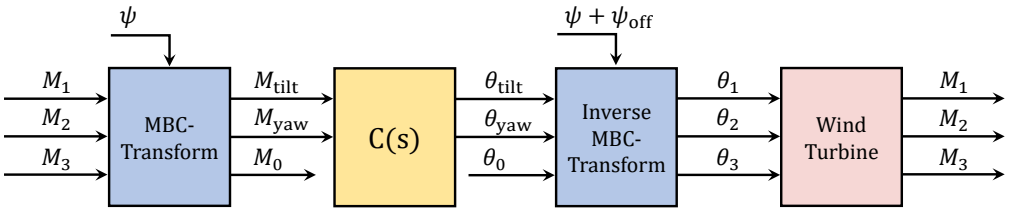


**Figure 2-4:** Schematic representation of the use of the MBC transformation to achieve periodic yaw and tilt moments on the turbine rotor.

## 2-2 Wake interaction on Downstream Turbine

This section delves deeper into the impact of the meandering effect on downstream wind turbines, considering its rotation direction either in the Clockwise (CW) or Counterclockwise

(CCW) direction, which affects the mathematical representation of the cyclic modes $M_{dq}(t)$. These modes are expressed as follows:

$$M_{dq}^{\mathrm{CW}}(t) = \begin{cases} A_{\mathrm{tilt}} \sin\left(\theta_e(t)\right) + b_{\mathrm{tilt}} \\ A_{\mathrm{yaw}} \cos\left(\theta_e(t)\right) + b_{\mathrm{yaw}} \end{cases} \quad \text{and} \quad M_{dq}^{\mathrm{CCW}}(t) = \begin{cases} A_{\mathrm{tilt}} \sin\left(\theta_e(t)\right) + b_{\mathrm{tilt}} \\ -A_{\mathrm{yaw}} \cos\left(\theta_e(t)\right) + b_{\mathrm{yaw}} \end{cases} \tag{2-5}$$

where $A_{\mathrm{tilt}}$ and $A_{\mathrm{yaw}}$ indicate the amplitude of the tilt and yaw moments, $b_{\mathrm{tilt}}$ and $b_{\mathrm{yaw}}$ represent their respective offsets, and $\theta_e(t) = \omega_e(t)t + \varphi$ represents the phase of the periodic load and $\varphi$ denotes its phase delay. The excitation frequency $\omega_e(t) = 2\pi f_e(t)$ of the wake can be determined using the relation:

$$f_e = \frac{St \cdot U_\infty}{D} \tag{2-6}$$

where $f_e$ is given in Hz, $St$ is the dimensionless Strouhal number, $U_\infty$ represents the ambient wind speed in m/s, and $D$ is the rotor diameter in m. The relationship given in (2-6) helps determine the frequency range of the meandering effect, as the Strouhal number typically ranges between 0.15 and 0.25 for meandering. This insight guides the design of phase synchronisation control methods to enhance the meandering effect, either by amplifying or attenuating the amplitude of the tilt and yaw moments. Furthermore, note that the sign of $M_{\mathrm{yaw}}$ in (2-5) changes between CW and CCW rotation. Therefore, careful consideration is necessary when constructing the control effort, which will be further explored in Section 2-4. The subsequent section will delve into the method used to estimate the time-varying excitation frequency of the meandering wake.

## 2-3 Second-Order Generalized Integrator Phase-Locked Loop

The preceding sections outlined the framework for converting the coupled MIMO-structure into two manageable decoupled SISO configurations using a MBC transformation. Subsequently, the interaction of tilt and yaw moments on the downstream turbine was explored to get a better understanding of enhancing the meandering effect. Therefore, the next step involves designing a framework capable of phase synchronising the time-varying nature of the meandering wake. To achieve this goal, the Second-Order Generalized Integrator Phase-Locked Loop (SOGI-PLL), illustrated in Figure 2-5, will be applied to our system.

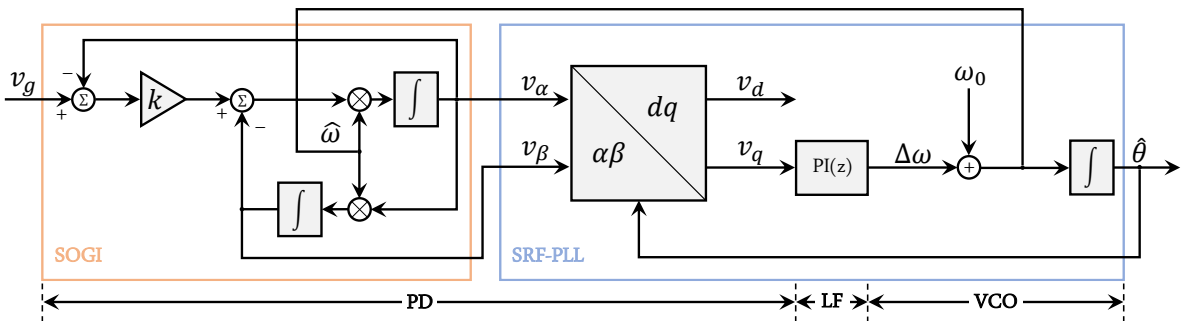


**Figure 2-5:** Overview of the Second-Order Generalized Integrator Phase-Locked Loop.

However, its suitability requires further exploration. This includes assessing its behaviour in mitigating the impact of an offset in the wake's centreline, which could induce fluctuations in the estimated phase and frequency, and addressing frequency- and phase jumps caused by the slowly time-varying meandering wake. Hence, the subsequent subsections will undertake a comprehensive analysis of the Phase Detection, Loop Filter, and Voltage-Controlled Oscillator components of our PLL, discussing specific improvements made to optimise its performance within the context of our system.

### 2-3-1 Phase Detection

The first component of the SOGI-PLL structure is the Phase Detection (PD). This part produces an output proportional to the phase error between the estimated phase and its actual value. If the phase error is zero, the system response is synchronised to the incoming signal's phase ($\hat{\omega} = \omega$). This is called the *quasi-locked* state. The conventional SOGI structure, refer to Figure 2-5, converts the input signal $v(t)$ in the quasi-locked state into two quadrature signals, $v_\alpha(t)$ and $v_\beta(t)$. This is done by employing two second-order filters, Bandpass Filter (BPF) $G_\alpha(s)$ and Lowpass Filter (LPF) $G_\beta(s)$, with unity gain and, respectively a zero and 90° phase shift at the resonance frequency $\hat{\omega}$:

$$G_\alpha(s) = \frac{v_\alpha(s)}{v(s)} = \frac{k\hat{\omega}s}{s^2 + k\hat{\omega} + \hat{\omega}^2}, \qquad \text{and} \qquad G_\beta(s) = \frac{v_\beta(s)}{v(s)} = \frac{k\hat{\omega}^2}{s^2 + k\hat{\omega} + \hat{\omega}^2} \tag{2-7}$$

where $k = 2\xi$ is the damping factor, and $\hat{\omega}$ is the filter's centre frequency. The adaptive feedback loop, incorporating the estimated frequency $\hat{\omega}$, ensures the filters' centre frequency continually aligns with the time-varying input signal's frequency.

This adaptability makes the PLL suitable for systems with time-varying frequencies. The only design parameter of (2-7) includes damping ratio $\xi$. The damping ratio influences the bandwidth of the filters, influencing the filters' bandwidth, as illustrated in Figure 2-6. Increasing the value of damping factor $k$ diminished the resonant peak, as depicted in the magnitude plots, leading to a narrower bandwidth and faster response. Furthermore, the

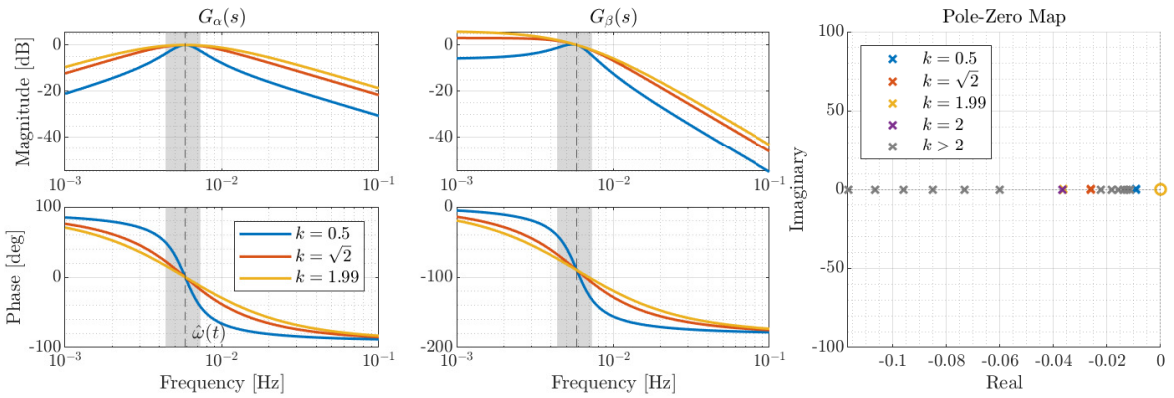


**Figure 2-6:** Bode plots of **Left:** $G_\alpha(s)$ and **Middle:** $G_\beta(s)$ of the SOGI structure for various damping factors $k$ and centre frequency $\hat{\omega}$ where the meandering frequency range is specified with the grey region for $St = [0.15\ 0.25]$ and $U_{hub} = 9$ m/s. **Right:** Pole-zero map of the filters of the conventional SOGI structure for various damping factors $k$.

pole-zero map illustrates that increasing $k$ causes the complex-conjugated pole pair to move away from the imaginary axis towards the real axes, confirming enhanced stability and faster dynamic response. However, the trade-off is that higher values of $k$ compromise the filtering ability, causing a decline in rejection capability at higher frequencies. Furthermore, beyond $k = 2$, all the poles lie on the real axis, split into two parts. One part moves significantly away from the imaginary axis, while the other converges towards the imaginary axis, becoming the dominant pole. This shift indicates that for $k \geq 2$, the stability and dynamic response will deteriorate. Therefore, a damping factor of $k < 2$ is recommended [50]. A value of $k = \sqrt{2}$ is often chosen to achieve critical damping as it is an optimal compromise between the transient response and filtering performance.

Enhancing the system's stability also involves addressing the presence of a dc offset, a crucial consideration in the overall design since offsets commonly exist in practical input signals. Since, as aforementioned, the presence of dc offset could lead to fundamental frequency oscillations in the estimated phase and frequency, potentially impacting the system's accuracy. To mitigate this effect, it becomes imperative to implement additional refinements to the conventional SOGI structure. Now, let the input signal $v(t)$ take the form of a biased sine wave:

$$v(t) = A \sin(\omega t + \varphi) + b \tag{2-8}$$

where $\omega$ is the input signal's frequency, $\varphi$ the phase delay, $A$ the sine wave's amplitude and $b$ the dc offset. In the $s$-domain, the input signal can be expressed as:

$$\mathcal{L}\{v(t)\} := v(s) = \frac{A(\sin\varphi + s\sin\varphi)}{s^2 + \omega^2} + \frac{b}{s} \tag{2-9}$$

Now, if the inverse Laplace transform is applied to (2-7) and (2-9), the steady-state output of $v_\alpha(t)$ and $v_\beta(t)$ can be obtained by

$$v_{\alpha\infty}(t) = a^* A \sin(\omega t + \varphi + \varphi^*), \qquad v_{\beta\infty}(t) = kb - a^* \frac{\hat{\omega}}{\omega} A \cos(\omega t + \varphi + \varphi^*) \tag{2-10}$$

where the attenuation factor $a^*$ and the phase shift $\varphi^*$ are determined by

$$a^* = \frac{k\hat{\omega}\omega}{\sqrt{k^2\hat{\omega}^2\omega^2 + (\hat{\omega}^2 - \omega^2)^2}}, \qquad \varphi^* = \arctan\frac{\hat{\omega}^2 - \omega^2}{k\hat{\omega}\omega}$$

It is important to note that the negative cosine in (2-10) means that the $\alpha$-axis in the $\alpha\beta 0$-frame is mirrored to its conventional orientation. However, this has no impact on the dynamics within the PLL, so no additional actions are required. In a quasi-locked state, as observed from (2-10), the system exhibits no attenuation ($a^* = 1$) and zero phase delay ($\varphi^* = 0$). Conversely, when the system is not synchronised, the output signals' amplitudes experience attenuation ($a^* < 1$), accompanied by a phase lead or delay ($\varphi^* \neq 0$). This observation aligns with the visual representation in Figure 2-6. Furthermore, (2-10) reveals that in both states, the conventional SOGI structure fails to eliminate the dc offset for $G_\beta(s)$, as indicated by the $kb$ term in the equation. This offset, represented by $kb$, introduces an error in amplitude detection, subsequently impacting the follow-up PLL operation during low-frequency oscillation. To overcome this limitation, improvements to the conventional SOGI structure are necessary to eliminate the dc offset. Additionally, these improvements must also include the capability to estimate the dc offset to compensate for it in a closed-loop control

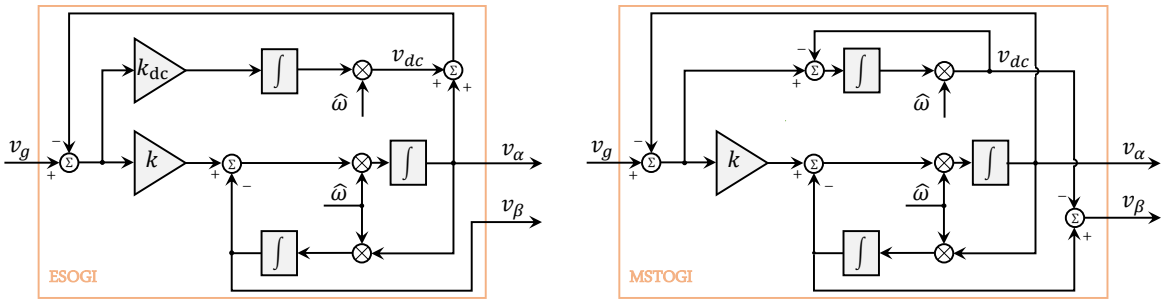


**Figure 2-7:** Block structure of **Left:** ESOGI-, and **Right:** MSTOGI-module.

configuration, which will be discussed in Section 2-4. Two of such methods are illustrated in Figure 2-7.

The Extended Second-Order Generalized Integrator (ESOGI) [51] integrates the estimation of the dc offset as an additional state by introducing a third integrator with a $k_{dc}\hat{\omega}$-gain. The estimated dc offset, denoted as $v_{dc}$, is then included in the feedback loop of $v_\alpha$ and subtracted from the input signal to augment the dc offset rejection capability. The detailed derivations of the ESOGI's transfer functions, presented comprehensively in Appendix A-1-1, are expressed as follows:

$$G_\alpha(s) = \frac{k\hat{\omega}s^2}{\Delta_1(s)}, \qquad G_\beta(s) = \frac{k\hat{\omega}^2 s}{\Delta_1(s)}, \qquad G_{dc}(s) = \frac{v_{dc}(s)}{v_g(s)} = \frac{k_{dc}\hat{\omega}(s^2+\hat{\omega}^2)}{\Delta_1(s)} \tag{2-11}$$

where $\Delta_1(s) = s^3+(k+k_{dc})\hat{\omega}s^2+\hat{\omega}^2 s+k_{dc}\hat{\omega}^3$, and $k_{dc}$ is the gain in dc offset estimate. Karimi-Ghartemani et al. [51] suggest tuning gain $k_{dc}$ by examining the poles of $\Delta_1(s)$. Choosing these poles as one real pole $m\alpha$ and a complex conjugate pair $\alpha \pm j\beta$, the characteristics equation can be obtained by

$$\Delta_1(s) = (s+m\alpha)\left(s^2+2\alpha s+(\alpha^2+\beta^2)\right) \tag{2-12}$$

This results in the following relations:

$$(k+k_{dc})\hat{\omega} = (m+2)\alpha, \qquad \hat{\omega}^2 = (2m+1)\alpha^2+\beta^2, \qquad k_{dc}\hat{\omega}^3 = m\alpha(\alpha^2+\beta^2) \tag{2-13}$$

A direct correlation between $k_{dc}$ and $m$ can be seen in the third relation in (2-13). As $m$ increases, $k_{dc}$ increases, and vice versa. Furthermore, the first relation implies that for a given value of $m$, $k$ decreases as $k_{dc}$ increases, and vice versa. Consequently, increasing $m$ results in a higher $k_{dc}/k$-ratio. Selecting $m < 1$ shifts the real pole to the right of the complex pole pair, making it the dominant pole. Visual representations are provided in Figure 2-8. Choosing an inappropriate value for $m$ could result in a greater imbalance between fast dynamics response and good transient performance. An increase in $k_{dc}$ would provide fast dc offset estimation but introduces oscillatory behaviour in the PLL's estimations. A $k_{dc}$ significantly smaller than $k$ is recommended to balance fast dynamics response and good transient performance [51]. The solution for $k_{dc}$ in terms of $k$ and $m$ can be obtained by:

$$k_{dc}^3+3kk_{dc}^2+\left(3k^2+\left(\frac{m+2}{m}\right)^2\right)k_{dc}+\left(k^3-\frac{(m+2)^2}{2m}k\right) = 0 \tag{2-14}$$

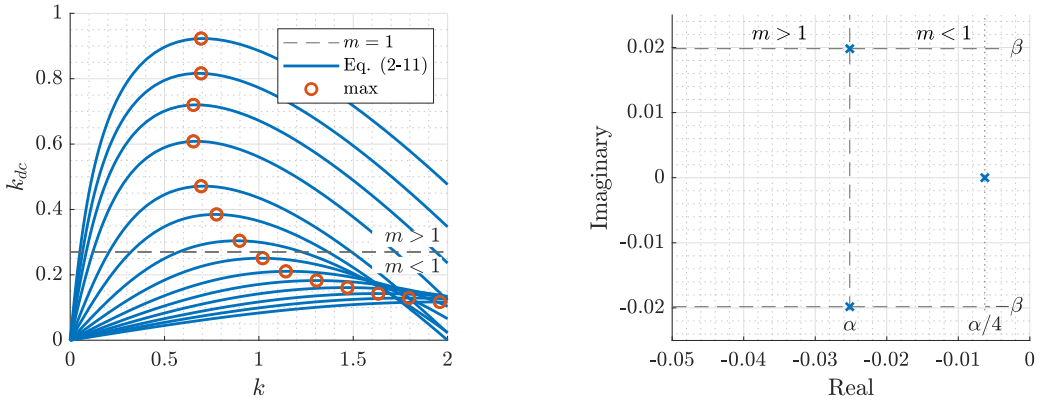


**Figure 2-8:** Design of $k_{dc}$ with **Left:** $k$ vs. $k_{dc}$ based on (2-14) for various multiplication factors $m$, and **Right:** pole map of (2-12) in terms of $m$, $\alpha$ and $\beta$.

Please refer to Appendix A-2 for the complete derivation. Tuning the dc offset gain $k_{dc}$ with $m$ and $k$ using (2-14) leads to the bode plots shown in Figure 2-9. Similar to the SOGI structure, a lower damping factor will narrow the bandwidth but result in a longer response time. Furthermore, it can seen that $G_{dc}(s)$ is a Notch Filter (NF) with a stop band centred at the estimated frequency $\hat{\omega}$. The large negative magnitude of $G_{dc}(s)$ at $\hat{\omega}$, which increases by an increasing $k$, parts the $\hat{\omega}$-component of the input signal, leading to the elimination of the dc offset.

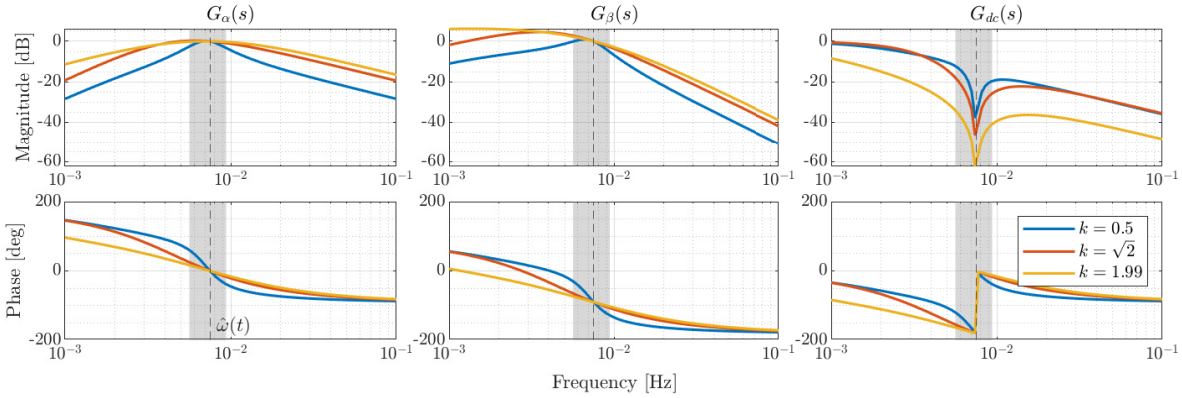


**Figure 2-9:** Bode plots of **Left:** $G_\alpha(s)$, **Centre:** $G_\beta(s)$ and **Right:** $G_{dc}(s)$ of the ESOGI structure for various damping factors $k$ and centre frequency $\hat{\omega}$ where the meandering frequency range is specified with the grey region for $St = [0.15\ 0.25]$ and $U_{hub} = 9$ m/s.

Another method, which, unlike the ESOGI structure, does not use additional parameters for the dc offset removal, is a compromise between the general SOGI and TOGI structures. The Mixed Second- and Third-Order Generalized Integrator (MSTOGI) [52] eliminates the dc offset of the input signal by adding an extra TOGI branch, which is then subtracted from the $v_\beta$-signal. The MSTOGI's transfer function, where the full derivation can be seen in Appendix A-1-2, have the following form:

$$G_\alpha(s) = \frac{k\hat{\omega}s}{\Delta_2(s)}, \qquad G_\beta(s) = \frac{k\hat{\omega}s(\hat{\omega} - s)}{(s + \hat{\omega})\Delta_2(s)}, \qquad G_{dc}(s) = \frac{k_{dc}\hat{\omega}(s^2 + \hat{\omega}^2)}{(s + \hat{\omega})\Delta_2(s)} \tag{2-15}$$

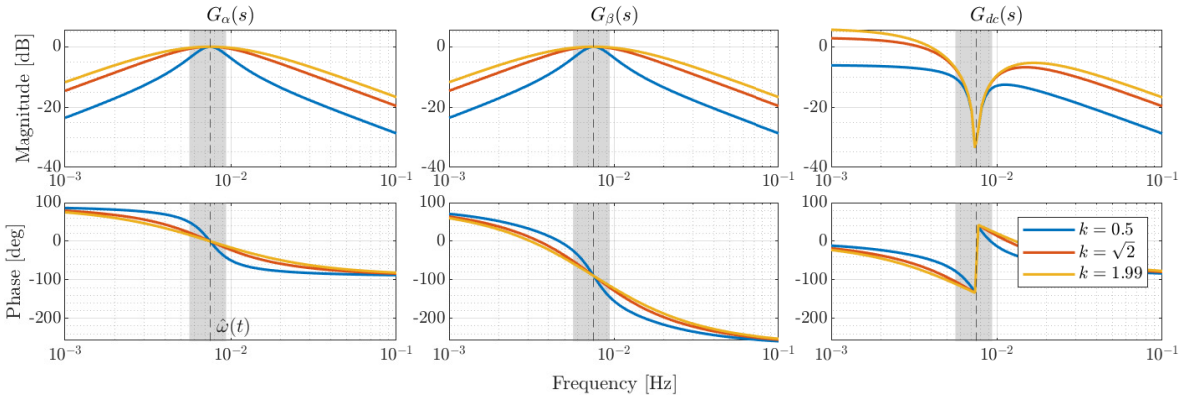


**Figure 2-10:** Bode plots of **Left:** $G_\alpha(s)$, **Centre:** $G_\beta(s)$ and **Right:** $G_{dc}(s)$ of the MSTOGI structure for various damping factors $k$ and centre frequency $\hat{\omega}$ where the meandering frequency range is specified with the grey region for $St = [0.15\ 0.25]$ and $U_{hub} = 9$ m/s.

where $\Delta_2(s) = s^2 + k\hat{\omega} + \hat{\omega}^2$. In Figure 2-10, it can be seen that $G_{dc}(s)$ is a NF with the band stop centred at $\hat{\omega}$ with a gain equal to zero, similar to the ESOGI structure. Furthermore, $G_\beta(s)$ is a BPF with unity gain and 90° phase shift at resonant frequency $\hat{\omega}$. Due to the large attenuation in both low- and high-frequency bands, the dc offset and high-frequency harmonics existing in the input signal can be effectively eliminated. This can be shown by analysing the steady-state outputs:

$$v_{\alpha\infty}(t) = a^* A \sin(\omega t + \varphi + \varphi^*) \tag{2-16a}$$

$$v'_{\beta\infty}(t) = kb - a^* \frac{\hat{\omega}}{\omega} A \cos(\omega t + \varphi + \varphi^*) \tag{2-16b}$$

$$v_{dc\infty}(t) = kb - k\hat{\omega} A \sqrt{\frac{1 - a^{*2}}{\hat{\omega}^2 + \omega^2}} \cos(\omega t + \varphi + \varphi^* - \varphi_c) \tag{2-16c}$$

where $\varphi_c = \arctan(\omega/\hat{\omega})$. By subtracting (2-16c) from (2-16b), the dc offset is removed from the output signal $v_\beta$, which results in quasi-locked state to:

$$\begin{aligned} v_{\beta\infty}(t) &= v'_{\beta\infty}(t) - v_{dc\infty}(t) \\ &= -A \cos(\omega t + \varphi) \end{aligned} \tag{2-17}$$

Hence, the $\alpha\beta 0$-frame signals of the MSTOGI-structure in the quasi-locked state become:

$$v_{\alpha\infty}(t) = A \sin(\omega t + \varphi) \qquad v_{\beta\infty}(t) = -A \cos(\omega t + \varphi) \tag{2-18}$$

This concludes the filtering stage of our single-phase PLL-system, transitioning to the last stage of Phase Detection part. This involves transforming the output signals of the modified SOGI-structures from the $\alpha\beta 0$-frame to the $dq0$-frame (refer to section 2-1), as illustrated in Figure 2-5, using a $T_{dq}$-transform:

$$\begin{bmatrix} v_d(t) \\ v_q(t) \end{bmatrix} = \begin{bmatrix} \cos\left(\hat{\theta}(t)\right) & \sin\left(\hat{\theta}(t)\right) \\ -\sin\left(\hat{\theta}(t)\right) & \cos\left(\hat{\theta}(t)\right) \end{bmatrix} \begin{bmatrix} v_\alpha(t) \\ v_\beta(t) \end{bmatrix} = T_{dq}\left(\hat{\theta}(t)\right) \begin{bmatrix} v_\alpha(t) \\ v_\beta(t) \end{bmatrix} \tag{2-19}$$

where $\hat{\theta}$ is the estimated phase given by the sum of the system's phase and phase difference $\hat{\theta}(t) = \theta(t) + \Delta\theta(t)$. Now, using trigonometric identities (refer to Appendix A-3), the $dq0$-frame

signals of (2-19) can be simplified to:

$$v_d(t) = A\cos\Big(\theta(t) - \hat{\theta}(t)\Big) \qquad v_q(t) = A\sin\Big(\theta(t) - \hat{\theta}(t)\Big) \tag{2-20}$$

where the phase $\theta(t) = \omega(t)t + \varphi$ combines the input's time-varying frequency $\omega(t)$ and phase delay $\varphi$, $v_d(t)$ represents the voltage magnitude signal and $v_q(t)$ denotes the phase error signal. Considering the time-varying nature of meandering, the influence of frequency jumps also needs to be considered. The standard SRF-PLL exhibit infinite equilibrium points, including stable points at $(2k\pi, 0)$ and saddle points at $(2k\pi + \pi, 0)$ for $k \in \mathbb{Z}$ [53]. This implies the potential for instability. Moreover, significant frequency jumps can cause the convergence of an initially stable equilibrium point to another stable equilibrium point far away, resulting in numerous oscillations, leading to a prolonged transient process. To address this, our system needs modification to ensure convergence to a stable equilibrium.

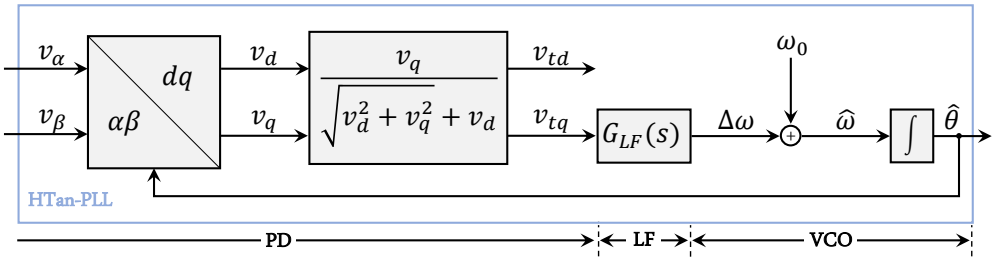


**Figure 2-11:** Block structure of the HTan-PLL module.

The Half-Tangent (HTan)-PLL [54] structure, as illustrated in Figure 2-11, addresses the challenges associated with conventional SRF-PLL structures, aiming to enhance convergence performance and dynamic response. The HTan-PLL transforms the phase error signal $v_q$ through the use of the voltage amplitude $\|v_{dq}\|$ and trigonometric identities:

$$v_{tq}(t) = \frac{v_q(t)}{\|v_{dq}\| + v_d(t)} = \frac{\frac{v_q(t)}{\|v_{dq}\|}}{1 + \frac{v_d(t)}{\|v_{dq}\|}} = \frac{\sin\Big(\theta(t) - \hat{\theta}(t)\Big)}{1 + \cos\Big(\theta(t) - \hat{\theta}(t)\Big)} = \tan\left(\frac{\theta(t) - \hat{\theta}(t)}{2}\right) \tag{2-21}$$

Normalising the $v_q$ signal ensures that a constant bandwidth and damping ratio will be maintained. Now, if the estimation errors of the phase and frequency are defined by

$$\Delta\theta(t) := \tilde{\theta}(t) = \theta(t) - \hat{\theta}(t) \qquad \Delta\omega(t) := \tilde{\omega}(t) = \omega(t) - \hat{\omega}(t) \tag{2-22}$$

The HTan's voltage magnitude and phase error signal can be denoted by

$$v_{td}(t) = A\cos\Big(\tilde{\theta}(t)\Big) \qquad v_{tq}(t) = A\tan\Big(\tilde{\theta}(t)/2\Big) \tag{2-23}$$

According to the large-signal model (2-34) with the HTan module, the equilibrium points satisfy $\dot{\tilde{\theta}} = \dot{\tilde{\omega}} = 0$, resulting in an unique equilibrium point at $(\tilde{\theta}, \tilde{\omega}) = (2k\pi, 0)$ within the region

$$\Omega_{2k} = \Big\{(\tilde{\theta}, \tilde{\omega}) \mid (2k-1)\pi \leq \tilde{\theta} \leq (2k+1)\pi, -\infty \leq \tilde{\omega} \leq \infty\Big\} \qquad \text{for } k \in \mathbb{Z}$$

As a result, any initial states within this region cause the HTan-PLL to persist within this domain and converge to the stable equilibrium point $(2k\pi, 0) \in \Omega_{2k}$. Hence, the stability in our PLL is guaranteed under frequency and phase errors. The convergence performance can be further proven using the large-signal model (2-34) following the strict Lyapunov-based proof similar to Li et al. [54]. This concludes the Phase Detection part of our PLL, which produces an output proportional to the phase error between the estimated phase and its actual value. In the next subsection, the Loop Filter, which utilises the PD's output, will be discussed.

### 2-3-2 Loop Filter

The Loop Filter (LF) attenuates the high-frequency components present in the Phase Detection output. This involves applying specific control actions to steer the phase difference $\Delta\theta$ towards zero. Let's assume that the system is close to the quasi-locked state such that the frequency and phase errors of (2-23) are sufficiently small. This allows us to express the errors as linear perturbations around an operating point:

$$v_{td}(t) \approx A \qquad\qquad v_{tq}(t) \approx A\tilde{\theta}(t) \tag{2-24}$$

Therefore, the open-loop transfer function can be obtained using a conventional type-2 PI-controller as Loop Filter control action $G_{LF}(s)$:

$$G_{ol}^{\theta}(s) = \underbrace{\frac{A}{1+\tau s}}_{PD} \cdot \underbrace{C_{LF}(s)}_{LF} \cdot \underbrace{\frac{1}{s}}_{VCO} = \frac{A\left(k_p s + k_i\right)}{s^2\left(1+\tau s\right)} \tag{2-25}$$

where $\tau = 2/(k\hat{\omega})$ is the time-constant of PD and $\omega_0$ the fundamental frequency [55]. Then, the closed-loop transfer function of the phase error is described by

$$G_{cl}^{\theta}(s) = \frac{\hat{\theta}(s)}{\theta(s)} = \frac{1}{1+G_{ol}^{\theta}(s)} = \frac{s^2\left(1+\tau s\right)}{s^2\left(1+\tau s\right) + A\left(k_p s + k_i\right)} \tag{2-26}$$

Given the time-varying nature of the meandering wake's frequency, the input signal should be modelled under a frequency ramp $\theta(s) = \Delta\dot{\omega}/s^3$ for some arbitrary acceleration rate $\Delta\dot{\omega}$ rad/s$^2$. In this scenario, the finite steady-state phase error $\tilde{\theta}_{ss}$ can be determined from (2-26) using the Final Value Theorem (FVT):

$$\tilde{\theta}_{ss} = \lim_{t\to\infty} \tilde{\theta}(t) = \lim_{s\to 0} s\, G_{cl}^{\theta}(s)\, \theta(s) = \lim_{s\to 0} \frac{\Delta\dot{\omega}\left(1+\tau s\right)}{s^2\left(1+\tau s\right) + A\left(k_p s + k_i\right)} = \frac{\Delta\dot{\omega}}{A k_i} \tag{2-27}$$

The steady-state phase error in (2-27) converges to a constant value, highlighting the preference for higher-order PLLs due to their capability to track frequency ramps with zero phase error. A type-3 PLL's LF is represented by:

$$G_{LF}(s) = k_p + \frac{k_i}{s} + \frac{k_a}{s^2} \tag{2-28}$$

In this context, the steady-state phase error becomes:

$$\tilde{\theta}_{ss} = \lim_{s\to 0} \frac{s\, a\left(1+\tau s\right)}{s^3\left(1+\tau s\right) + A\left(k_p s^2 + k_i s + k_a\right)} = 0 \tag{2-29}$$

which indeed converge to zero. However, transitioning from a type-2 PLL to a higher-order may lead to slower dynamic performance and increased system complexity. Furthermore, applying the Routh-Hurwitz stability criterion to the poles of the type-3 $G^{\theta}_{cl}(s)$ reveals that

$$A, k_p, k_i, k_a > 0, \qquad \text{and} \qquad A > \frac{k_a}{k_p k_i}.$$

must hold for stability. This implies the potential for instability during a significant reduction in bending loads where the magnitude falls below $k_a/(k_p k_i)$ [56]. To achieve the performance characteristics of a type-3 PLL, specifically zero steady-state error in phase during input signal frequency ramps, while retaining the advantages of a type-2 control system, enhancements to the type-2 PLL should be made.

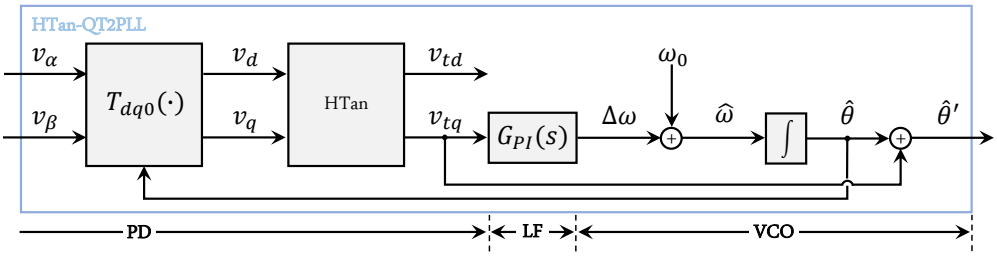


**Figure 2-12:** Block structure of the HTan-QT2PLL module.

Golestan et al. [57] proposed a feedforward branch into the conventional type-2 structure to steer the steady-state error to zero, as illustrated in Figure 2-12. The open-loop transfer of the HTan-QT2PLL system can be obtained using its small-signal model of the proposed displayed in Figure 2-13. This leads to the open-loop transfer function:

$$G^{\theta}_{ol}(s) = \frac{A}{1+\tau s}\frac{s^2 + k_p s + k_i}{s^2} \approx \frac{\overbrace{(1/\tau)}^{k_p'} s^2 + \overbrace{(k_p/\tau)}^{k_i'} s + \overbrace{(k_i/\tau)}^{k_a'}}{s^3} \tag{2-30}$$

Hence, the system effectively operates as a type-3 PLL, capable of tracking a frequency ramp. This characteristic renders the HTan-QT2PLL well-suited for tracking the slowly varying frequency of the wake. The large-signal model of the system can be derived by considering the LF and VCO stages, as illustrated in Figure 2-12. This model allows the determination of the estimated frequency and phase, given by

$$\hat{\theta}'(t) = \int \hat{\omega}(t)dt + v_{tq}(t) \qquad \hat{\omega}(t) = k_p v_{tq}(t) + k_i \int v_{tq}(t)dt + \omega_0 \tag{2-31}$$

where $\omega_0$ denotes the feed-forward parameter, a constant dependent on the frequency range for faster convergence to the quasi-locked state. Additionally, (2-31) implies:

$$\dot{\hat{\theta}}'(t) = \hat{\omega}(t) + \dot{v}_{tq}(t) \qquad \dot{\hat{\omega}}(t) = k_p \dot{v}_{tq}(t) + k_i v_{tq}(t) \tag{2-32}$$

By substituting (2-22) into (2-32), it can be deduced that:

$$\dot{\tilde{\theta}}'(t) = \tilde{\omega}(t) + \dot{v}_{tq}(t) \qquad \dot{\tilde{\omega}}(t) = k_p \dot{v}_{tq}(t) + k_i v_{tq}(t) \tag{2-33}$$

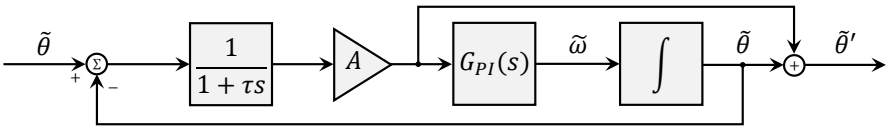


**Figure 2-13:** Small-signal model of the Modified SOGI-HTan-QT2PLL module.

The large-signal model of the HTan-QT2PLL is obtained by submitting (2-21) into (2-33):

$$\begin{aligned} \dot{\tilde{\theta}}'(t) &= \tilde{\omega}(t) - \frac{\tilde{\omega}(t)}{2\cos^2\left(\tilde{\theta}'(t)/2\right)} & \dot{\tilde{\omega}}(t) &= k_p \frac{\tilde{\omega}(t)}{2\cos^2\left(\tilde{\theta}'(t)/2\right)} - k_i \tan\left(\tilde{\theta}'(t)/2\right) \\ &= f_1(\tilde{\theta}', \tilde{\omega}) & &= f_2(\tilde{\theta}', \tilde{\omega}) \end{aligned} \tag{2-34}$$

Subsequently, the stability of the system can be evaluated by linearizing (2-34) around the equilibrium point $(\tilde{\theta}', \tilde{\omega}) = (2k\pi, 0)$ for $k \in \mathbb{Z}$:

$$\begin{bmatrix} \dot{\tilde{\theta}}' \\ \dot{\tilde{\omega}} \end{bmatrix} = \begin{bmatrix} \frac{\partial f_1(2\pi k, 0)}{\partial \tilde{\theta}'} & \frac{\partial f_1(2\pi k, 0)}{\partial \tilde{\omega}} \\ \frac{\partial f_2(2\pi k, 0)}{\partial \tilde{\theta}'} & \frac{\partial f_2(2\pi k, 0)}{\partial \tilde{\omega}} \end{bmatrix} \begin{bmatrix} \tilde{\theta}' \\ \tilde{\omega} \end{bmatrix} = \underbrace{\begin{bmatrix} \frac{1}{2} & 1 \\ -\frac{k_i}{2} & -\frac{k_p}{2} \end{bmatrix}}_{=A} \begin{bmatrix} \tilde{\theta}' \\ \tilde{\omega} \end{bmatrix} \tag{2-35}$$

Leveraging that both gains are positive ($k_p, k_i > 0$), it is consequently proven that the system is stable for $k_p > 2k_i$. The gains of the LF can be obtained using the general design optimum method [58]. The expressions for the proportional gain $k_p$ and integral gain $k_i$ are given by:

$$k_p = 2\xi\omega_n \qquad k_i = \omega_n^2 \tag{2-36}$$

where typically the damping ratio is set as $\xi = 1/\sqrt{2}$ to balance settling time and overshoot, and the natural frequency $\omega_n$ will be set $\omega_n < \omega_0$ to lower the system bandwidth. This concludes the last step of the Loop Filter, initiating the final stage of the PLL.

### 2-3-3 Voltage-Controlled Oscillator

The Voltage-Controlled Oscillator (VCO) aims to achieve precise synchronisation between the input signal and the control effort $u^c(t)$, which will be discussed in Section 2-4. This synchronisation is crucial for effectively aligning the control effort with the phase of the incoming wake to either amplify for enhanced wake mixing or attenuate to reduce loads. The estimated frequency $\hat{\omega}(t)$ is determined in the VCO by adding the feedforward-frequency $\omega_0$ to the output $\hat{\omega}$ of the Loop Filter stage, which speeds up the convergence to the quasi-locked state, as previously mentioned. Subsequently, the estimated frequency is integrated and fed back to the $T_{dq}$-transform, representing our PLL's second adaptive feedback loop. The estimated phase $\hat{\theta}'$ is then obtained by adding the additional branch of the QT2PLL-module to the integrated estimated frequency. Henceforth, $\hat{\theta}'$ is used as the phase of the synchronisation control effort. This completes the description of our developed (ESOGI or MSTOGI)-HTan-QT2PLL structure, as illustrated in Figure 2-14, serving as the phase estimator in our control configuration. In the following section, the control configuration will be expanded by constructing the control effort $u_k^c(t)$. This control effort will make use of the estimated phase $\hat{\theta}'$, the signal's magnitude $\|v_\perp\|_2$, and the estimated bias $v_{dc}$ to close the phase synchronisation loop.

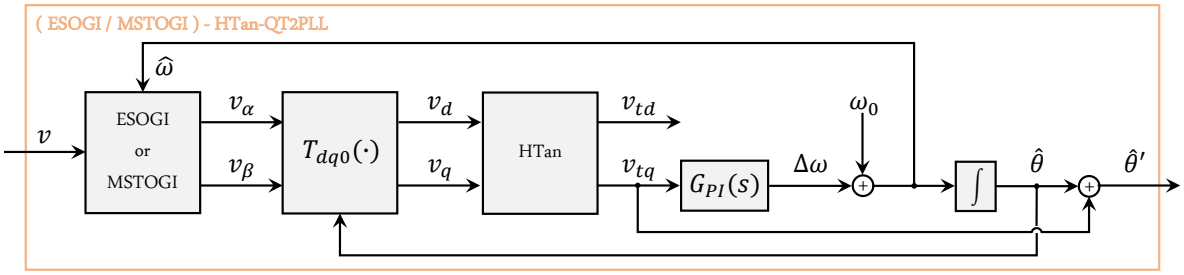


**Figure 2-14:** Block diagram of (ESOGI or MSTOGI)-HTan-QT2PLL structure with two adaptable feedback loops including $\hat{\omega}(t)$ and $\hat{\theta}(t)$ which makes this phase synchronisation control method frequency adaptive.

## 2-4 Closed-Loop Meandering Synchronisation

This section outlines the framework for the closed-loop configuration of our meandering control method. Unlike the helix method [37], where the tilt and yaw moments exhibit a closely intertwined relationship with a constant frequency and consistent 90° delay, our scenario involving the meandering effect requires treating these moments differently due to their meandering nature. Although the meandering tilt and yaw moments also share a similar phase $\theta_e(t) = 2\pi f_e(t)t + \varphi$ with a 90° delay, they possess distinct magnitudes $A_i$ and offsets $b_i$ as shown in Section 2-2. Therefore, successfully applying the phase synchronisation control strategy necessitates separately estimating the signals' magnitudes and offsets, while the phase could potentially be estimated for one axis if the rotation of the wake is known.

The constructed Phase-Locked Loop (PLL), detailed in Section 2-3, provides information about the phase, amplitude and offset of the input signal, facilitating the construction of a controller to steer the system towards a specific reference signal. The goal is to amplify or attenuate the effect of the meandering wake. Therefore, the cyclic modes $M_{dq}(t)$ will be used for reference tracking. The chosen controller for this task is simple Proportional-Integral (PI)-control, as it has proven to be sufficient in the closed-loop helix control [59], which has a similar application to our closed-loop meandering control strategy. The PI-controller will be discussed in the subsequent subsection.

### 2-4-1 Proportional-Integral control

The Proportional-Integral (PI) action is effective when employed on dc signals, given that the Integral action can solely eliminate constant or slowly varying error signals. In the context of our system, PI control is selected to track the magnitude of $M_{dq}$ and its offset, considering their characteristic of being slowly varying. The control diagram is depicted in Figure 2-15. First, two filtered quadrature signals $\bar{M}_{i\perp}$ are produced in the enhanced SOGI module for both $M_{\text{tilt}}$ and $M_{\text{yaw}}$, and their respective biases are estimated. The construction of the quadrature sets makes us able to determine the magnitude of the tilt and yaw moments using:

$$\|\bar{M}_{i\perp}\|_2 = \sqrt{M_{i\alpha}^2 + M_{i\beta}^2} \qquad \text{for } i = \text{tilt, yaw} \tag{2-37}$$

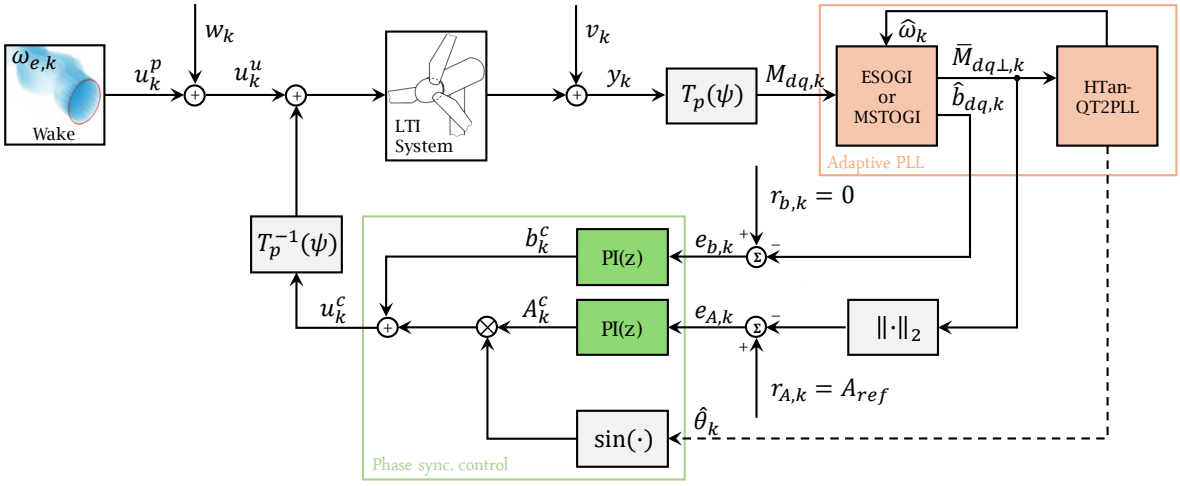


**Figure 2-15:** Proposed controller diagram for phase synchronisation in a downstream turbine using an adaptive PLL and PI controller. The wake is depicted as a periodic disturbance $u_k^u$, comprising $u_k^p$ and a load disturbance $w_k$. The output $y_k$, inclusive of measurement noise $v_k$, is transformed by a $T_{dq}$ transform and directed to the PLL. Within the enhanced SOGI modules, two filtered quadrature sets of $M_{dq}$ are generated and their biases are estimated. Then, set $\bar{M}_{\text{tilt}\perp}$ is fed to HTan-QT2PLL to estimate the frequency and phase. Combining magnitude $\bar{M}_{i\perp}$ with the reference magnitude and the biases with zero, the PI-action is employed. Multiplying this with $\sin\hat{\theta}$, results in phase synchronisation control input $u_k^c$.

Then, combining the magnitude to a reference, and the bias to zero, yields two error signals for the tilt and yaw axis on which PI-action can be applied:

$$\epsilon_{i,A}(t) = M_{i,\text{ref}}(t) - \|\bar{M}_{i\perp}(t)\|_2 \qquad \text{and} \qquad \epsilon_{i,b}(t) = 0 - b_i(t) \tag{2-38}$$

The PI controller is designed using $k_p$, representing the proportionality to the error, and $k_i$, reflecting the proportionality to the integrated error. The transfer function of the PI controller is expressed as:

$$G_{PI}(s) = k_p + \frac{k_i}{s} = k_p \cdot \frac{s + k_i/k_p}{s} \tag{2-39}$$

The inclusion of the Integral action $k_i$ introduces an additional pole at the origin, ensuring the integration of both positive and negative errors. This continuous adjustment aids in eliminating steady-state errors. To enhance the controller's responsiveness, Proportional gain $k_p$ is introduced. From Eq. (2-39), it becomes clear that this adds a zero to the system located at $-k_i/k_p$. The Bode plots in Figure 2-16 demonstrate the impact of tuning of $k_p$ to increase the controller's speed by shifting the magnitude response vertically. After optimising $k_p$, $k_i$ is adjusted to set the cutoff frequency in the open-loop transfer function. The resultant magnitude control effort $A^c$ is multiplied by a sine function incorporating the phase estimated in the HTan-QT2PLL module. This is then added to the bias control effort $b^c$, resulting in the phase synchronisation control effort $u^c(t)$, as illustrated in Figure 2-17, mathematically represented by:

$$u^c_{\text{tilt}}(t) = A^c_{\text{tilt}} \sin\left(\hat{\theta}(t)\right) + b^c_{\text{tilt}} \qquad u^c_{\text{yaw}}(t) = A^c_{\text{yaw}} \cos\left(\hat{\theta}(t)\right) + b^c_{\text{yaw}} \tag{2-40}$$

Note that this control effort is for synchronising a CW rotating wake. In the case of a CCW rotation, it results in a negative cosine signal in $u^c_{\text{yaw}}(t)$. Consequently, with the control effort

described in (2-40), our control method has transitioned into a closed-loop system. This enables it to guide the tilt and yaw moments towards a specified reference, facilitating the amplification or attenuation of the meandering wake.

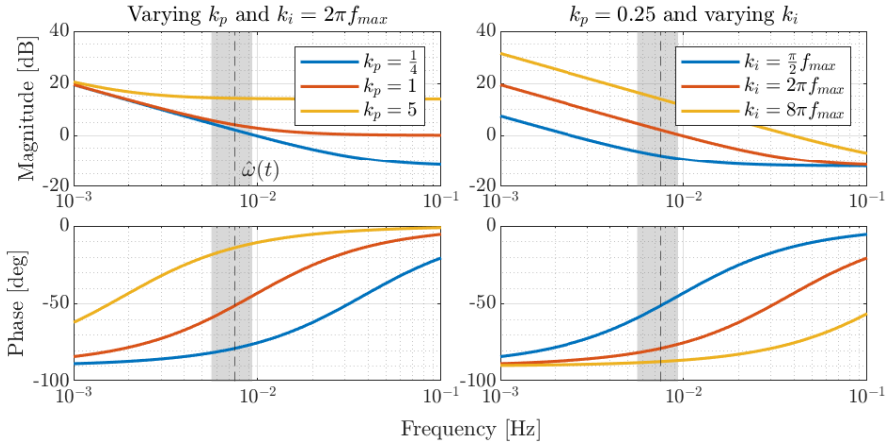


**Figure 2-16:** Bode plots of a PI controller with **Left:** varying values of $k_p$ with a constant value for $k_i$, and **Right:** constant $k_i$ and varying $k_p$. The meandering frequency range is specified with the grey region.

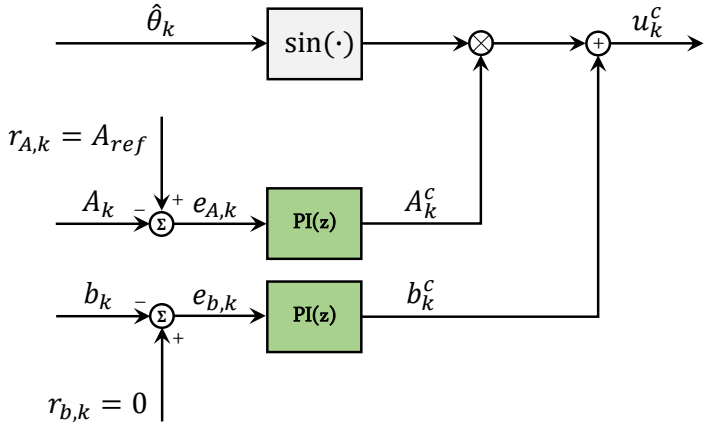


**Figure 2-17:** Blockscheme of construction phase control effort $u^c(t) = A^c \sin(\hat{\theta}(t)) + b^c$.

## 2-5 Concluding Remarks on the Controller Strategy

This chapter has provided the preliminary knowledge for meandering wake synchronisation. It has provided an overview of different reference frames and their transformations, including the MBC transform, which initiates the conversion of the coupled MIMO system into two SISO systems. Then, the interaction of the meandering wake at the downstream turbine was discussed, presenting a mathematical representation of the interference between the wake and control effort. This deepened our understanding of amplifying or attenuating the meandering wake's effect during Clockwise and Counterclockwise rotations. Subsequently,

the (ESOGI or MSTOGI)-HTan-QT2PLL structure was derived, enabling the estimation of the time-varying frequency and phase of an incoming signal. A comprehensive assessment was conducted, considering its behaviour in mitigating the impact of an offset in the wake's centerline, and addressing frequency- and phase jumps caused by the meandering wake. A closed-loop control strategy was also derived, which utilises the magnitude of the tilt and yaw moments, along with their biases, which were obtained in the enhanced SOGI modules, crucial for the amplification or attenuation of the meandering effect. The next chapter will evaluate the performance of the ESOGI and MSTOGI modules for both in-phase and out-of-phase synchronisation during reference tracking and disturbance rejection on a Low-Order model to reveal the limits of our control setup.

# Chapter 3

# Phase synchronisation in Low-Order Mass-Spring-Damper system

This chapter will focus on the validation of the performance of the control method of Chapter 2. In the first section, a Linear Time-Invariant Three-Degrees-of-Freedom Mass-Spring-Damper system will be derived to represent a downstream turbine experiencing a time-varying meandering wake. The low-order model, with all states known, enhances our understanding of the estimation and control capabilities of the proposed control method. Subsequently, the experimental setup details will be discussed, and planned test cases will be outlined. In the following section, the results of various test cases will be evaluated. Finally, the chapter concludes with a discussion of the results to assess the performance of the control method.

## 3-1 Model Description

The Three-Degrees-of-Freedom Mass-Spring-Damper (3DOF-MSD) system, as illustrated in Figure 3-1, is a Linear Time-Invariant (LTI) model composed of masses $m_i$, springs $k_i$ and dampers $c_i$ for $i = 1, 2, 3$. The masses interconnect through springs and dampers, with the first mass connected to a fixed frame and the third being free. An external periodic force $f(t) \in \mathbb{R}^r$ will excite the first mass. A second-order differential equation can describe this system:

$$M\ddot{q}(t) + J\dot{q}(t) + Kq(t) = Sf(t) \tag{3-1}$$

where $\ddot{q}(t)$ stands for acceleration, $\dot{q}(t)$ represents velocity and $q(t) \in \mathbb{R}^n$ denotes displacements, accompanied by respectively the mass $M$, damping $J$, and stiffness $K$ matrices. The Boolean input shape matrix $S \in \mathbb{R}^{n \times r}$ specifies the state where $f(t)$ is applied. By defining the state vector as $x(t) = [\, q(t)\ \dot{q}(t)\,]^\top$ and the input as $u(t) = f(t)$, the state-space model can be described as follows:

$$\dot{x}(t) = \underbrace{\begin{bmatrix} 0_{n\times n} & I_{n\times n} \\ -M^{-1}K & -M^{-1}J \end{bmatrix}}_{A} x(t) + \underbrace{\begin{bmatrix} 0_{n\times r} \\ M^{-1}S \end{bmatrix}}_{B} u(t) + w(t) \tag{3-2}$$

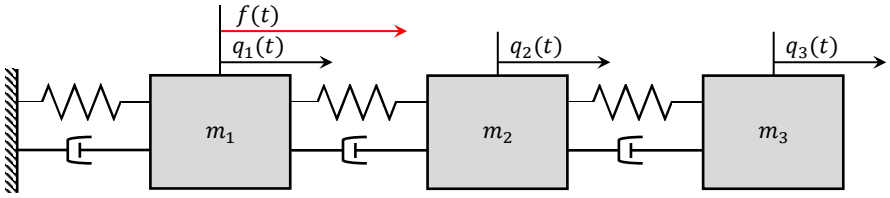


**Figure 3-1:** Schematic of the simulated Three-Degrees-of-Freedom Mass-Spring-Damper system.

where the mass, spring and damping matrices are given by

$$M = \begin{bmatrix} m_1 & 0 & 0 \\ 0 & m_2 & 0 \\ 0 & 0 & m_3 \end{bmatrix}, \quad J = \begin{bmatrix} c_1 + c_2 & -c_2 & 0 \\ -c_2 & c_2 + c_3 & -c_3 \\ 0 & -c_2 & c_3 \end{bmatrix}, \quad K = \begin{bmatrix} k_1 + k_2 & -k_2 & 0 \\ -k_2 & k_2 + k_3 & -k_3 \\ 0 & -k_2 & k_3 \end{bmatrix} \tag{3-3}$$

with mass values $m_1 = 14$ kg, $m_2 = 16$ kg and $m_3 = 15$ kg, damping coefficients $c_1 = c_2 = c_3 = 0.6$ Ns/m, and spring stiffness $k_1 = k_2 = 0.1$ N/m and $k_3 = 0.3$ N/m. These parameters are selected following the approach of Van Vondelen et al. [37] to resemble the natural frequency of a wind turbine tower. The experiment aims to mimic the amplification or attenuation of the meandering wake acting on the downstream turbine. Consequently, the position of the first mass is selected as the system's output to evaluate the controller's synchronisation performance. The system's output is represented as:

$$y(t) = \underbrace{\begin{bmatrix} 1 & 0 & 0 & 0 & 0 & 0 \end{bmatrix}}_{C} x(t) + \underbrace{\begin{bmatrix} 0 \end{bmatrix}}_{D} u(t) + v(t) \tag{3-4}$$

This completes the derivation of the linearized state-space model for the Three-Degrees-of-Freedom Mass-Spring-Damper system, which will be utilised to assess the effectiveness of our developed control method. Subsequently, the next subsection will delve into the details of the experimental setup for the low-order experiment.

### 3-1-1 Experimental Setup

The experimental setup, illustrated in Figure 3-2, assumes that the input on the Linear Time-Invariant 3DOF-MSD system includes an uncontrollable input $u^u$ and control input $u^c$. The uncontrollable input $u^u$ includes the periodic disturbance $u^p$ with process noise $w$. The periodic disturbance represents the external force $f(t)$ acting on the first mass and is modelled by

$$u^p(t) := f(t) = b + A \sin\left(\omega(t)t + \varphi\right) \tag{3-5}$$

where $b$, $A$, $\varphi$ and $\omega(t)$ are the bias, the amplitude, the initial phase and the time-varying frequency of the periodic disturbance. In the different test cases, $u^u$ will be set within the meandering frequency range specified by $St = [\,0.15\ 0.25\,]$ for a wind speed at hub height of $U_{hub} = 7$ m/s. The process noise is assumed to be Gaussian White Noise with an amplitude of 4% of the amplitude of the periodic disturbance. The controllable input $u^c$ is a sinusoidal signal consisting of the estimated phase $\hat{\theta}$ and amplitude $A^c$ plus the bias $b^c$. Subsequently, input $u$ is fed to the Mass-Spring-Damper system as illustrated in the experimental setup of

Figure 3-2. The resulting output $y$ is directed to the enhanced SOGI modules and passed through to HTan-QT2PLL, estimating the system's frequency and phase. The estimated frequency is fed back to the SOGI structures to set their centre frequency. The Input Generator will construct the control action $u^c$ using the estimated estimated phase and characteristics of the output. Additionally, a switch is implemented in the experimental setup to specify the ESOGI or MSTOGI module used in the adaptive PLL. The experiment will be performed in discrete time. Hence, Eqs. (3-2), (3-4) and (3-5) will be discretized with a sampling time of $t_s = 0.1$ seconds. The low-order experiment will consist of three main test cases conducted in MATLAB. First, the tracking ability of the system will be analysed. Then, its rejection capability against disturbances. Lastly, its performance in synchronising the phase of the incoming signal while attenuating the effect of periodic load will be evaluated. The results of these different test cases are presented in the next section.

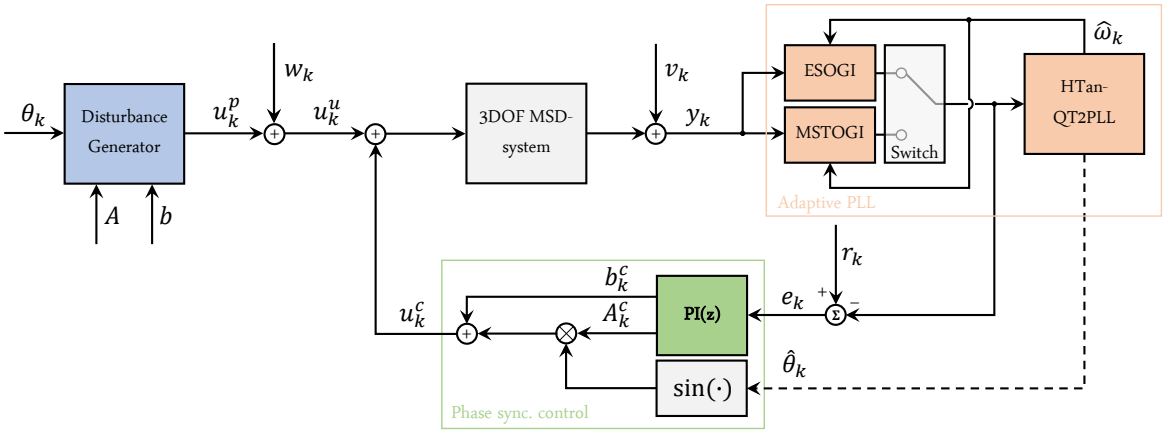


**Figure 3-2:** Control diagram of the low-order system. The input $u_k$, consisting of the periodic disturbance $u_k^u$ and controllable input $u_k^c$, is fed into the 3DOF Mass-Spring-Damper system. The output is then directed to the improved SOGI modules with centre frequency $\hat{\omega}$ and further processed through HTan-QT2PLL for frequency and phase estimation. The Input Generator constructs the control action $u_k^c$ using estimated phase $\hat{\theta}_k$, amplitude $A^c$ and bias $b^c$. A switch is implemented in the setup to specify the enhanced SOGI module used in the adaptive PLL.

## 3-2 Result of the Lower-Order Model

The simulations for specified control configurations, as mentioned in the previous subsection, are run with a duration of $t_{max} = 2000$ seconds. In Figure 3-3, $u_k^u$ undergoes a frequency step at $t = 1000$ seconds to evaluate the performance in tracking a signal with varying frequency. The control input becomes active after $t_{act} = 200$ seconds. Upon activating the control input, the deflection of the first mass significantly increases compared to the response solely to the periodic disturbance $u_k^u$. Two peaks in the frequency estimation occur, as shown in the middle plot of Figure 3-3. The first peak emerges after activating the control action, and the second occurs after the frequency step. After a transient period and overshoot, they converge to a steady frequency estimate. It is noteworthy that the peak after activation has a larger overshoot due to compensating for the delayed tracking. Consequently, the frequency significantly increases, but eventually, it converges back to a steady frequency

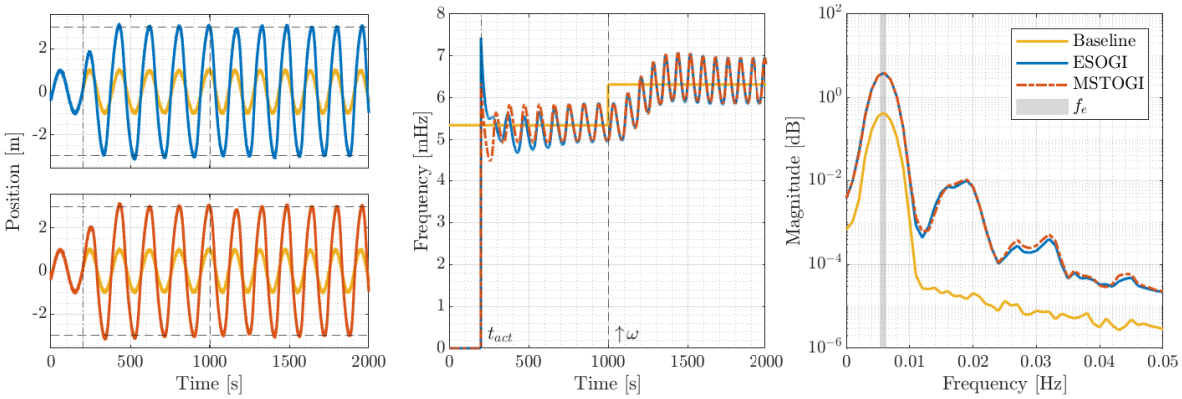


**Figure 3-3:** Results of amplification during phase synchronisation on a 3DOF-MSD system. **Left:** Time-domain response with **Top:** ESOGI-, and **Bottom:** MSTOGI- HTan-QT2PLL using PI-control for synchronising $u_k^u$ with a frequency step. **Middle:** Time-domain results of $\hat{\omega}$ for both methods with ripples caused by the inherent nature of SOGI-PLL with ripples caused by the inherent nature of SOGI-PLL. **Right:** Welch Power Spectrum results with a peak at $\hat{\omega}$ and peaks at the 3$^{rd}$ harmonic caused by the ripples.

estimate. Throughout the transient period, the MSTOGI structure converges more rapidly and displays less overshoot compared to the ESOGI structure.

The ripple observed in the plot depicting the estimated frequency, the middle plot of Figure 3-3, is caused by the harmonics inherent in the nature of SOGI-PLL, as noted by Xu et al. [50], but it does not significantly affect the tracking capability of the system. Specifically, the ripple present on the frequency component of $v_{dq}(t)$ (Eq. (2-23)) corresponds to the second harmonics, which subsequently map back to the third harmonics on $v(t)$ (Eq. (2-8)). This phenomenon is evident in the Welch Power Spectrum, depicted in the left plot of Figure 3-3, where the second peak represents the third harmonic of the estimated frequency. Additionally, the main peak of both control methods aligns with the peak induced by the periodic disturbance but with a greater magnitude. This alignment indicates that both control methods can amplify the first mass's position during a frequency jump. Consequently, both methods can be used for phase synchronisation during instantaneous frequency variations. The next subsection will delve deeper into the tracking abilities of the control methods and will evaluate their performance in rejecting disturbances.

### 3-2-1 Reference Tracking & Disturbance Rejection

During the phase synchronisation of the wake at the downstream turbine, the wake's characteristics may undergo changes. The frequency can vary gradually over time, the lateral displacement might change, and the wake centre may not perfectly align with the downstream wind turbine. Consequently, an additional analysis of the control methods' performance will be carried out, encompassing frequency ramp tracking, amplitude drop/rise rejection, and offset compensation. In Figure 3-4, both control methods effectively demonstrate the ability to track a frequency ramp, simulating the slowly varying nature of meandering wakes. The system swiftly adjusts to a persistent increasing frequency estimate after a brief transient. This aligns with the amplified system response shown by the deflection of the first mass, indicating effective amplification. The peaks in the Welch Power Spectrum, corresponding to the

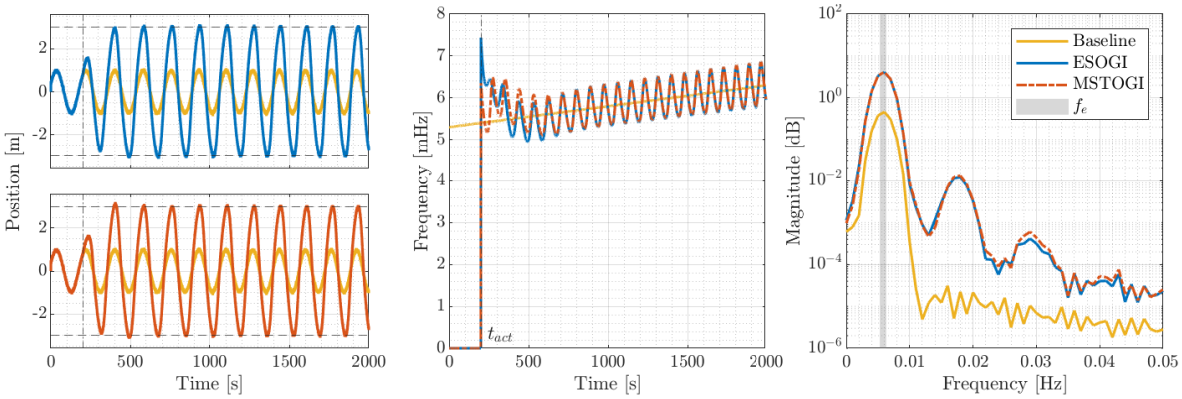


**Figure 3-4:** Results of amplification during phase synchronisation on a 3DOF-MSD system. **Left:** Time-domain response with **Top:** ESOGI-, and **Bottom:** MSTOGI- HTan-QT2PLL using PI-control on $u_k^u$ with increasing frequency. **Middle:** Time-domain results of $\hat{\omega}$ for both methods with ripples caused by the inherent nature of SOGI-PLL. **Right:** Welch Power Spectrum showing a widened main peak at the 1st and 3rd harmonic of $\hat{\omega}$ due to the increasing frequency.

fundamental and 3rd harmonic of the estimated frequency, consistently align with those induced by the periodic disturbance. Furthermore, the broader peaks indicate synchronisation across the wider frequency range. Hence, both control methods can effectively track a frequency ramp, making them applicable to the controller of the downstream turbine impinged by the slowly varying wake.

The focus now shifts to assessing the rejection of a constant lateral deflection for both control methods. An offset in the signal may lead to disturbances inside the PLL, as mentioned in Section 2-3-1, effectively impacting the PLL's accuracy. To evaluate the offset rejection capabilities of the enhanced SOGI structures, a positive bias ($b > 0$ in $u_k^p$ Eq. (3-5)) is introduced to the periodic disturbance. Both control methods effectively compensate for the offset, as depicted in Figure 3-5, restoring the response to its reference as indicated by

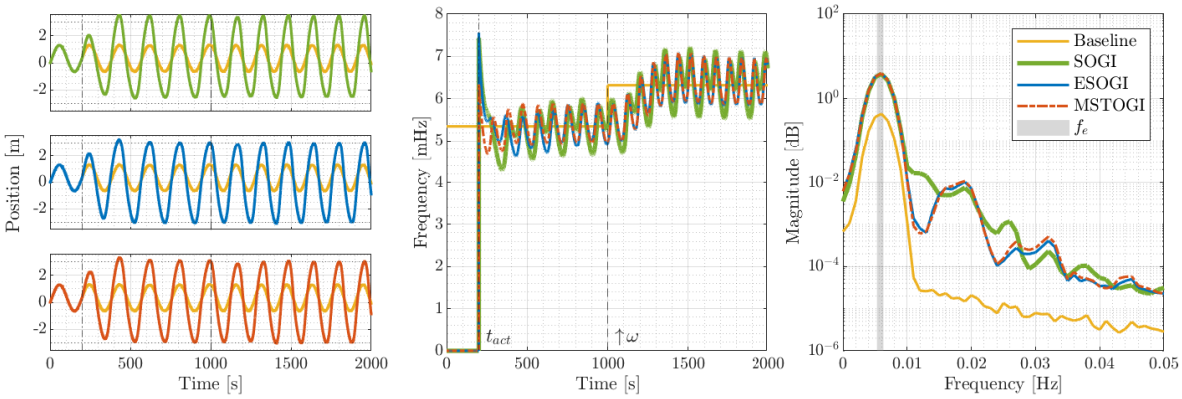


**Figure 3-5:** Results of amplification during phase synchronisation on a 3DOF-MSD system. **Left:** Time-domain response with **Top:** SOGI-, **Centre:** ESOGI-, and **Bottom:** MSTOGI-HTan-QT2PLL using PI-control on $u_k^u$ for rejecting a constant positive while tracking a frequency step. **Middle:** Time-domain results of $\hat{\omega}$ for both methods with ripples caused by the inherent nature of SOGI-PLL. **Right:** Welch Power Spectrum results with the mean peak at $\hat{\omega}$.

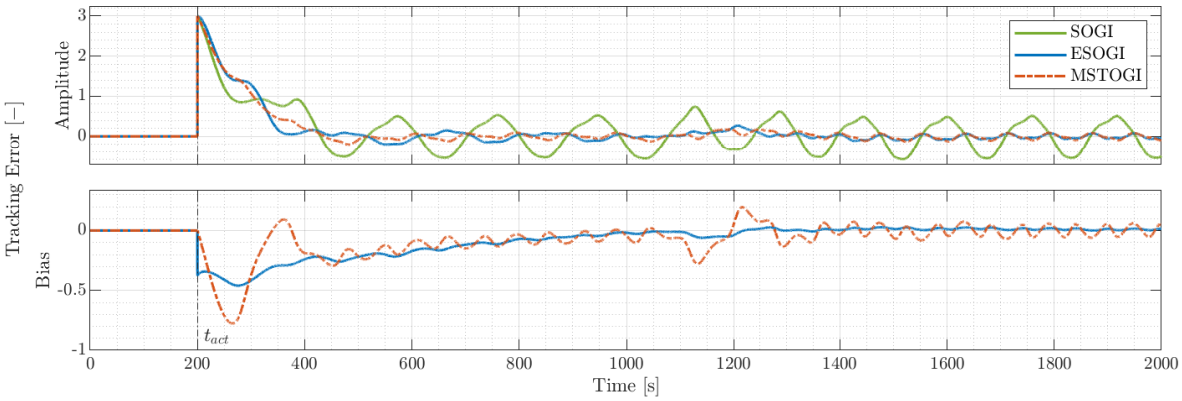


**Figure 3-6:** Results of amplification during phase synchronisation on a 3DOF-MSD system. Time-domain response of tracking errors of **Top:** amplitude, and **Bottom:** bias for the SOGI, ESOGI, and MSTOGI modules. Note that no error signal is shown for the offset tracking of the SOGI since the module cannot estimate the offset.

horizontal dashed lines. In contrast, the conventional SOGI module (green line) results in a constant offset in the response. The middle plot, illustrating frequency estimation, reveals an additional oscillation in the estimated frequency of the conventional module, suggesting an internal disturbance in the PLL. This disturbance is further highlighted in the Welch Power Spectrum, where there is a noticeable increase in power overall instead of distinct peaks at the $3^{\text{rd}}$ and $5^{\text{th}}$ harmonics. Figure 3-6, depicting the tracking errors, emphasises the accurate estimation of the amplitude and offset of the periodic disturbance. Both error signals are guided to zero, contrasting with the oscillatory behaviour observed with the standard SOGI module. It's worth noting that no offset estimate is provided for the SOGI, as it lacks this capability. Consequently, both ESOGI and MSTOGI effectively reject the offset's effect within the PLL, as evidenced by the convergence to the steady frequency estimate. This renders both control methods suitable for accommodating a changing wake. The previous test cases focused on in-phase synchronisation, which amplifies the system's response, enhancing wake mixing and resulting in higher power performance at the downstream wind turbine. The subsequent subsection will further investigate the control methods' performance under uncertain conditions involving heavily increased process noise.

### 3-2-2 Effect of the Signal-to-Noise Ratio

In the mentioned test cases, process noise was already included in $u_k^u$. However, the impact of the process noise on the accuracy of the control methods is not explored in detail. Therefore, to further evaluate the control methods' ability to estimate the fundamental frequency of the periodic disturbance under distorted conditions, the amplitude of the process noise $w_k$ will be raised to 50% of the amplitude of $u_k^p$. The result of the heavily distorted test case during a frequency step is depicted in Figure 3-7. These heavily distorted conditions lead to an increased transient time and overshoot compared to the less distorted case illustrated in Figure 3-3. The Welch Power Spectrum shows an overall increase in magnitude, while the peak at the fundamental frequency still aligns with a similar magnitude as in Figure 3-3. The performance of the control method in distorted conditions can be quantified using the Signal-to-Noise Ratio (SNR). The SNR is a measure indicating the signal's strength relative to the

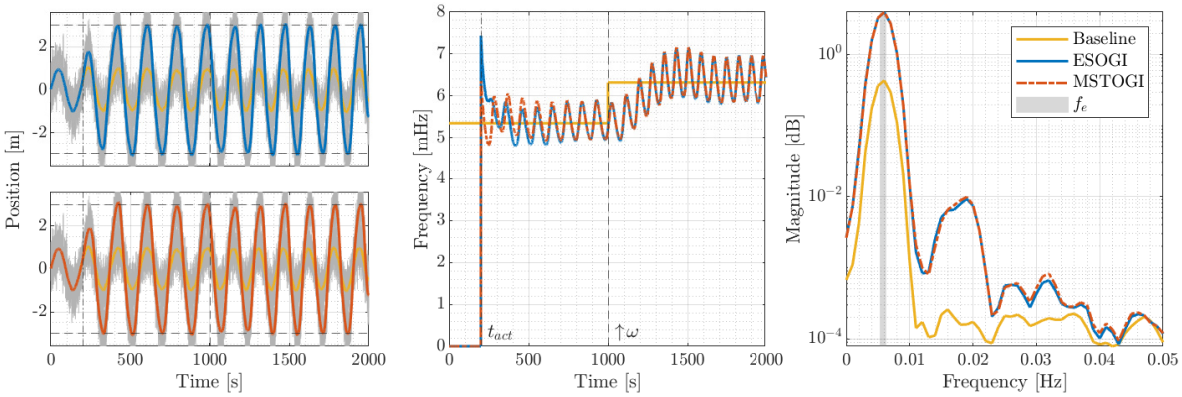


**Figure 3-7:** Results of amplification during phase synchronisation on a 3DOF-MSD system. **Left:** Time-domain response with **Top:** ESOGI-, and **Bottom:** MSTOGI- HTan-QT2PLL using PI-control on $u_k^u$ with a frequency step during heavily increased process noise. The system responses are post-filtered using a digital zero-phase LPF for better visibility. **Middle:** Time-domain results of $\hat{\omega}$ for both methods with ripples caused by the inherent nature of SOGI-PLL with ripples caused by the inherent nature of SOGI-PLL. **Right:** Welch Power Spectrum results with a peak at $\hat{\omega}$ and peaks at the 3$^{\text{rd}}$ harmonic caused by the ripples.

background noise in a system. Utilising the MATLAB function `snr` yielded a SNR of 12.10 for ESOGI and 12.07 for MSTOGI. These values highlight the effectiveness of the Loop Filter stage in successfully filtering the process noise from the periodic disturbance, resulting in an accurate phase estimate. Both control methods demonstrate the ability to synchronise the phase of the periodic disturbance and amplify its response in phase under heavily distorted conditions. They are also capable of tracking frequency step and ramp, rejecting amplitude rise/drop, and compensating for induced offsets. However, the attenuation of the system's response still needs exploration. Therefore, the subsequent subsection will delve into the analysis of attenuation during phase synchronisation performance.

### 3-2-3 Effect of Attenuation

Applying phase synchronisations using full attenuation directly diminishes the system's response to the periodic disturbance, consequently reducing the bending loads on the downstream turbine. However, achieving complete attenuation poses a challenge as a PLL can exclusively lock onto the phase of periodic signals. Furthermore, the PLL does not differentiate between the input's periodic component and the process noise. Consequently, steering the system's response to zero also amplifies the relative influence of the load disturbance on the system's response. Therefore, complete attenuation of the periodic disturbance is not achievable. Nevertheless, near-complete attenuation is demonstrated in the system response in Figure 3-8. The deflection of the first mass has been effectively reduced close to zero. However, it exhibits non-sinusoidal behaviour, as evidenced by the sawtooth pattern of ripples in the frequency estimation plot. Additionally, the Welch Power Spectrum indicates a decrease in the main peak's magnitude at the fundamental frequency for both methods. Although the main peak still aligns with the response on $u_k^u$, its magnitude is reduced, confirming the system's synchronisation with the periodic disturbance. Notably, the spectrum also reveals an increase in the peaks at the 3$^{\text{rd}}$ and 5$^{\text{th}}$ harmonics with MSTOGI, while ESOGI shows

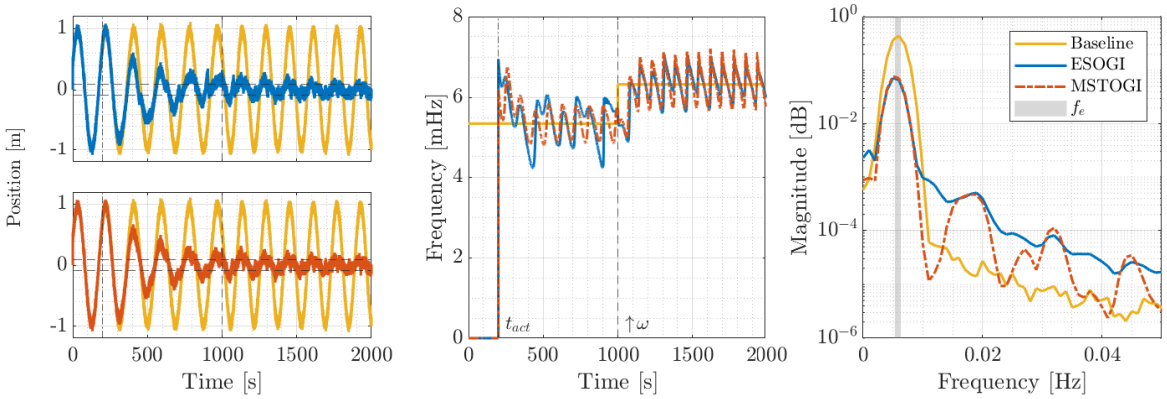


**Figure 3-8:** Results of attenuation during phase synchronisation on a 3DOF-MSD system. **Left:** Time-domain response with **Top:** ESOGI-, and **Bottom:** MSTOGI- HTan-QT2PLL using PI-control. **Middle:** Time-domain results of $\hat{\omega}$ for both methods with nonsinusoidal ripples. **Right:** Welch Power Spectrum results with a reduced main peak at $\hat{\omega}$ and increase in magnitude on other frequencies.

an overall increase in the energy contribution. This suggests that MSTOGI better preserves the periodic load's fundamental frequency while attenuating its effect. Therefore, it can be concluded that MSTOGI outperforms ESOGI.

## 3-3 Concluding Remarks of the Lower-Order Model

All test cases were intentionally conducted with enlarged characteristics to thoroughly evaluate the boundaries and robustness of the control methods. Consequently, when synchronising with the meandering wake effect, the system experiences more slowly varying changes, e.g. smaller frequency jumps and smaller amplitude drops and swells. Both control methods demonstrated successful amplification and attenuation during the test cases on the response of a time-varying periodic disturbance. The enhanced SOGI structures showed great filtering ability, emphasised by the large positive SNR in the heavily distorted test case. Furthermore, the enhancements introduced to the SOGI modules successfully reject the offset internally within the PLL while providing an accurate estimate to compensate for the offset using the control input. Successfully steering the system response back to its reference. The results presented in this chapter showed better performance of the MSTOGI than the ESOGI structure. The lower transient time, less overshoot, and better consistency of frequency estimation across all test cases evidence this. Since the natural frequency of the Mass-Spring-Damper system was chosen to be similar to that of wind turbines, the control strategy employed in this chapter can be directly applied in a simulation environment using reference wind turbines. Therefore, in the next chapter, our closed-loop phase synchronisation will be implemented on a downstream wind turbine using the MSTOGI-HTan-QT2PLL for phase and frequency estimation, along with a closed-loop control strategy including PI-control for reference tracking.

# Chapter 4

# Phase Synchronisation in Higher-Order Wind Turbine Models

The previous chapter validated our methodology under different conditions using the simulation environment of a lower-order system. Both methods demonstrated their ability to estimate the time-varying frequency and successfully amplify and attenuate with reasonable accuracy, with the MSTOGI structure exhibiting better performance than ESOGI. Consequently, the MSTOGI-HTan-QT2PLL will be implemented for phase synchronisation in a downstream turbine affected by meandering wake effects to investigate its performance in a higher-order wind turbine simulation environment. The first part of this chapter introduces this simulation environment, followed by a discussion of the simulation results in the second part. Finally, all findings will be summarised in the concluding section.

## 4-1 Experimental Setup in OpenFAST

To evaluate the performance of the control method on wind turbines, the experiment will be conducted within the simulation environment of OpenFAST [60]. OpenFAST is a versatile tool capable of simulating the coupled dynamic response of wind turbines across various configurations. It supports wind turbine configurations, including two- or three-blade horizontal-axis rotors. Furthermore, it allows for modelling wind turbines in diverse settings, including onshore and offshore installations, with fixed-bottom or floating substructures. OpenFAST integrates physical phenomena and system couplings containing environmental excitation such as wind, waves, and currents. Additionally, it models the dynamic response of the entire turbine system, including the rotor, drivetrain, nacelle, support structure, and controller. This enables the evaluation of fatigue analysis and loading assessment for both normal and extreme conditions.

The OpenFAST software can be extended in FAST.Farm [15] to address the dynamics of each individual turbine. This extension considers further physics for wind farm-wide ambient wind in the atmospheric boundary layer, wind farm control, and aspects such as wake

deficits, advection, deflection, meandering, and merging. However, FAST.Farm may encounter limitations in simulating more complex flow fields essential for analysing wake mixing performance. Hence, to specifically analyse the effect of meandering phase synchronisation involving interactions between two turbines, the downstream turbine will be simulated in OpenFAST while its inflow will replicate the outflow of the upstream turbine. Details regarding the construction of this inflow will be discussed in Section 4-1-3. But first, in the subsequent subsection, the reference wind turbine used in the experiment will be introduced.

### 4-1-1 15-Megawatt Reference Wind Turbine

The turbine model used as a reference throughout this thesis is the International Energy Agency 15-Megawatt Offshore Reference Wind Turbine [61]. The IEA 15-MW RWT represents an offshore wind turbine with a power rating of 15 megawatts, matching the scale of the largest turbines in current installations. Consequently, these turbines are particularly compelling for testing our control system. Its key parameters are listed in Table 4-1:

**Table 4-1:** Key parameters for the IEA 15-MW RWT, adapted from [61].

| Description | Value | Unit |
|---|---|---|
| Rated Power | 15 | MW |
| Rotor Orientation / Configuration | Upwind / 3 Blades | - |
| Rotor Diameter | 240 | m |
| Hub Height | 150 | m |
| Cut-In / Rated / Cut-Out Wind Speeds | 3 / 10.59 / 25 | m/s |
| Designed tip-speed-ratio | 9.0 | - |
| Minimum / Maximum Rotor Speed | 5.0 / 7.56 | rpm |
| Maximum Tip Speed | 95 | m/s |
| Max Pitch Rate | 2 | °/s |

Wake mixing strategies, like Phase Synchronisation, are typically applied at wind speeds below the rated conditions, refer to Figure 1-1, as power losses are more significant in this regime compared to above-rated conditions [36]. Hence, all simulations in this chapter are performed in Region 2 as well, operating in the wind speed range between 6.98 m/s and 10.59 m/s. In this regime, the rotor speed is controlled to maintain maximum aerodynamic efficiency and power by operating at the turbine's optimal TSR while maintaining a constant blade pitch angle. Here, the $k\omega^2$-law can be used to establish a relationship between the generator speed $\omega_g$ and the demanded torque $\tau_g$, assuming the turbine operates at its optimal TSR $\lambda_{\text{opt}}$ and corresponding power coefficient $C_{p,\max}$:

$$\tau_g(t) = k\omega_g^2(t), \qquad \text{where } k = \frac{\pi\rho R^5 C_{p,\max}}{2\lambda_{\text{opt}}^3 N_g^3 \eta_{gb}} \tag{4-1}$$

However, due to the high flexibility of modern turbine rotors, the assumption of $R$ remaining constant in $k$ is less applicable, potentially leading to modelling errors. Therefore, employing a TSR tracking controller with a PI controller to regulate the generator torque is preferred, as modern rotors are usually designed to optimise aerodynamic efficiency at specific TSR

values [61]. Hence, a TSR tracking controller is integrated into Reference Open-Source COntroller (ROSCO) [62], reflecting common practices in the field. Since this thesis aims to synchronise the meandering effect, the existing ROSCO controller serves as the baseline controller and will be further discussed in the subsequent subsection.

### 4-1-2 Control Strategy on the Downstream Turbine

The ROSCO controller from NREL will serve as the baseline controller in all experiments conducted in this chapter. ROSCO presents a modular reference wind turbine controller that aligns with industry standards. The automatic tuning of all standard controller implementations and control modules facilitates the seamless integration of our meandering phase synchronisation controller. While ROSCO manages the baseline control, including the collective blade pitch angle and generated torque, our meandering phase synchronisation controller will govern the individual pitch angles. These angles will be superimposed on ROSCO's collective pitch angle, as depicted in Figure 4-1. Our phase synchronisation controller leverages existing parameters within OpenFAST. By employing a MBC transform on the BOoP moments, the tilt and yaw moments are constructed, enabling the application of our MSTOGI-HTan-QT2PLL method to estimate the resulting phase, magnitude, and offset. Subsequently, integral action is utilised for closed-loop reference tracking, leading to the pitch angles on the tilt and yaw axis, as discussed in Section 2-4. An inverse MBC transform translates these angles into individual pitch angles, which can be applied to the IEA 15-MW reference wind turbine in OpenFAST along with the collective pitch angle constructed by the ROSCO controller.

In the inverse MBC, as detailed in Section 2-1-2, an azimuth offset $\varphi_{\text{off}}$ is included to minimise the coupling between non-rotating axes and compensate for actuator delays. However, determining $\varphi_{\text{off}}$ presents a challenge due to its dependence on wind speed and turbine operating

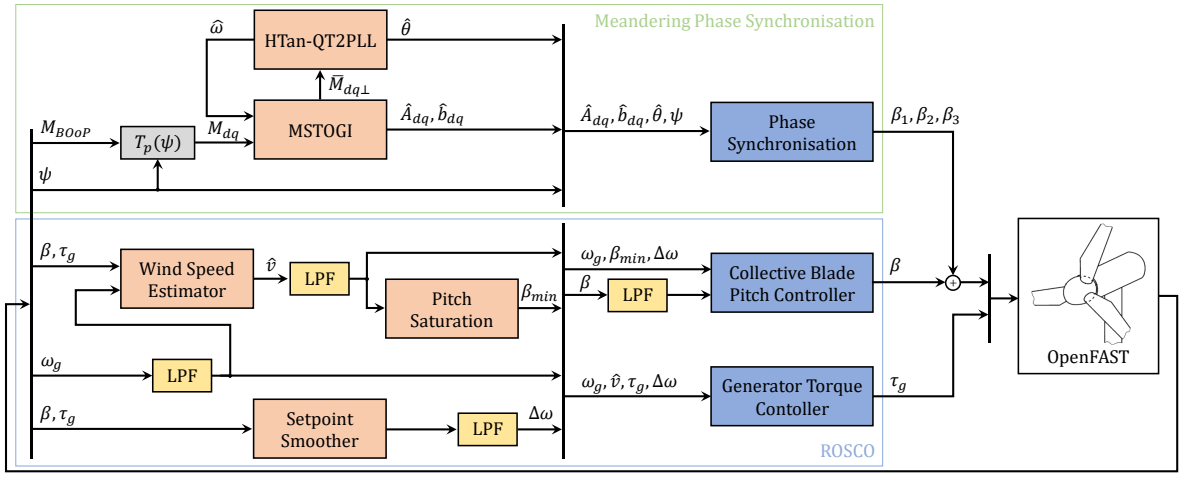


**Figure 4-1:** The block diagram illustrates the overall controller logic in Simulink featuring ROSCO and our phase synchronisation controller. The key time-varying signals exchanged between different controller components are highlighted. The blue-shaded regions represent the torque and pitch controllers, the orange boxes various control actions and the yellow squares represent filters.

conditions, which vary due to the time-varying nature of meandering. Additionally, since the control strategy relies on the magnitude of the tilt and yaw moment for reference tracking, the system exhibits nonlinearity. Therefore, the azimuth offset is determined heuristically. Similarly, a heuristic approach is employed to determine the integral gain $k_i$. This concludes the specification of our control strategy for implementation in OpenFAST. In the subsequent subsection, a low-fidelity wind field will be constructed to assess our method's time-varying frequency tracking capability.

### 4-1-3 Low-Fidelity Wind Field

The wake of the upstream turbine is simulated by a custom inflow field generated using TurbSim, a stochastic, full-field turbulence simulator primarily used with Inflow Wind-based simulation tools. It generates three-dimensional wind speed data $U, V, W \in \mathbb{R}^{n_t \times n_y \times n_z}$ in a two-dimensional $YZ$-plane for $n_t$ time steps. The three components are respectively aligned along the positive $X$-axis (downwind), along the positive $Y$-axis (to the left when looking along $X$), and along upwards (positive to gravity), similar to the coordinates shown in Figure 2-1. Here, $Y \in \mathbb{R}^{n_y}$ represents the grid width with $n_y$ data points, $Z \in \mathbb{R}^{n_z}$ denotes the grid height with $m$ data points, and $n_t$ is the number of time steps. In our setup, a $30 \times 20$ grid with 400 meters width and 290 meters height has been selected. The wind speed at hub height will range between $U_{\text{hub}} \approx 7 - 10$ m/s to ensure the experiment is conducted in Region 2, as discussed in Section 4-1-2. This maintains the baseline controller's (ROSCO) blade pitch angle of 0°, while tracking the optimal TSR with PI control.

To generate a flow field resembling a meandering wake behind the upstream turbine, the meandering characteristics outlined in Section 1-2-1 must be satisfied. For performance analysis of our control strategy, a simplified meandering wake will be constructed using a rotating disk. This disk rotates around the turbine's rotor centre with a lateral offset of $0.2D$, and the vertical offset is set to 50% of the lateral displacement. The disk rotates featuring an

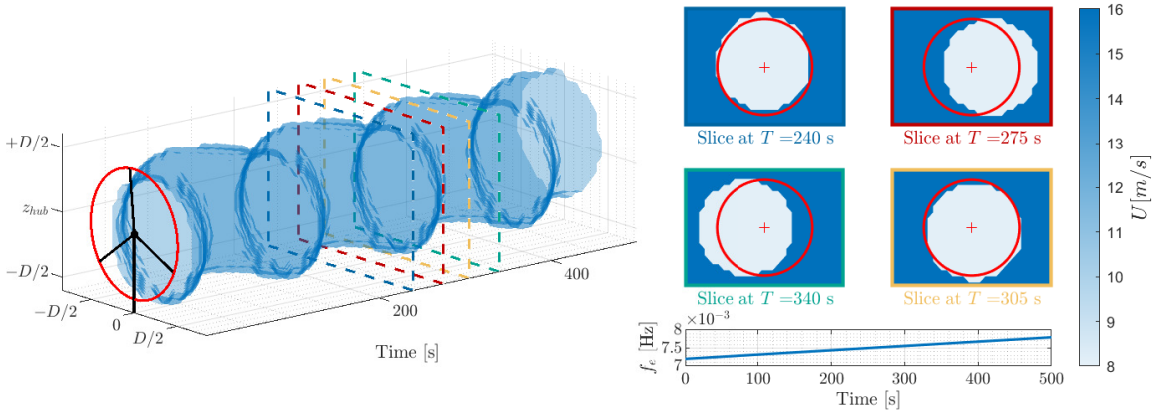


**Figure 4-2:** Inflow field generated by the Clockwise rotating disk, with an ambient wind speed of $U_\infty = 16$ m/s and an interior wake speed of 8 m/s. The red circle denotes the turbine's rotor disk, and the red cross indicates the hub height at 150 meters. Four slices at different time steps are plotted, illustrating the maximum deflection in the $Y$ and $Z$ directions. The excitation frequency $f_e$ is displayed in the bottom right.

increasing excitation frequency $f_e$ from $St = 0.18$ to 0.22. An initial flow field was generated in TurbSim for 1500 seconds with a uniform flow at $U_\infty = 16$ m/s in the $X$-direction, while the $Y$ and $Z$ components were set to 0 m/s. This results in a four-dimensional velocity vector $U_{uvw} \in \mathbb{R}^{n_t \times 3 \times n_y \times n_z}$ for $n_t$ time steps featuring the streamwise $u$, transverse $v$, and vertical $w$ velocity components for each grid point $(y, z)$. The ambient wind speed is set to $U_\infty = 16$ m/s, ensuring the wind speed at hub height is approximately $U_{\text{hub}} \approx 8$ m/s after the conducted modifications. Subsequently, the custom wake is obtained by modifying the velocity vector in Matlab, with the interior of the rotating disk being overwritten to $U_\infty/2 = 8$ m/s. This results in the wake illustrated in Figure 4-2. This simplified inflow allowed us to assess our method's performance during a steadily increasing excitation frequency, as the frequency was known for every time step. To examine our method's phase synchronisation during a wake with higher fidelity, an inflow was generated in Simulator fOr Wind Farm Applications (SOWFA), which will be detailed in the following subsection.

### 4-1-4 High-Fidelity Wind Field

A helical wake with higher fidelity will be generated in SOWFA. This helps to assess the performance of our method in a more realistic simulation environment. SOWFA is a high-fidelity simulation environment, which uses CFD methods to simulate wind flow and turbulence. The generated data comprises streamwise $u$, transverse $v$, and vertical $w$ velocity components for each three-dimensional grid, simulating a helical wake with an increasing excitation frequency starting from Strouhal number of $St = 0.15$ at an ambient wind speed of $U_\infty = 9$ m/s, as depicted in Figure 4-6. Unlike the rotating disk inflow, the helical inflow data includes simulation data at various distances ($X$-direction) from the upstream turbine. Therefore, to apply a similar method to construct an inflow field for OpenFAST, a cross-section in the SOWFA data is selected in the $YZ$-plane at $x = 4D$ to convert the data into a four-dimensional velocity vector $U_{uvw} \in \mathbb{R}^{n_t \times 3 \times n_y \times n_z}$.

Since TurbSim restricts the grid height to be no more than twice the hub height, the $Z$-dimension of the SOWFA data needs to be trimmed accordingly to ensure that the height remains below 300 meters (i.e., $z < 300$). This adjustment reduces the usable grid size of the SOWFA data to $n_y = 28$ and $n_z = 25$. Given that the simulation runs for 1600 seconds with a

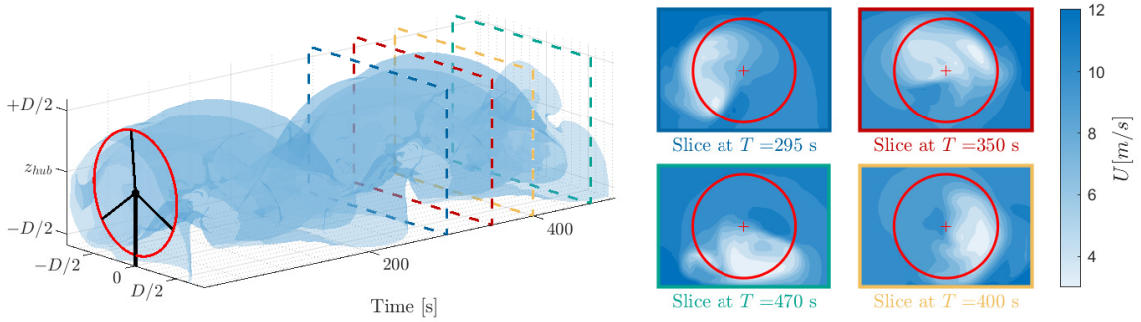


**Figure 4-3:** Inflow field generated in SOWFA at $x/D = 5$ with a constant excitation frequency. The red circle denotes the turbine's rotor disk, and the red cross indicates the hub height at 150 meters. Four slices at different time steps are plotted, illustrating the CW-rotation of the helical wake.

sample time of 2 seconds, the velocity vector becomes $U_{uvw} \in \mathbb{R}^{800\times3\times28\times25}$. This vector can be used, following to the approach outlined in Section 4-1-3, to overwrite the velocity vector of an inflow generated in TurbSim using Matlab. With the construction of the second inflow completed for simulation, the next subsection will focus on practically amplifying or attenuating the meandering wake effect.

### 4-1-5 Enhancement of the Meandering Effect

When implementing phase synchronisation on the meandering wake, the effect can be either amplified or attenuated by adjusting the reference amplitude of the tilt and yaw moments relative to their initial magnitudes before applying the control action. These amplitude references are selected by scaling an initial reference amplitudes of both moments to maintain the phase of the periodic load:

$$\mathbf{M}^{\text{ref}} := \begin{bmatrix} M^{\text{ref}}_{\text{tilt}} & M^{\text{ref}}_{\text{yaw}} \end{bmatrix} = \alpha \begin{bmatrix} M^{0}_{\text{tilt}} & M^{0}_{\text{yaw}} \end{bmatrix} \tag{4-2}$$

where $\alpha$ represents the reference scaling factor, and superscript $(\cdot)^0$ indicates the initial reference magnitude of the tilt and yaw moment, obtained by averaging the amplitudes during the baseline simulation, which are outlined in Table 4-2:

**Table 4-2:** Initial reference magnitude of tilt and yaw moments.

| Inflow | Tilt [kN-m] | Yaw [kN-m] |
|---|---|---|
| Rotating Disk | 7050 | 15490 |
| Helical Inflow | 7870 | 9430 |

Choosing $\alpha > 1$ amplifies the periodic loads induced by the meandering effect, while $\alpha < 1$ attenuates it. Since this report focuses on analysing the impact of phase synchronisation on the meandering effect, only amplitude reference tracking is implemented, excluding offset tracking. By mitigating the meandering effects, fatigue loads on the turbine are expected to decrease, potentially prolonging the turbine's lifespan. The effectiveness of this approach will be assessed by comparing the reduction in specific loads, measured through the standard deviation, between the test cases with phase synchronisation and baseline simulation without it. The focus will be on analysing structural loads using a methodology similar to Van Vondelen et al. [39], as detailed in Table 4-3. The standard deviation reflects the degree of dispersion within a dataset, providing insights into the instability of the aerodynamic loads. Alongside this measure, the averaged generated power will be evaluated, as the primary objective of

**Table 4-3:** Components of the turbine used to compare fatigue loads and power production.

| Component | Direction | Units |
|---|---|---|
| Blade Root Moment | Edgewise & Flapwise | kN-m |
| Tower Top Moment | Fore-aft, Side-side & Torsional | kN-m |
| Tower Base Moment | Fore-aft & Side-side | kN-m |
| Generated Power | – | kW |

wind farms remains maximising power production. Thus, any significant reduction in power output alongside fatigue load mitigation may not be viable for practical implementation.

It is noteworthy that directly evaluating the performance of amplification of the meandering effect is not feasible using OpenFAST since it can only simulate one turbine at a time. Consequently, it cannot directly demonstrate the power improvement across multiple turbines resulting from the amplification. However, Van Vondelen et al. [63] have demonstrated that applying phase synchronisation to amplify the effect of the helical wake increases the overall power performance. Similarly, it can be inferred that amplifying the meandering wake effect, indicated by increased tilt and yaw moments, will enhance wake mixing and deflection, ultimately resulting in a higher overall generated power. However, validation through future work is necessary. Therefore, throughout the remainder of this thesis, successful amplification will be considered as amplifying the tilt and yaw moment while limiting the decrease in generated power. The results of the simulation performed in OpenFAST will be analysed in the following section.

## 4-2 Results in OpenFAST

This section presents the results from various test cases performed using either the rotating disk or SOWFA-generated helical inflow. It is essential to note that using these inflows may violate certain assumptions in OpenFAST since the BEM theory used assumes symmetric loads in the actuator disk [60]. Therefore, large blade deflection could violate this assumption, yielding slightly less accurate results. Nonetheless, it offers valuable insights into the performance of our method. Initially, the rotating disk inflow is utilised to evaluate the time-varying tracking capability of our control method within the turbine simulation environment since the frequency at every time step is known. Subsequently, the simulation using the higher-fidelity helical inflow assesses the performance of our phase synchronisation method under more realistic conditions.

### 4-2-1 Results of the Low-Fidelity Wind Field

Four test cases are conducted to evaluate the performance of our method under varying excitation frequencies. These test cases will set the reference amplitude by changing the scaling factor $\alpha$, with Test Case 1 (TC1) amplifying the effect of the rotating disk, while the test cases TC2 to TC4 will attenuate the periodic effect. The chosen scaling factors are:

| **Name** | TC1 | TC2 | TC3 | TC4 |
|---|---|---|---|---|
| **Scaling factor** $\alpha$ | 1.25 | 0.75 | 0.5 | 0.35 |

All test cases will switch our control strategy activates after $t_{act} = 400$ seconds. The results, showcased in both time and frequency domains in Figure 4-4, undergo post-processing with a zero-phase digital low-pass filter. In the figure, the blue line indicates amplification, while varying levels of attenuation are represented by different shades of red. A detailed comparison of the results is provided in Table 4-4. To ensure accuracy, the initial 600 seconds of the datasets are discarded to eliminate transient effects in the simulation. This approach allows

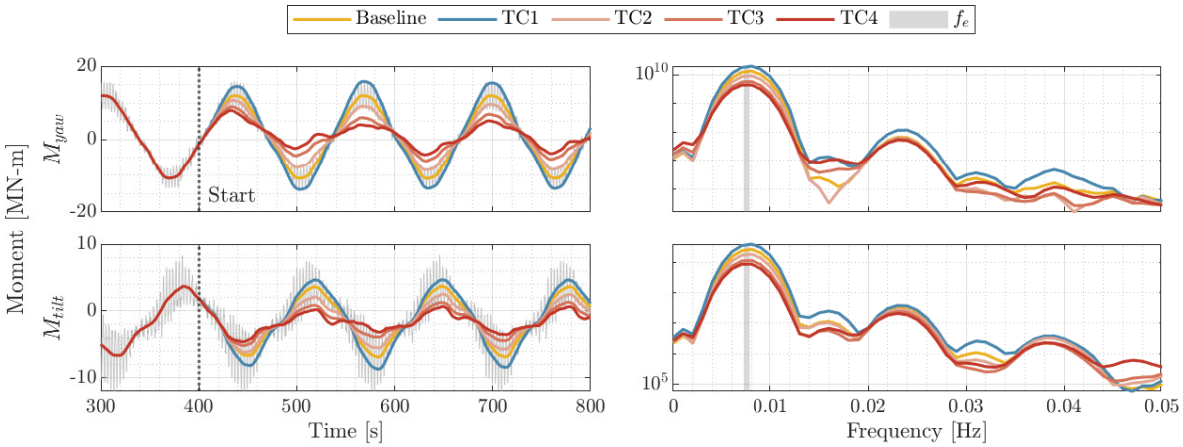


**Figure 4-4:** Results of phase synchronisation applied to the rotating disk inflow with **Left:** time-, and **Right:** frequency-domain response for various test cases for **Top:** tilt-, and **Bottom:** yaw moment.

for a comparison of 900 seconds of simulation time for each test case against the baseline simulation in terms of the Standard Deviation (STD) of bending moments and averaged generated power. Figure 4-4 indicates that our phase synchronisation method successfully amplifies and attenuates the meandering effect while accurately tracking the continuously increasing excitation frequency of the constructed rotating disk inflow. This is also shown in the right plot of Figure 4-5 displaying the frequency estimates of all test cases. However, these estimates exhibit some harmonic ripple, consistent with the findings in Chapter 3. Test Case 1 shows a 25% increase in amplitude in the time-domain response, which is also evident in the frequency-domain by the heightened peak at the excitation frequency compared to the baseline simulation. Importantly, this increase in amplitude does not result in any loss of generated power, as outlined in the last row of Table 4-4. The attenuation of the meandering effect (TC2 to TC4) displays a similar response, but with respectively a 25%, 50% and 65% decrease in amplitude, along with lowered peaks at the excitation frequency. Consequently,

**Table 4-4:** Comparison of the standard deviation of the bending moments and generated power with the baseline (BL) case for the constructed rotating disk inflow in Clockwise direction.

| **Component** | **Direction** | **Unit** | **Test Cases [Δ%]** | | | | |
|---|---|---|---|---|---|---|---|
| | | | **BL** | **TC1** | **TC2** | **TC3** | **TC4** |
| Blade Root | Edgewise | kN-m | 13336 | +1.3 | −0.5 | −0.9 | −1.0 |
| | Flapwise | kN-m | 8574 | +13.3 | −10.8 | −22.0 | −27.9 |
| Tower Top | Fore-aft | kN-m | 6201 | +19.4 | −16.3 | −34.3 | −43.5 |
| | Side-side | kN-m | 2560 | +5.9 | −0.2 | −2.5 | −2.8 |
| | Torsional | kN-m | 11323 | +28.0 | −22.6 | −47.0 | −60.9 |
| Tower Base | Fore-aft | kN-m | 31597 | −0.3 | −2.6 | −6.1 | −8.0 |
| | Side-side | kN-m | 10977 | +22.3 | −0.8 | −15.4 | −16.0 |
| Generated Power | – | kW | 10464 | +0.1 | −0.9 | −2.7 | −4.0 |

this leads to decreased STDs of the fatigue loads, as detailed in Table 4-4, reducing the instability of the aerodynamic loads. While higher levels of attenuation correspond to greater decreases, they also result in greater power loss. Notably, Test Case 2 shows promising results since all STDs are decreased while showing an acceptable loss in the power production of 1%.

The left plots of Figure 4-5 depict the convergence of amplitude reference errors towards zero for all test cases. However, noticeable oscillations of similar magnitude are observed around the zero tracking error. These oscillations could arise from conflicting control actions applied by the components of our control strategy, triggered by any phase or amplitude error. An inaccurately chosen initial reference value of the amplitudes can lead to an imbalance in the ratio between the tilt and yaw moment, resulting in a phase different from the excitation phase of the periodic load. Consequently, the PLL corrects the phase error to zero, inducing an amplitude error. Subsequently, the reference controller attempts to rectify the amplitude error, potentially introducing a slight phase error and initiating a feedback loop resulting in these oscillations. Nonetheless, these oscillations are relatively small and do not significantly hinder system performance, and they could be mitigated by fine-tuning the chosen initial values. Hence, it can be concluded that our phase synchronisation strategy effectively amplifies and attenuates the time-varying meandering effect. Consequently, the subsequent subsection will delve into a more detailed analysis of the performance using the higher-fidelity inflow generated in SOWFA.

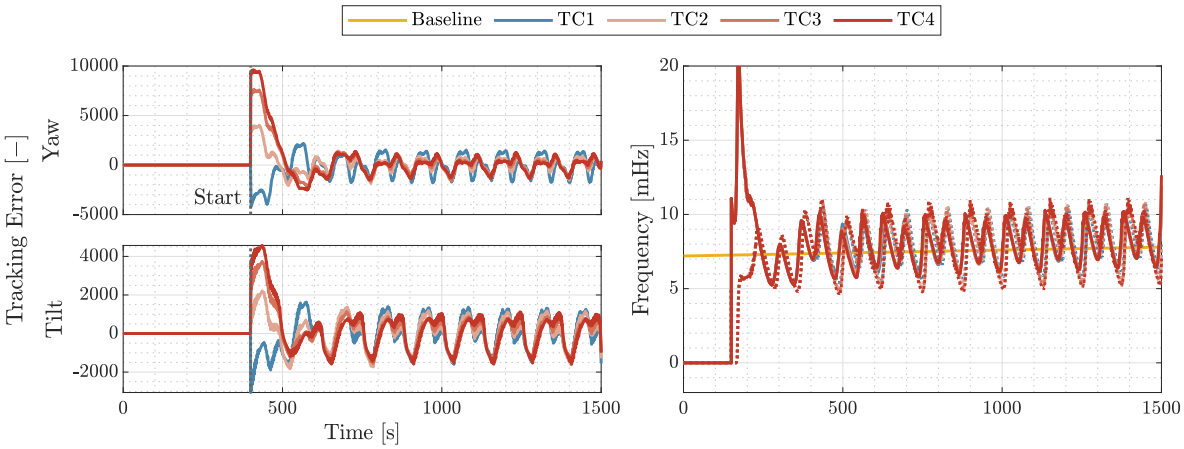


**Figure 4-5:** Results of phase synchronisation applied to the rotating disk inflow in the time-domain with **Left:** Reference error for **Top:** tilt and **Bottom:** yaw moment. **Right:** Frequency estimation

## 4-2-2 Results of the Higher-Fidelity Wind Field

Finally, the performance of our method will be evaluated using the higher-fidelity helical inflow generated in SOWFA. Based on the results obtained from the low-fidelity wind field, which suggested that excessive attenuation might not be feasible for commercial applications, this section will primarily focus on amplifying the meandering effect. Therefore, the test cases in Table 4-5 were performed. The results in both the time and frequency domain are illustrated in Figure 4-6. In the figure, amplification is represented by blue lines, while attenuation is indicated by red. The different shades denote varying levels of amplification and attenuation.

**Table 4-5:** Test cases simulated using the helical wake for various amplitude reference scaling factors $\alpha$.

| **Name** | TC1 | TC2 | TC3 | TC4 | TC5 | TC6 |
|---|---|---|---|---|---|---|
| **Scaling factor** $\alpha$ | 2 | 1.75 | 1.5 | 1.25 | 0.75 | 0.5 |

The right plot of Figure 4-6 illustrates the Welch Power Spectrum for the various test cases. Interestingly, in the baseline scenario, the peak energy contribution at the excitation frequency appears less pronounced compared to the findings discussed in Section 4-2-1. Furthermore, the peaks corresponding to the 3$^{\text{rd}}$ and 5$^{\text{th}}$ harmonics almost disappear. This suggests a relatively lower energy contribution of the excitation frequency, likely due to the wind field's increased complexity. This trend persists across all test cases. Nevertheless, effective amplification and attenuation of the meandering effect are evident, as indicated by the heightened and lowered peaks at $f_e$. However, this effect also extends to other frequencies, with a more pronounced impact on the tilt than the yaw moment. Specifically, the amplification of the yaw moment results in an increased peak at $f_e$, accompanied by distinct increases at its 3$^{\text{rd}}$ and 5$^{\text{th}}$ harmonics. Conversely, the tilt moment amplifies across a wider frequency range, indicated by the increased overall energy contribution. This disparity suggests that the phase synchronisation strategy is more effective on the yaw moment than the tilt, a trend also evident in the time domain response depicted in the left plot of Figure 4-6. The response

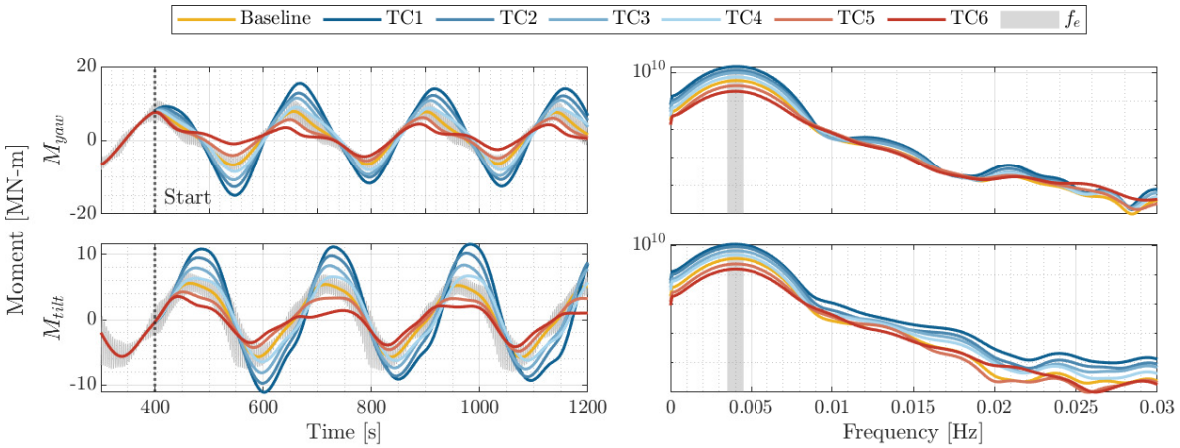


**Figure 4-6:** Results of phase synchronisation applied to the helical inflow with **Left:** time-, and **Right:** frequency-domain response for various test cases for **Top:** tilt-, and **Bottom:** yaw moment.

of the yaw moment mirrors that of the baseline case, with either an increased or reduced amplitude. Conversely, the tilt's response exhibits notable changes in shape, accompanied by an additional shift at the zero-crossing. Excessive amplification of frequencies other than the wake's excitation frequency could explain the former effect, while the latter could also be attributed to a shift in the moment's centerline. This shift is highlighted by the moments' biases illustrated in the right plot of Figure 4-7, where the bias is measured concerning the zero centreline. It's clear that different levels of enhancement result in varying biases, with larger amplification or attenuation leading to greater biases.

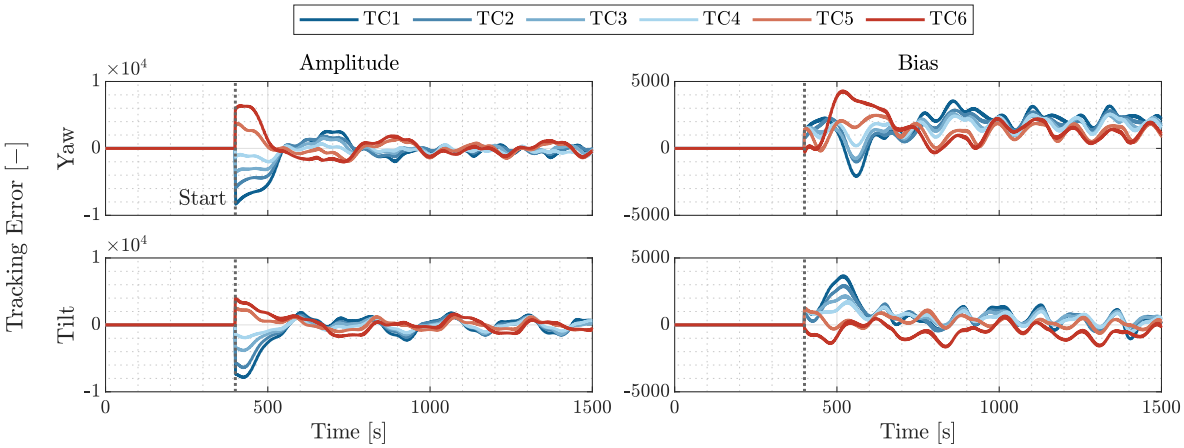


**Figure 4-7:** Results of phase synchronisation applied to the helical inflow in the time-domain with the tracking error of the **Left:** amplitude and **Right:** bias for **Top:** tilt and **Bottom:** yaw moment.

This section concludes with a comparison of the bending moments' standard deviation and the average generated power across all test cases against the baseline scenario. After discarding transient data preceding 600 seconds to ensure accuracy, a comparison over a 900-second simulation period was conducted. The results, as outlined in Table 4-6, revealed distinct trends: amplification led to increased standard deviation of the bending moments, while attenuation resulted in reductions. Moreover, the level of amplification and attenuation showed a direct correlation with greater power loss. The bending moments primarily affected by phase synchronisation are the fore-aft and torsional moments of the tower top, along with the flapwise blade root moment, which is consistent with previous findings. Notably, the tower base side-side load fluctuations significantly decrease compared to low-fidelity simulations. This reduction is attributed to the smaller velocity differences inside the wake compared to the ambient wind speed, resulting in lower load variations. The phase synchronisation test cases with the most significant impact were TC1 and TC6. Test Case 1 amplified the magnitude of

**Table 4-6:** Comparison of the standard deviation of fatigue loads and generated power with the baseline (BL) case for the generated helical inflow.

| Component | Direction | Unit | Test Cases [Δ%] | | | | | | |
|---|---|---|---|---|---|---|---|---|---|
| | | | **BL** | **TC1** | **TC2** | **TC3** | **TC4** | **TC5** | **TC6** |
| Blade Root | Edgewise | kN-m | 13345 | 2.7 | 2.0 | 1.2 | 0.9 | −0.5 | −0.7 |
| | Flapwise | kN-m | 6892 | 40.6 | 28.4 | 18.5 | 7.0 | −7.8 | −13.7 |
| Tower Top | Fore-aft | kN-m | 6948 | 80.8 | 63.4 | 38.6 | 19.7 | −21.0 | −38.8 |
| | Side-side | kN-m | 1630 | 17.6 | 11.1 | 6.8 | 9.4 | −2.3 | −2.0 |
| | Torsional | kN-m | 7507 | 84.6 | 57.6 | 42.5 | 18.5 | −19.2 | −37.7 |
| Tower Base | Fore-aft | kN-m | 38334 | 6.2 | 6.4 | 3.6 | 0.4 | −3.1 | −5.9 |
| | Side-side | kN-m | 12845 | 1.1 | 7.1 | 5.0 | 3.6 | −1.6 | −3.3 |
| Gen. Power | – | kW | 5644 | −1.8 | −0.1 | 0.6 | −0.3 | −1.1 | −2.7 |

the tilt and yaw moments by 100%, potentially increasing wake mixing and wake defection. Conversely, TC6 notably reduced the overall bending moments' STD by $-5.6\%$. While both test cases show promise in improving power performance or extending the turbines' lifespan, they both violated the acceptable power loss thresholds, rendering them non-viable for commercial applications. In contrast, the other test cases stayed within this threshold. This indicates that the meandering effect on the tilt and yaw moments can be amplified by up to 75% (TC2), while attenuation can lead to an average reduction of the bending loads' standard deviation by $-3.1\%$ (TC5). Interestingly, Test Case 3 displayed a 0.6% power gain, which contradicts the typical expectation that additional pitch actuation would result in power loss. This unexpected gain could be attributed to suboptimal control settings applied by ROSCO.

## 4-3 Concluding remarks

This chapter has undertaken an in-depth evaluation of the MSTOGI-HTan-QT2PLL methodology within the simulation framework of OpenFAST. Initially, the method's time-varying frequency tracking capability was analysed using a constructed low-fidelity wind field in MATLAB, where the excitation frequency was known at each time step. This allowed for the validation of our method's frequency estimation performance under increasing frequencies. Minor oscillations in the reference error were observed during the simulations, potentially arising from conflicting control actions triggered by phase or amplitude errors within the control strategy. However, these oscillations were relatively small and did not significantly impair system performance. Subsequently, the fidelity of the wind field was increased to assess the method's performance under more realistic conditions. The increased contribution of frequencies other than the wake's excitation frequency $f_e$, likely attributed to the higher fidelity of the wind field, made it more challenging to amplify the meandering effect solely at $f_e$. This challenge was particularly evident in the response of the tilt moment during amplification, as demonstrated in both the time and frequency domains.

A direct demonstration of amplifying the meandering effect across multiple turbines wasn't feasible in OpenFAST. However, the potential for amplifying the meandering effect was evident through an increasing magnitude of the tilt and yaw moments without sacrificing generated power. This suggests that amplification could enhance wake mixing further upstream and induce larger wake deflection [40], resulting in increased available energy at the downstream turbine. On the other hand, attenuating the meandering effect reduced the deviation of bending moments but also led to greater power loss. Hence, there exists a tradeoff between load reduction and power preservation. A magnitude reduction of 25% on the tilt and yaw moment resulted in an overall decrease of $-3.1\%$ in the bending moments' Standard Deviation (STD), while maintaining its power loss within an acceptable threshold of 1%. More excessive attenuation will further decrease the STDs, extending the turbines' lifespan, but may not be feasible for commercial applications due to the considerable power loss incurred.

# Chapter 5

# Conclusions and Recommendations

## 5-1 Conclusions

As wind farms expand and turbine sizes increase, challenges associated with wake effects and turbine interactions become more pronounced. Therefore, wind farm control strategies have been developed to mitigate the negative effects of wakes, consequently enhancing overall power production or reducing fatigue loads. The helix approach has emerged as a promising method for controlling wake dynamics, forming the wake into a helical shape to increase wake mixing further downstream. In this context, phase synchronisation has emerged as an extension of the helix approach, simultaneously applying the helix on up- and downstream turbines. By leveraging the existing helical periodic components induced by the upstream turbine, phase synchronisation can initiate the helix at the downstream turbine with less pitch action.

However, power is still compromised at the upstream turbine due to the execution of the helix. Consequently, the potential for improvement arises with the integration of phase synchronisation onto the meandering effect—a phenomenon often already present at the downstream turbine. This effect yields benefits similar to those of the helical wake concerning wake recovery, offering the potential to improve overall power performance without power loss at the upstream turbine. Therefore, the primary objective of this MSc Thesis was to investigate the potential of integrating phase synchronisation to enhance the meandering effect. To address this objective, the following main research question was formulated:

*How can the meandering effect of an incoming wake be harnessed at the downstream turbine to enhance overall performance?*

---

To address this question, three sub-questions were formulated initially in Chapter 1 to provide deeper insights, facilitating the formulation of the main conclusion of this thesis.

1. *How can wake meandering be identified based on inflow information at the downstream turbine?*

Identifying the meandering effect based on inflow information involves understanding the periodic loads imposed by the meandering wake on the rotor disk. Valuable wake information is embedded within the Blade root Out-of-Plane moments with its peak energy contribution at $f_e + 1P$. Applying a Multi-Blade Coordinate (MBC) transform shifts this peak to the wake's excitation frequency $f_e$. Consequently, all necessary information about the meandering effect is present at this frequency. This thesis has demonstrated that the ESOGI- and MSTOGI-HTan-QT2PLL methodologies effectively extract the meandering information by estimating the key characteristics—phase, amplitude, and offset—at the fundamental frequency of the tilt and yaw moment located at $f_e$. Moreover, enhancements to the conventional SOGI-PLL structure have improved stability and performance during offset and frequency variations. The ESOGI and MSTOGI structures accurately estimate the signal's offset while effectively managing internal disturbances originating from offsets. The addition of the HTan module enhances system stability, while the QT2PLL module ensures precise phase tracking during phase and frequency jumps and during frequency ramps. In our validation study, both methodologies demonstrated effectiveness during amplification and attenuation under uncertain conditions, successfully providing the phase, amplitude, and offset required to implement the downstream turbine's closed-loop meandering control strategy. The validation study showed better performance for MSTOGI-HTan-QT2PLL compared to ESOGI-HTan-QT2PLL.

2. *How can phase synchronisation be effectively initiated to accommodate the time-varying nature of meandering wake?*

Effectively initiating phase synchronisation to accommodate the meandering wake involves addressing the rotor disk's highly coupled Multiple-Input Multiple-Output (MIMO) structure, which requires advanced control strategies. Implementing a MBC-transform resolves this issue by changing the structure into two Single-Input Single-Output (SISO) configurations, allowing for implementing simple control strategies. Our validation study demonstrated that integral action could effectively be employed for reference tracking using the extracted amplitude and offset to amplify or attenuate the system towards a specified reference. This strategy is also effective in OpenFAST for amplification and attenuation of the meandering wake. The reference control effort produced two pitch amplitudes, $A^c_{\text{tilt}}$ and $A^c_{\text{yaw}}$, which, combined with their estimated phase, determined the tilt and yaw pitch angles. These angles were then translated into individual pitch angles using an inverse MBC-transform. By incorporating an additional azimuth offset in the inverse, the phase lag induced by coupling and actuator delays could be effectively compensated for. However, it's important to note that while integral control has shown efficacy in mitigating amplitude errors across various test cases, its performance may deteriorate in scenarios characterised by significant magnitude fluctuations, suggesting the necessity for more advanced controllers. Additionally, experiments conducted in OpenFAST with a higher-fidelity wind field revealed challenges posed by the wake's complexity. This complexity, characterised by a relatively lower energy contribution of the wake's excitation frequency in its frequency domain, was demonstrated through Welch's Power Spectra. These spectra showed a decrease in the peak energy contribution at

$f_e$, accompanied by the near disappearance of peaks at the $3^{\text{rd}}$ and $5^{\text{th}}$ harmonics, particularly pronounced in the tilt moment. Consequently, the controller encountered difficulties in solely amplifying the meandering effect at $f_e$ on the tilt axis, while the effect on attenuation appeared to be less evident. However, on the yaw axis, where both amplification and attenuation were observed, the challenges were less prominent.

3. *What impacts does enhancing the meandering effect have on power performance and fatigue loads?*

Enhancing the meandering effect in wind turbines has implications for both power performance and fatigue loads. A meandering wake introduces periodic loads on the turbine, which can increase fatigue loads and potentially shorten the turbine's lifespan. However, it can also yield advantageous effects such as improved wake mixing further downstream and larger wake deflection. The overall impact of enhancing meandering depends on balancing these opposing factors. Our phase synchronisation method has demonstrated the ability to increase the magnitude of tilt and yaw by up to 75% with minimal power loss. This amplification could heighten the meandering's beneficial aspects, potentially increasing available energy downstream. However, the amplification also showed a significant increase in deviations in the bending moments, primarily affecting the fore-aft and torsional moments of the tower top, along with the flapwise blade root moment. Conversely, our method also managed to reduce the magnitude of tilt and yaw moments by 25% while still keeping power loss within the acceptable threshold of 1%. This resulted in an overall decrease of $-3.1\%$ in the bending moments' standard deviation. Further attenuation could diminish these deviations even more, thereby extending turbine lifespan, but this would also result in greater power loss, which might not be viable for commercial applications. Furthermore, decreasing the meandering effect also reduces its beneficial effects, potentially impacting downstream turbines' power performance as well. Since OpenFAST can only simulate a single-turbine setting, this balance should be investigated in a multi-turbine setting during future work. This would provide a more comprehensive understanding of how amplifying or attenuating the meandering effect affects the overall wind farm power performance.

With all sub-questions addressed, it can be concluded that the meandering effect can be harnessed at downstream turbines by extracting its key characteristics—phase, amplitude, and offset—at the wake's excitation frequency. Our phase synchronisation approach holds the potential to improve the wind farm's overall power performance through amplification or mitigating fatigue loads via attenuation, thereby potentially extending the turbines' lifespan. This thesis represents one of the initial applications of phase synchronisation on the meandering effect amidst time-varying frequencies. However, further research is necessary to delve deeper into this application. The subsequent subsection will outline recommendations for future investigations to explore this topic further.

## 5-2 Recommendations

This MSc Thesis has taken the initial steps in integrating phase synchronisation to address the meandering effect, revealing promising potential. However, future research is essential to fully validate its potential. This section will propose recommendations for future investigation.

1. *Investigate the impact of meandering phase synchronisation in a multi-turbine simulation environment* — This would enable a comprehensive investigation into the impact of amplification, which involves analysing the increased wake recovery at downstream turbines to understand how different levels of amplification affect overall power performance. Additionally, comparing the power performance achieved with helix phase synchronisation to that achieved solely with the meandering effect could provide valuable insights. Specifically, investigating if excluding the helix on the upstream turbine increases the overall power performance. Furthermore, the effects of attenuation should be further investigated. Mitigating the meandering effect could have implications not only for the power performance of the turbine applying phase synchronisation but also for the performance of downstream turbines since the beneficial meandering effects are also mitigated. Therefore, a thorough analysis of the total power performance is necessary to assess the feasibility of attenuating the meandering effect in commercial applications.

2. *Explore advanced controller designs for reference tracking* — During scenarios with significant amplitude fluctuations, using integral action for reference control may not effectively mitigate the tracking errors. Hence, more advanced control strategies to handle these fluctuations should be investigated. Additionally, the process of setting reference amplitudes could be improved. Inaccurate initial values could disrupt performance if they deviate from the tilt/yaw ratio before applying phase synchronisation. This discrepancy may impact the preservation of the estimated phase and potentially initiate a feedback loop between the reference controllers and the PLL, leading to oscillations in the tracking error. Therefore, exploring alternative methods for setting amplitude references could significantly enhance control performance.

3. *Develop a systematic approach to determine the azimuth offset* — While the azimuth offset was determined heuristically in this thesis, a more systematic approach could enhance performance. Exploring methods to determine the optimal azimuth offset would be advantageous.

4. *Investigate the effect of partial wake overlap* — A SOGI-PLL can estimate essential characteristics—phase, amplitude, and offset—of a non-sinusoidal signal, however, its application to partially measured signals is yet unexplored. Hence, exploring the impact of partial wake overlap would be valuable, particularly to evaluate our method's capability to extract meandering characteristics at its excitation frequency in such scenarios.

# Appendix A

# Mathematical Derivation

## A-1 Transfer functions

### A-1-1 Extended Second-Order Generalized Integrator (ESOGI)

Let us begin by writing down all three output signals:

$$\begin{aligned} u_\alpha(s) &= \left(ke(s) - \frac{\hat{\omega}}{s}u_\alpha(s)\right)\frac{\hat{\omega}}{s} \\ u_\beta(s) &= \frac{\hat{\omega}}{s}u_\alpha(s) \\ u_{dc}(s) &= k_{dc}\frac{\hat{\omega}}{s}e(s) \end{aligned} \tag{A-1}$$

where $e(s) = u(s) - (u_{dc}(s) + u_\alpha(s))$. Let's start by expanding (A-1) with the error term $e(s)$:

$$\begin{aligned} u_\alpha(s) &= \left(k(u(s) - (u_{dc}(s) + u_\alpha(s))) - \frac{\hat{\omega}}{s}u_\alpha(s)\right)\frac{\hat{\omega}}{s} \\ \left(s + k\hat{\omega} + \frac{\hat{\omega}^2}{s}\right)u_\alpha(s) &= k\hat{\omega}(u(s) - u_{dc}(s)) \\ \left(s^2 + k\hat{\omega}s + \hat{\omega}^2\right)u_\alpha(s) &= k\hat{\omega}s(u(s) - u_{dc}(s)) \end{aligned} \tag{A-2a}$$

$$\begin{aligned} u_{dc}(s) &= k_{dc}\frac{\hat{\omega}}{s}(u(s) - (u_{dc}(s) + u_\alpha(s))) \\ (s + k_{dc}\hat{\omega})\,u_{dc}(s) &= k_{dc}\hat{\omega}\,(u(s) - u_\alpha(s)) \end{aligned} \tag{A-2b}$$

Next, (A-2) must be rewritten such that all relations only exist out of terms of themselves and $u(s)$ to successfully obtain the transfer function of the output signals concerning the input

signal. Here, the first step is to substitute (A-2b) into (A-2a):

$$\begin{aligned}
\left(s^2 + k\hat{\omega}s + \hat{\omega}^2\right) u_\alpha(s) &= k\hat{\omega}s \left(u(s) - \frac{k_{dc}\hat{\omega}}{s + k_{dc}\hat{\omega}}(u(s) - u_\alpha(s)\right) \\
\left(s^2 + k\hat{\omega}s + \hat{\omega}^2 - \frac{kk_{dc}\hat{\omega}^2 s}{s + k_{dc}\hat{\omega}}\right) u_\alpha(s) &= k\hat{\omega}s \left(1 - \frac{k_{dc}\hat{\omega}}{s + k_{dc}\hat{\omega}}\right) u(s) \\
\left((s^2 + k\hat{\omega}s + \hat{\omega})(s + k_{dc}\hat{\omega}) - kk_{dc}\hat{\omega}^2 s\right) u_\alpha(s) &= k\hat{\omega}s \left(s + k_{dc}\hat{\omega} - k_{dc}\hat{\omega}\right) u(s) \\
\left(s^3 + (k + k_{dc})\hat{\omega}s^2 + \hat{\omega}^2 s + k_{dc}\hat{\omega}^3\right) u_\alpha(s) &= k\hat{\omega}s^2 u(s)
\end{aligned} \tag{A-3}$$

This results in the following transfer function $G_\alpha(s)$:

$$G_\alpha(s) = \frac{u_\alpha(s)}{u(s)} = \frac{k\hat{\omega}s^2}{s^3 + (k + k_{dc})\hat{\omega}s^2 + \hat{\omega}^2 s + k_{dc}\hat{\omega}^3} \tag{A-4}$$

By substituting (A-4) in (A-1), the relation between $u_\beta(s)$ and $u(s)$ can be obtained:

$$\begin{aligned}
u_\beta(s) &= \frac{\hat{\omega}}{s} \frac{k\hat{\omega}s^2}{s^3 + (k + k_{dc})\hat{\omega}s^2 + \hat{\omega}^2 s + k_{dc}\hat{\omega}^3} u(s) \\
&= \frac{k\hat{\omega}^2 s}{s^3 + (k + k_{dc})\hat{\omega}s^2 + \hat{\omega}^2 s + k_{dc}\hat{\omega}^3} u(s)
\end{aligned} \tag{A-5}$$

Hence, the transfer function $G_\beta(s)$ becomes:

$$G_\beta(s) = \frac{u_\beta(s)}{u(s)} = \frac{k\hat{\omega}^2 s}{s^3 + (k + k_{dc})\hat{\omega}s^2 + \hat{\omega}^2 s + k_{dc}\hat{\omega}^3} \tag{A-6}$$

Finally, by substituting (A-2a) into (A-2b), the relation between the $u_{dc}(s)$ and $u(s)$ can be found:

$$\begin{aligned}
\left(s + k_{dc}\hat{\omega}\right) u_{dc}(s) &= k_{dc}\hat{\omega} \left(u(s) - \frac{k\hat{\omega}s}{s^2 + k\hat{\omega}s + \hat{\omega}^2}(u(s) - u_{dc}(s))\right) \\
\left(s + k_{dc}\hat{\omega} - \frac{kk_{dc}\hat{\omega}^2 s}{s^2 + k\hat{\omega}s + \hat{\omega}^2}\right) u_{dc}(s) &= \frac{k_{dc}\hat{\omega}\left(s^2 + \hat{\omega}^2\right)}{s^2 + k\hat{\omega}s + \hat{\omega}^2} u(s) \\
\left((s + k_{dc}\hat{\omega})(s^2 + k\hat{\omega}s + \hat{\omega}^2) - kk_{dc}\hat{\omega}^2 s\right) u_{dc}(s) &= k_{dc}\hat{\omega} \left(s^2 + \hat{\omega}^2\right) u(s) \\
\left((s^3 + (k + k_{dc})\hat{\omega}s^2 + \hat{\omega}^2 s + k_{dc}\hat{\omega}^3\right) u_{dc}(s) &= k_{dc}\hat{\omega} \left(s^2 + \hat{\omega}^2\right) u(s)
\end{aligned} \tag{A-7}$$

This results in the transfer function $G_{dc}(s)$:

$$G_{dc}(s) = \frac{u_{dc}(s)}{u(s)} = \frac{k_{dc}\hat{\omega}(s^2 + \hat{\omega}^2)}{s^3 + (k + k_{dc})\hat{\omega}s^2 + \hat{\omega}^2 s + k_{dc}\hat{\omega}^3} \tag{A-8}$$

### A-1-2 Mixed Second- and Third-Order Generalized Integrator (MSTOGI)

Let us begin by writing down all three output signals:

$$\begin{aligned}
u_\alpha(s) &= \left(ke(s) - \frac{\hat{\omega}}{s} u_\alpha(s)\right) \frac{\hat{\omega}}{s} \\
u_\beta(s) &= \frac{\hat{\omega}}{s} u_\alpha(s) - u_{dc}(s) \\
u_{dc}(s) &= \frac{\hat{\omega}}{s}(ke(s) - u_{dc}(s))
\end{aligned} \tag{A-9}$$

where $e(s) = u(s) - u_\alpha(s)$. Let's start again by expanding (A-9):

$$\begin{aligned} u_\alpha(s) &= \left(k(u(s) - u_\alpha(s)) - \frac{\hat{\omega}}{s}u_\alpha(s)\right)\frac{\hat{\omega}}{s} \\ \left(s^2 + k\hat{\omega}s + \hat{\omega}^2\right)u_\alpha(s) &= k\hat{\omega}s \cdot u(s) \end{aligned} \tag{A-10a}$$

$$\begin{aligned} u_\beta(s) &= \frac{\hat{\omega}}{s}\frac{k\hat{\omega}s}{s^2 + k\hat{\omega}s + \hat{\omega}^2} \cdot u(s) - u_{dc}(s) \\ &= \frac{k\hat{\omega}^2}{s^2 + k\hat{\omega}s + \hat{\omega}^2} \cdot u(s) - u_{dc}(s) \end{aligned} \tag{A-10b}$$

$$\begin{aligned} u_{dc}(s) &= \frac{\hat{\omega}}{s}\left(k(u(s) - u_\alpha(s)) - u_{dc}(s)\right) \\ (s + \hat{\omega})\,u_{dc}(s) &= k\hat{\omega}(u(s) - u_\alpha(s)) \\ &= k\hat{\omega}\left(u(s) - \frac{k\hat{\omega}s}{s^2 + k\hat{\omega}s + \hat{\omega}^2} \cdot u(s)\right) \\ &= \frac{k\hat{\omega}\left(s^2 + \hat{\omega}^2\right)}{s^2 + k\hat{\omega}s + \hat{\omega}^2} \cdot u(s) \end{aligned} \tag{A-10c}$$

To obtain the relation between $u_\beta(s)$ and $u(s)$, we can substitute (A-14) into (A-10b):

$$\begin{aligned} u_\beta(s) &= \frac{k\hat{\omega}^2}{s^2 + k\hat{\omega}s + \hat{\omega}^2} \cdot u(s) - \frac{k\hat{\omega}(s^2 + \hat{\omega}^2)}{(s + \hat{\omega})(s^2 + k\hat{\omega}s + \hat{\omega}^2)} \cdot u(s) \\ &= \frac{k\hat{\omega}s(\hat{\omega} - s)}{(s + \hat{\omega})(s^2 + k\hat{\omega}s + \hat{\omega}^2)} \cdot u(s) \end{aligned} \tag{A-11}$$

Therefore the transfer functions of the MSTOGI stucture become:

$$G_\alpha(s) = \frac{u_\alpha(s)}{u(s)} = \frac{k\hat{\omega}s}{s^2 + k\hat{\omega}s + \hat{\omega}^2} \tag{A-12}$$

$$G_\beta(s) = \frac{u_\beta(s)}{u(s)} = \frac{k\hat{\omega}s(\hat{\omega} - s)}{(s + \hat{\omega})(s^2 + k\hat{\omega}s + \hat{\omega}^2)} \tag{A-13}$$

$$G_{dc}(s) = \frac{u_{dc}(s)}{u(s)} = \frac{k\hat{\omega}(s^2 + \hat{\omega}^2)}{(s + \hat{\omega})(s^2 + k\hat{\omega}s + \hat{\omega}^2)} \tag{A-14}$$

## A-2 Design Guideline for $k_{dc}$

The choice of the dc-gain $k_{dc}$ in (2-11) can be determined based on the poles of

$$\Delta_1(s) = s^3 + (k + k_{dc})\hat{\omega}s^2 + \hat{\omega}^2 s + k_{dc}\hat{\omega}^3. \tag{A-15}$$

By choosing the poles of $\Delta_1(s)$ as a real pole $m\alpha$ and a complex conjugate pair $\alpha \pm j\beta$, the characteristics equation becomes:

$$\begin{aligned}\Delta_1(s) &= (s + m\alpha)(s + \alpha + j\beta)(s + \alpha - j\beta) \\ &= (s + m\alpha)(s^2 + 2\alpha s + (\alpha^2 + \beta^2)) \\ &= s^3 + (m+2)\alpha s^2 + \left((2m+1)\alpha^2 + \beta^2\right) s + m\alpha(\alpha^2 + \beta^2)\end{aligned} \tag{A-16}$$

From (A-15) and (A-16), the following relationships are obtained:

$$(k + k_{dc})\hat{\omega} = (m+2)\alpha \tag{A-17a}$$

$$\hat{\omega}^2 = (2m+1)\alpha^2 + \beta^2 \tag{A-17b}$$

$$k_{dc}\hat{\omega}^3 = m\alpha(\alpha^2 + \beta^2) \tag{A-17c}$$

By manipulating (A-17c), $\alpha$ and $\beta$ can be written in terms of $\hat{\omega}$, $k$ and $k_{dc}$:

$$\alpha = \hat{\omega}\left(\frac{k + k_{dc}}{m+2}\right) \qquad \beta = \sqrt{\hat{\omega}^2 - \hat{\omega}^2(2m+1)\left(\frac{k + k_{dc}}{m+2}\right)^2} \tag{A-18}$$

Now, if (A-18) is substituted in (A-17c), the solution can be written only in terms of $k$, $k_{dc}$ and $m$:

$$\begin{aligned} m\hat{\omega}\left(\frac{k + k_{dc}}{m+2}\right)\left(\hat{\omega}^2\left(\frac{k + k_{dc}}{m+2}\right)^2 + \left(\hat{\omega}^2 - \hat{\omega}^2(2m+1)\left(\frac{k + k_{dc}}{m+2}\right)^2\right)\right) &= k_{dc}\hat{\omega}^3 \\ m\hat{\omega}^3\left(\frac{k + k_{dc}}{m+2}\right)\left(\left(\frac{k + k_{dc}}{m+2}\right)^2 + 1 - (2m+1)\left(\frac{k + k_{dc}}{m+2}\right)^2\right) &= k_{dc}\hat{\omega}^3 \\ m\left(\frac{k + k_{dc}}{m+2}\right)\left(1 - 2m\left(\frac{k + k_{dc}}{m+2}\right)^2\right) &= k_{dc} \\ 2m^2\left(\frac{k + k_{dc}}{m+2}\right)^3 - m\left(\frac{k + k_{dc}}{m+2}\right) + k_{dc} &= 0 \end{aligned} \tag{A-19}$$

Next, (A-19) will further expended such that it matches the form $k_{dc}^3 + ak_{dc}^2 + bk_{dc} + c = 0$:

$$\begin{aligned} (k + k_{dc})^3 - \left(\frac{(m+2)^2}{2m}\right)(k + k_{dc}) + \left(\frac{(m+2)^3}{2m^2}\right)k_{dc} &= 0 \\ (k + k_{dc})^3 + \left(\frac{(m+2)^2}{2m}\left(1 - \frac{m+2}{m}\right)\right)k_{dc} - \left(\frac{(m+2)^2}{2m}\right)k &= 0 \\ (k + k_{dc})^3 + \left(\frac{m+2}{m}\right)^2 k_{dc} - \left(\frac{(m+2)^2}{2m}\right)k &= 0 \end{aligned} \tag{A-20}$$

Therefore, the solution for $k_{dc}$ in terms of $k$ and $m$ can be obtained by:

$$k_{dc}^3 + 3kk_{dc}^2 + \left(3k^2 + \left(\frac{m+2}{m}\right)^2\right)k_{dc} + \left(k^3 - \frac{(m+2)^2}{2m}k\right) = 0 \tag{A-21}$$

## A-3 Time-domain signal $u_d(t)$ and $u_q(t)$

The signal $u_d(t)$ and $u_q(t)$ can be obtained using the Park transformation:

$$\begin{aligned}\begin{bmatrix} u_d(t) \\ u_q(t) \end{bmatrix} &= \begin{bmatrix} \cos\left(\hat{\theta}(t)\right) & \sin\left(\hat{\theta}(t)\right) \\ -\sin\left(\hat{\theta}(t)\right) & \cos\left(\hat{\theta}(t)\right) \end{bmatrix} \begin{bmatrix} u_\alpha(t) = A\sin\left(\omega(t)t + \varphi\right) \\ u_\beta(t) = -A\cos\left(\omega(t)t + \varphi\right) \end{bmatrix} \\ &= \begin{bmatrix} A\cos\left(\hat{\theta}(t)\right)\sin\left(\omega(t)t + \varphi\right) - A\sin\left(\hat{\theta}(t)\right)\cos\left(\omega(t)t + \varphi\right) \\ -A\sin\left(\hat{\theta}(t)\right)\sin\left(\omega(t)t + \varphi\right) - A\cos\left(\hat{\theta}(t)\right)\cos\left(\omega(t)t + \varphi\right) \end{bmatrix}\end{aligned} \tag{A-22}$$

Now, using the following product-to-sum trigonometric identities:

$$\begin{aligned}\sin(A+B) &= \sin(A)\cos(B) + \cos(A)\sin(B) \\ \cos(A+B) &= \cos(A)\cos(B) - \sin(A)\sin(B) \\ \tan(A+B) &= \frac{\tan(A) + \tan(B)}{1 - \tan(A)\tan(B)}\end{aligned} \tag{A-23}$$

Equation (A-22) can be rewritten to

$$u_d(t) = A\sin\left(\omega(t)t + \varphi - \hat{\theta}(t)\right) \tag{A-24a}$$

$$u_q(t) = -A\cos\left(\omega(t)t + \varphi - \hat{\theta}(t)\right) \tag{A-24b}$$

# Bibliography


[1] UNFCCC, "The Paris Agreement," 2015.

[2] International Energy Agency, "World Energy Outlook 2019," tech. rep., International Energy Agency, Paris, 2019.

[3] J. Meyers, C. Bottasso, K. Dykes, P. Fleming, P. Gebraad, G. Giebel, T. Göçmen, and J.-W. Van Wingerden, "Wind farm flow control: prospects and challenges," *Wind Energy Sience*, vol. 7, pp. 2271–2306, 2022.

[4] A. C. Kheirabadi and R. Nagamune, "A quantitative review of wind farm control with the objective of wind farm power maximization," *Journal of Wind Engineering and Industrial Aerodynamics*, vol. 192, pp. 45–73, 9 2019.

[5] M. N. Soltani, T. Knudsen, M. Svenstrup, R. Wisniewski, P. Brath, R. Ortega, and K. Johnson, "Estimation of rotor effective wind speed: A comparison," *IEEE Transactions on Control Systems Technology*, vol. 21, no. 4, pp. 1155–1167, 2013.

[6] S. Boersma, B. M. Doekemeijer, P. M. Gebraad, P. A. Fleming, J. Annoni, A. K. Scholbrock, J. A. Frederik, and J. W. Van Wingerden, "A tutorial on control-oriented modeling and control of wind farms," *Proceedings of the American Control Conference*, pp. 1–18, 6 2017.

[7] C. Carrillo, A. F. Obando Montaño, J. Cidrás, and E. Díaz-Dorado, "Review of power curve modelling for wind turbines," *Renewable and Sustainable Energy Reviews*, vol. 21, pp. 572–581, 5 2013.

[8] D. R. Houck, "Review of wake management techniques for wind turbines," *Wind Energy*, vol. 25, pp. 195–220, 2 2022.

[9] P. M. Gebraad, F. W. Teeuwisse, J. W. Van Wingerden, P. A. Fleming, S. D. Ruben, J. R. Marden, and L. Y. Pao, "Wind plant power optimization through yaw control using a parametric model for wake effects - A CFD simulation study," *Wind Energy*, vol. 19, pp. 95–114, 1 2016.

[10] F. Porté-Agel, M. Bastankhah, and S. Shamsoddin, "Wind-Turbine and Wind-Farm Flows: A Review," *Boundary-Layer Meteorology 2019 174:1*, vol. 174, pp. 1–59, 9 2019.

[11] T. Uchida, "Effects of Inflow Shear on Wake Characteristics of Wind-Turbines over Flat Terrain," *Energies 2020, Vol. 13, Page 3745*, vol. 13, p. 3745, 7 2020.

[12] M. Bastankhah and F. Porté-Agel, "Experimental and theoretical study of wind turbine wakes in yawed conditions," *Journal of Fluid Mechanics*, vol. 806, pp. 506–541, 11 2016.

[13] X. Ning and D. Wan, "LES Study of Wake Meandering in Different Atmospheric Stabilities and Its Effects on Wind Turbine Aerodynamics," *Sustainability*, vol. 11, p. 6939, 12 2019.

[14] K. Kimura, M. Iida, Y. Tanabe, and Y. Matsuo, "Forced wake meandering for rapid recovery of velocity deficits in a wind turbine wake," *AIAA Scitech 2019 Forum*, 2019.

[15] J. Jonkman and K. Shaler, "Fast. farm user's guide and theory manual," 2021.

[16] X. Yang and F. Sotiropoulos, "A Review on the Meandering of Wind Turbine Wakes," *Energies 2019, Vol. 12, Page 4725*, vol. 12, p. 4725, 12 2019.

[17] V. Gupta and M. Wan, "Low-order modelling of wake meandering behind turbines," *Journal of Fluid Mechanics*, vol. 877, pp. 534–560, 2019.

[18] D. Foti, X. Yang, M. Guala, and F. Sotiropoulos, "Wake meandering statistics of a model wind turbine: Insights gained by large eddy simulations," *Physical Review Fluids*, vol. 1, no. 4, p. 44407, 2016.

[19] E. Torres Garcia, S. Aubrun, M. Boquet, P. Royer, O. Coupiac, and N. Girard, "Wake meandering and its relationship with the incoming wind characteristics: a statistical approach applied to long-term on-field observations," *Journal of Physics: Conference Series*, vol. 854, p. 012045, 5 2017.

[20] D. Foti, X. Yang, and F. Sotiropoulos, "Similarity of wake meandering for different wind turbine designs for different scales," *Journal of Fluid Mechanics*, vol. 842, pp. 5–25, 5 2018.

[21] K. B. Howard, A. Singh, F. Sotiropoulos, and M. Guala, "On the statistics of wind turbine wake meandering: An experimental investigation," *Physics of Fluids*, vol. 27, p. 75103, 7 2015.

[22] D. Medici and P.-H. Alfredsson, "Measurements behind Model Wind Turbines: Further Evidence of Wake Meandering," *Wind Energy*, vol. 11, pp. 211 – 217, 10 2008.

[23] V. Okulov, I. Naumov, R. Mikkelsen, I. Kabardin, and J. Sørensen, "A regular Strouhal number for large-scale instability in the far wake of a rotor," *Journal of Fluid Mechanics*, vol. 747, pp. 369–380, 2014.

[24] L. P. Chamorro, C. Hill, S. Morton, C. Ellis, R. E. A. Arndt, and F. Sotiropoulos, "On the interaction between a turbulent open channel flow and an axial-flow turbine," *Journal of Fluid Mechanics*, vol. 716, pp. 658–670, 2013.

[25] J. Annoni, P. M. Gebraad, A. K. Scholbrock, P. A. Fleming, and J. W. V. Wingerden, "Analysis of axial-induction-based wind plant control using an engineering and a high-order wind plant model," *Wind Energy*, vol. 19, pp. 1135–1150, 6 2016.

[26] E. Bossanyi and R. Ruisi, "Axial induction controller field test at Sedini wind farm," *Wind Energy Science*, vol. 6, pp. 389–408, 3 2021.

[27] P. A. Fleming, P. M. Gebraad, S. Lee, J. W. van Wingerden, K. Johnson, M. Churchfield, J. Michalakes, P. Spalart, and P. Moriarty, "Evaluating techniques for redirecting turbine wakes using SOWFA," *Renewable Energy*, vol. 70, pp. 211–218, 2014.

[28] M. T. van Dijk, J. W. van Wingerden, T. Ashuri, and Y. Li, "Wind farm multi-objective wake redirection for optimizing power production and loads," *Energy*, vol. 121, pp. 561–569, 2 2017.

[29] P. Fleming, J. Annoni, J. J. Shah, L. Wang, S. Ananthan, Z. Zhang, K. Hutchings, P. Wang, W. Chen, and L. Chen, "Field test of wake steering at an offshore wind farm," *Wind Energy Science*, vol. 2, no. 1, pp. 229–239, 2017.

[30] J. P. Goit and J. Meyers, "Optimal control of energy extraction in wind-farm boundary layers," *Journal of Fluid Mechanics*, vol. 768, pp. 5–50, 2015.

[31] W. Munters and J. Meyers, "Towards practical dynamic induction control of wind farms: Analysis of optimally controlled wind-farm boundary layers and sinusoidal induction control of first-row turbines," *Wind Energy Science*, vol. 3, pp. 409–425, 1 2018.

[32] J. A. Frederik, R. Weber, S. Cacciola, F. Campagnolo, A. Croce, C. Bottasso, and J. W. Van Wingerden, "Periodic dynamic induction control of wind farms: Proving the potential in simulations and wind tunnel experiments," *Wind Energy Science*, vol. 5, pp. 245–257, 2 2020.

[33] K. Brown, D. Houck, D. Maniaci, and C. Westergaard, "Rapidly recovering wind turbine wakes with dynamic pitch and rotor speed control," *AIAA Scitech 2021 Forum*, pp. 1–16, 2021.

[34] J. A. Frederik, B. M. Doekemeijer, S. P. Mulders, and J. W. van Wingerden, "The helix approach: Using dynamic individual pitch control to enhance wake mixing in wind farms," *Wind Energy*, vol. 23, pp. 1739–1751, 8 2020.

[35] H. Korb, H. Asmuth, and S. Ivanell, "The characteristics of helically deflected wind turbine wakes," *Journal of Fluid Mechanics*, vol. 965, 6 2023.

[36] J. A. Frederik and J. W. van Wingerden, "On the load impact of dynamic wind farm wake mixing strategies," *Renewable Energy*, vol. 194, pp. 582–595, 7 2022.

[37] A. A. W. Van Vondelen, J. Ottenheym, A. K. Pamososuryo, S. T. Navalkar, J.-W. Van Wingerden, and a. Vanvondelen, "Phase Synchronization for Helix Enhanced Wake Mixing in Downstream Wind Turbines," *IFAC-PapersOnLine*, vol. 56, no. 2, pp. 8426–8431, 2023.

[38] J. Ottenheym, *Control for Helix Enhanced Dynamic Wake Mixing Strategies: The Helix Wake Synchronization Method*. PhD thesis, 2023.

[39] A. A. Van Vondelen, S. T. Navalkar, D. R. Kerssemakers, and J. W. Van Wingerden, "Enhanced wake mixing in wind farms using the Helix approach: A loads sensitivity study," *Proceedings of the American Control Conference*, vol. 2023-May, pp. 831–836, 2023.

[40] L. C. Cheung, K. A. Brown, D. R. Houck, and N. B. deVelder, "Fluid-Dynamic Mechanisms Underlying Wind Turbine Wake Control with Strouhal-Timed Actuation," *Energies*, vol. 17, 2 2024.

[41] M. Beza and M. Bongiorno, "Application of recursive least squares algorithm with variable forgetting factor for frequency component estimation in a generic input signal," *IEEE Transactions on Industry Applications*, vol. 50, no. 2, pp. 1168–1176, 2014.

[42] S. Greś, M. Döhler, P. Andersen, and L. Mevel, "Kalman filter-based subspace identification for operational modal analysis under unmeasured periodic excitation," *Mechanical Systems and Signal Processing*, vol. 146, p. 106996, 1 2021.

[43] L. Dong, W. H. Lio, and F. Meng, "Wake position tracking using dynamic wake meandering model and rotor loads," *Journal of Renewable and Sustainable Energy*, vol. 13, p. 023301, 3 2021.

[44] H. Hajimolahoseini, M. R. Taban, and H. Soltanian-Zadeh, "Extended Kalman Filter frequency tracker for nonstationary harmonic signals," 2011.

[45] A. T. Phan, G. Hermann, and P. Wira, "A new state-space for unbalanced three-phase systems: Application to fundamental frequency tracking with Kalman filtering," *2016 18th Mediterranean Electrotechnical Conference (MELECON)*, pp. 1–6, 2016.

[46] J. Xu, H. Qian, Y. Hu, S. Bian, and S. Xie, "Overview of SOGI-Based Single-Phase Phase-Locked Loops for Grid Synchronization under Complex Grid Conditions," *IEEE Access*, vol. 9, pp. 39275–39291, 2021.

[47] S. Golestan, J. M. Guerrero, F. Musavi, and J. C. Vasquez, "Single-phase frequency-locked loops: A comprehensive review," *IEEE Transactions on Power Electronics*, vol. 34, pp. 11791–11812, 12 2019.

[48] C. J. O'Rourke, M. M. Qasim, M. R. Overlin, and J. L. Kirtley, "A Geometric Interpretation of Reference Frames and Transformations: Dq0, Clarke, and Park," *IEEE Transactions on Energy Conversion*, vol. 34, pp. 2070–2083, 12 2019.

[49] S. P. Mulders, A. K. Pamososuryo, G. E. Disario, and J. W. v. Wingerden, "Analysis and optimal individual pitch control decoupling by inclusion of an azimuth offset in the multiblade coordinate transformation," *Wind Energy*, vol. 22, pp. 341–359, 3 2019.

[50] J. Xu, H. Qian, Q. Qian, and S. Xie, "Modeling, Stability, and Design of the Single-Phase SOGI-Based Phase-Locked Loop Considering the Frequency Feedback Loop Effect," *IEEE Transactions on Power Electronics*, vol. 38, pp. 987–1002, 1 2023.

[51] M. Karimi-Ghartemani, S. A. Khajehoddin, P. K. Jain, A. Bakhshai, and M. Mojiri, "Addressing DC component in pll and notch filter algorithms," *IEEE Transactions on Power Electronics*, vol. 27, no. 1, pp. 78–86, 2012.

[52] C. Zhang, X. Zhao, X. Wang, X. Chai, Z. Zhang, and X. Guo, "A Grid Synchronization PLL Method Based on Mixed Second- and Third-Order Generalized Integrator for DC Offset Elimination and Frequency Adaptability," *IEEE Journal of Emerging and Selected Topics in Power Electronics*, vol. 6, pp. 1517–1526, 9 2018.

[53] Z. Dai, G. Li, M. Fan, J. Huang, Y. Yang, and W. Hang, "Global Stability Analysis for Synchronous Reference Frame Phase-Locked Loops," *IEEE Transactions on Industrial Electronics*, vol. 69, pp. 10182–10191, 10 2022.

[54] G. Li, Z. Dai, B. Wu, Y. Yang, J. Huang, and C. S. Lam, "A Half-Tangent Phase-Locked Loop for Variable-Frequency Grids of the More Electric Aircraft," *IEEE Transactions on Industrial Electronics*, vol. 70, pp. 1576–1585, 2 2023.

[55] C. Zhang, X. Wang, F. Blaabjerg, and W. Wang, "Benchmarking of small-signal dynamics of single-phase PLLs," *9th International Conference on Power Electronics - ECCE Asia: "Green World with Power Electronics", ICPE 2015-ECCE Asia*, pp. 1420–1427, 7 2015.

[56] S. Golestan, M. Monfared, F. D. Freijedo, and J. M. Guerrero, "Advantages and challenges of a type-3 PLL," *IEEE Transactions on Power Electronics*, vol. 28, no. 11, pp. 4985–4997, 2013.

[57] S. Golestan, J. M. Guerrero, J. C. Vasquez, A. M. Abusorrah, V. Khadkikar, and J. Rodriguez, "Control Design of Grid Synchronization Systems for Grid-Tied Power Converters Using Symmetrical Optimum Method: A Comprehensive Reference," *IEEE Transactions on Power Electronics*, vol. 38, pp. 13650–13673, 11 2023.

[58] M. Xie, H. Wen, C. Zhu, and Y. Yang, "DC Offset Rejection Improvement in Single-Phase SOGI-PLL Algorithms: Methods Review and Experimental Evaluation," *IEEE Access*, vol. 5, pp. 12810–12819, 6 2017.

[59] D. R. H. Kerssemakers, *On the Load Impact of the Helix Approach on Offshore Wind Tur-bines Quantifying and analyzing the fatigue load impact of the helix approach on offshore wind turbine components*. PhD thesis, 2022.

[60] B. Jonkman, R. M. Mudafort, A. Platt, E. Branlard, M. Sprague, J. Jonkman, H. Ross, M. Hall, G. Vijayakumar, M. Buhl, P. Bortolotti, S. Ananthan, and J. Rood, "OpenFAST/openfast: OpenFAST v3.5.0.," 1 2024.

[61] E. Gaertner, J. Rinker, L. Sethuraman, F. Zahle, B. Anderson, G. Barter, N. Abbas, F. Meng, P. Bortolotti, W. Skrzypinski, G. Scott, R. Feil, H. Bredmose, K. Dykes, M. Shields, C. Allen, and A. Viselli, "Definition of the IEA Wind 15-Megawatt Offshore Reference Wind Turbine Technical Report," tech. rep., National Renewable Energy Lab.(NREL), Golden, CO (United States), 2020.

[62] N. J. Abbas, D. S. Zalkind, L. Pao, and A. Wright, "A reference open-source controller for fixed and floating offshore wind turbines," *Wind Energy Science*, vol. 7, pp. 53–73, 1 2022.

[63] A. A. W. Van Vondelen, A. K. Pamososuryo, S. T. Navalkar, and J. W. Van Wingerden, "Control of Periodically-Waked Wind Turbines," tech. rep., 2024.

# Glossary

## List of Acronyms

| | |
|---|---|
| ***1*$\phi$** | Single-Phase |
| **3DOF** | Three-Degrees-of-Freedom |
| ***abc*-frame** | three-axis reference frame |
| **AIC** | Axial Induction Control |
| **$\alpha\beta$0-frame** | stationary orthogonal two-axis reference frame |
| **BEM** | Blade-Element Momentum |
| **BL** | Baseline |
| **BOoP** | Blade root Out-of-Plane |
| **BPF** | Bandpass Filter |
| **CCW** | Counterclockwise |
| **CFD** | Computational Fluid Dynamics |
| **CW** | Clockwise |
| **dc** | Direct Current |
| **DIC** | Dynamic Induction Control |
| ***dq*0-frame** | rotating orthogonal two-axis reference frame |
| **DWM** | Dynamic Wake Meander |
| **EKF** | Extended Kalman Filter |
| **ESOGI** | Extended Second-Order Generalized Integrator |
| **FVT** | Final Value Theorem |
| **HAWT** | Horizontal Axis Wind Turbines |
| **HTan** | Half-Tangent |
| **IEA** | International Energy Agency |
| **RWT** | Reference Wind Turbine |
| **IPC** | Individual Pitch Control |

| | |
|---|---|
| **KF** | Kalman Filter |
| **LES** | Large-Eddy Simulation |
| **LF** | Loop Filter |
| **LPF** | Lowpass Filter |
| **LTI** | Linear Time-Invariant |
| **MBC** | Multi-Blade Coordinate |
| **MIMO** | Multiple-Input Multiple-Output |
| **MSc** | Master of Science |
| **MSD** | Mass-Spring-Damper |
| **MSTOGI** | Mixed Second- and Third-Order Generalized Integrator |
| **NF** | Notch Filter |
| **NREL** | National Renewable Energy Laboratory |
| **nsKF** | non-steady state Kalman Filter |
| **O&M** | Operation and Maintenance |
| **PD** | Phase Detection |
| **PI** | Proportional-Integral |
| **PLL** | Phase-Locked Loop |
| **QT2PLL** | Quasi Type-2 Phase-Locked Loop |
| **RLS** | Recursive Least Squares |
| **ROSCO** | Reference Open-Source COntroller |
| **SISO** | Single-Input Single-Output |
| **SNR** | Signal-to-Noise Ratio |
| **SOGI** | Second-Order Generalized Integrator |
| **SOWFA** | Simulator fOr Wind Farm Applications |
| **SRF** | Synchronous Reference Frame |
| **STD** | Standard Deviation |
| **T2** | Downstream Turbine |
| **TC** | Test Case |
| **TOGI** | Third-Order Generalized Integrator |
| **TSR** | tip-speed-ratio |
| **VCO** | Voltage-Controlled Oscillator |